AN EXPERIMENTAL INVESTIGATION OF PROPAGATION OF WEAK SHOCK WAVES IN A RANDOM MEDIUM

Thesis by

Lambertus Hesselink

In Partial Fulfillment of the Requirements
For the Degree of
Doctor of Philosophy

California Institute of Technology
Pasadena, California
1977
(Submitted May 24, 1977)

ACKNOWLEDGEMENTS

The advice and wise counsel given by many people during the course of this experiment are gratefully acknowledged.

The author's advisor , Professor Hans Liepmann, and Professor Bradford Sturtevant, provided inspiration, guidance and encouragement. I am indebted to them for their help with this research project, their invaluable contributions to my education and their friendship.

Professor Donald Coles' stimulating advice, in particular regarding experimental techniques, his interest in the project and his friendship are greatly appreciated.

The author wishes to thank Professor Nicholas George and Dr. Vijay Kulkarny; interesting discussions with them contributed to my understanding of the phenomenon under investigation.

Special thanks go to the technical staff of GALCIT for their assistance with the experimental apparatus. It is also a great pleasure to thank Mrs. Jacquelyn Beard and Mrs. Karen Cheetham for their excellent typing, Mrs. Betty Wood for her splendid drawings, and Professor Bradford Sturtevant for his constructive criticism during the preparation of the manuscript.

The financial assistance of the California Institute of Technology, the Josephone de Karman trust fund, and the Air Force Office of Scientific Research, which also sponsored the project is gratefully acknowledged.

Last, but not least, I thank my wife, Marieka, who contributed tremendously to this effort by her constant support.

ABSTRACT

An apparatus has been constructed for generating a 25 cm cube of randomly inhomogeneous gas in the GALCIT 17-inch diameter shock tube. It consists of a two-dimensional 7 x 8 array of fine jets alternately of helium and freon-12 behind coarse grids located on opposite sides of a box. The two other side walls of the box are fitted with optical windows for diagnostics. The upstream and downstream faces of the box are movable and can be opened rapidly just before shock arrival. This process is automated, and the arrival time of the shock wave relative to the decay of the turbulent density field can be varied. The gas mixture is made neutrally buoyant so that the mean interface between the scattering region and the uniform air in the shock tube is parallel to the plane of the incoming wave. Furthermore, the mean acoustic impedance of the mixture is matched to that of the quiescent air in the shock tube to minimize the effect of the air-gas mixture interface on the shock wave.

In this experiment shock waves of strengths varying from $M_s = 1.007$ to 1.1 scatter from random variations of acoustical impedance and index of refraction (defined as the ratio of the sound speed in air to the local, variable, sound speed in the scattering medium) which occur during the turbulent mixing of the two different gases. The scale and amplitude of the fluctuations before interaction with the shock wave are obtained from optical and point density measurements; the method of Uberoi and Kovasznay (Ref. 10) has been used to obtain length scales of the flow from shadowgraph and schlieren pictures, and the Brown-Rebollo (Ref. 11) density probe is used to measure local mean and rms density fluctuations, and space- and cross-correlation functions.

To study the interaction of the shock with the turbulence, spark shadowgraph and schlieren pictures have been taken and pressure measurements have been made. Arrays of pressure transducers located in a false endwall downstream of the scattering volume record the shock front topology and the spatial variation of shock amplitude.

The pressure measurements indicate a substantial modification of the unperturbed shock profile. Data are presented which indicate the effect of the Mach number on the scattering process.

Optical measurements show that length scales in the fluid, which is processed by all but the weakest shocks, have changed due to the interaction process.

TABLE OF CONTENTS

Chapter	Title	Page
	Acknowledgements	ii
	Abstract	iii
	Table of Contents	v
	List of Figures	x
	List of Tables	xiv
I	INTRODUCTION	1
	1.1 Motivation for the Research	1
	1.2 Research Goals	6
II	DESIGN OF THE EXPERIMENT	8
	2.1 Objectives	8
	2.2 Turbulent Mixer	9
	2.2.1 General Description	9
	2.2.2 Refractive Index Fluctuations	9
	2.2.3 Flow Control System	11
	2.2.4 The Grids	12
	2.2.5 The Shutters	13
	2.2.6 The Optical Windows	14
	2.2.7 The Cookie-Cutter	15
	2.2.8 Shock Tube Firing Mechanism	15
	2.3 Electronic Control System for the Turbulent Mixer	16
	2.3.1 Objectives	16
	2.3.2 Description of the Electronic Circuitry	17
	2.3.3 Performance	20

TABLE OF CONTENTS (Continued)

Chapter Title Page

2.4 Experimental Procedure 20

2.5 Performance of the Experimental Facility 21

III INSTRUMENTATION 23

3.1 Scope 23

3.2 Aspirating Density Probe 24

3.3 Optical Measurements 24

3.3.1 Optical Processor 24

3.3.2 Schlieren System 27

3.3.3 Shadowgraph System 28

3.3.4 Optical Correlator 28

3.3.5 Optical Fourier Transform Photography 29

3.4 Pressure Measurements 29

3.4.1 Pressure Transducer Mounts 29

3.5 Data Acquisition System 31

IV DATA ACQUISITION AND PROCESSING 32

4.1 Scope 32

4.2 Point Density Measurements 32

4.2.1 Data Acquisition Procedure 32

4.2.2 Computer Calculation of the Mean and rms Concentration Profiles 35

4.2.3 Computer Calculation of Cross- and Space-Correlation Functions 36

4.3 Optical Measurements 37

4.3.1 Measurement of the Shadowgraph and Schlieren Picture Correlation Function 37

TABLE OF CONTENTS (Continued)

Chapter	Title	Page
	4.3.2 Calculation of the Microscale for the Density Field Using the Shadowgraph Picture Correlation Function	38
	4.3.3 Calculation of a Length Scale for the Density Field Using Optical Fourier Transform Photography	40
	4.4 Pressure Measurements	42
	4.4.1 Data Acquisition Procedure	42
	4.4.2 Data Reduction Scheme for Pressure Signals in the Scattered Wave Field	43
V	CHARACTERIZATION OF THE SCATTERING MEDIUM	46
	5.1 Scope	46
	5.2 Experimental Procedure for Tuning the Flow Control System	46
	5.3 Results	47
	5.3.1 Mean and rms Density Profiles	47
	5.3.2 Shutter Opening Effects	51
	5.3.3 Cross- and Space-Correlation Functions	52
	5.3.4 Length Scales Obtained from the Optical Measurements	53
	5.4 Summary of the Results Characterizing the Selected Scattering Medium	56
VI	EFFECTS OF THE SCATTERING MEDIUM ON THE SHOCK WAVE	57
	6.1 Scope	57
	6.2 Representative Pressure Data Profiles	57

TABLE OF CONTENTS (Continued)

Chapter	Title	Page
	6.3 Characteristics of the Scattered Wave Field	60
	6.3.1 Shock Amplitude Results	60
	6.3.2 Peak Amplitude Results	63
	6.3.3 Shock Wave Front Topology Results	64
	6.3.4 Wave Front Thickness Results	65
	6.3.5 Peak Width Results	70
	6.3.6 Schlieren and Shadowgraph Pictures	71
	6.4 Comparison of the Shock Front Topology Results with Geometrical Acoustics Theory	73
VII	EFFECTS OF THE SHOCK WAVE ON THE SCATTERING MEDIUM	76
	7.1 Scope	76
	7.2 Scale Changes in the Density Field Induced by the Shock Wave	76
	7.2.1 Data Obtained from Schlieren Pictures	76
	7.2.2 Data Obtained from Shadowgraph Pictures	78
VIII	CONCLUSIONS	81
	APPENDICES	85
	Appendix A Details of Experimental Apparatus	85

TABLE OF CONTENTS (Continued)

Chapter		Title	Page
	A4	Shutter Drive Mechanism	88
	A5	The Shock Tube Firing Mechanism	88
	A6	Electronic Control Circuitry	88
	A7	Normal Operating Conditions	89
	Appendix B	Instrumentation	
	B1	Density Probe	90
	B2	Schlieren System	92
	B3	Optical Correlator	94
	B4	Data Acquisition System	96
Tables			97
Figures			103
References			154

LIST OF FIGURES

Number	Title	Page
1.1	Typical Theoretically Predicted Sonic Boom Pressure Profile	3
1.2	Typical Recorded Sonic Boom Pressure Profiles	4
3.1	Schematic of an Optical Processor	25
3.2	Pressure Transducer Mounting Plug	103
3.3	False Endwall for Pressure Transducers	104
4.1	Optical Setup for Fourier Transform Photography	41
4.2	Schematic Pressure Profile	43
4.3	Wave Front Showing Precursor	44
4.4	Schematic Pressure Profile Showing a Peaked Wave Front	45
5.1	Density Probe Locations	105
5.2	Mean and Rms Density Profile	106
5.3	Mean Concentration as a Function of the Height above the Bottom	107
5.4	Mean and Rms Density Profile Showing Shutter Effect	108
5.5	Raw Density Data (Jets On)	109
5.6	Raw Density Data (Jets Off)	110
5.7	Space-Correlation Function	111
5.8	Cross-Correlation Function (M = 3.2 cm)	112
5.9	Example of Shadowgraph Correlation Function	113
6.1	The Effect of the Decay Time of the Density Fluctuations on the Shock Wave	114
6.2	Representative Pressure Traces Measured in False Endwall (Horiz. 20 μsec/cm)	115
6.3	Histograms of Normalized Shock Pressures as a Function of Mach Number (Measured near Downstream Shutter)	116

LIST OF FIGURES (Continued)

Number	Title	Page
6.4	Histograms of Normalized Shock Pressures as a Function of Mach Number (Measured near Endwall)	117
6.5	Extreme Values of Normalized Pressures as a Function of Mach Number (Measured near Downstream Shutter)	118
6.6	Extreme Values of Normalized Pressures as a Function of Mach Number (Measured near Endwall)	119
6.7	Histograms of Normalized Peak Pressures as a Function of Mach Number (Measured near Downstream Shutter)	120
6.8	Histograms of Normalized Peak Pressures as a Function of Mach Number (Measured near Endwall)	121
6.9	Histograms for the Time Lag of the Peak Pressure behind the Front (Measured near Downstream Shutter)	122
6.10	Mean Values for the Time Lag between Peak and Shock Front Pressures (Measured near Downstream Shutter)	123
6.11	Rms Arrival Time Fluctuations as a Function of Mach Number	124
6.12	Histogram of Shock Rise Times ($M_s = 1.007$)	125
6.13	Geometrical Effects on Shock Wave Topology	66
6.14	Schlieren Photograph of $M_s = 1.03$ Unperturbed Shock Moving from Right to Left	126
6.15	Shadowgraph Photograph of $M_s = 1.007$ Shock Which is Indistinguishable from the Turbulence	127
6.16	Shadowgraph Photograph of $M_s = 1.03$ Shock Moving from Right to Left	128
6.17	Shadowgraph Photograph of $M_s = 1.1$ Shock Moving from Right to Left	129

LIST OF FIGURES (Continued)

Number	Title	Page
6.18	Schlieren Photograph of $M_s = 1.007$ Shock Which is Indistinguishable from the Turbulence	130
6.19	Schlieren Photograph of $M_s = 1.03$ Shock Moving from Right to Left	131
6.20	Schlieren Photograph of $M_s = 1.1$ Shock Moving from Right to Left	132
A.1	Horizontal Cross Section and Top View of Turbulent Mixer	133
A.2	Schematic End View (Endplate Removed)	134
A.3	Photograph of Turbulent Mixer Units	135
A.4	Photograph of Shutter Assembly (Open)	136
A.5	Photograph of Plenum Chamber and Grid	137
A.6	Photograph of Turbulent Mixer	138
A.7	Schematic of Shutter Assembly (Face Plate of Bottom Shutter Blade Removed)	139
A.8	Schematic Flow Control System for Turbulent Mixer	140
A.9	Groove Pattern in the Vertical Sidewalls of the Mixing Zone	141
A.10	Schematic of Grid Drive Mechanism	142
A.11	Schematic of Shutter Drive Mechanism	143
A.12	Window Locations	144
A.13	Shock Tube Firing Mechanism	145
A.14	Schematic of Electronic Control System for the Turbulent Mixer	146
A.15	Schematic of a Single Channel	147
B.1	Density Probe	148
B.2	Side View Schlieren System	149

LIST OF FIGURES (Continued)

Number	Title	Page
B. 3	Details Schlieren System	150
B. 4	Optical Correlator	151
B. 5	Photograph of Optical Correlator	152
B. 6	Data Acquisition Scheme	153

LIST OF TABLES

1. Length Scales Obtained from Picture Correlation Functions

2. Changes in Turbulence Length Scales Induced by the Shock Wave

3. List of Traces with Precursors

4. Mean Value for the Arrival Time Difference between Pressure Gauges Mounted in False Endwall

5. Peak Widths Behind Amplified Shocks

6. Characterization of the Anisotropy of the Shock Compressed Fluid

I. INTRODUCTION

1.1 Motivation for the Research

With the increasing need during the last 30 years to understand the mechanisms of acoustic-wave propagation in the oceans and atmosphere and/or radio-wave propagation in the atmosphere, the theory of wave propagation in random media has been extensively developed and verified by experiment. Contemporary applications in technology, including propagation of sonic boom and blast waves through the earth's turbulent boundary layer, transonic shock-boundary layer interaction, and laser communications and energy conversion have fueled continuing interest in the field.

The major difficulty, of course, deriving from the impossibility of characterizing the random medium in complete detail, is the question of what properties of the medium must be specified in order to obtain desired information about the wave field. For the case in which fluctuations of index of refraction in the medium and the resulting perturbations of the wave field are small, the theory is rather complete (Chernov, Ref. 1). This is linear or single-scattering theory, in which the scattered waves are of small amplitude or, in the alternative terminology of geometrical acoustics, the deflection of the rays normal to the wave fronts is small.

The question of how nonlinear effects first make themselves felt in different scattering problems is not so clear and has not been considered in any detail. For example, the single-scattering theory of the sonic boom (Crow, Ref. 2) predicts impossibly large perturbations on the shock front, suggesting that in order to predict shock amplitude (of primary importance in determining the environmental impact of the sonic boom), consideration of multiple scattering is necessary. In the terminology of geometrical acoustics, the small-amplitude theory does not provide for focusing of wave fronts, which surely must occur when perturbations of wave-front geometry become sufficiently large. It is not known what scales of turbulence might lead to important focusing effects in any given situation, or indeed, what the effect of focusing might be on the statistics of wave front geometry and perturbation amplitude. In particular, there are no experimental results available which provide any information about the effects of second-order scattering or gas-dynamic nonlinearity on the propagation of weak shock waves through random media.

Keller (Ref. 3) has reviewed the theories available for treating problems in which the random variations are not small. In most analyses averaged equations are formed which yield solutions in terms of the moments of the unknowns. This procedure is precisely analogous to the construction of the mean equations of motion for turbulence, and yields a hierarchy of moment equations which must be broken at some level by a closure approximation. Thus, the analysis of scattering in a fluid with large fluctuations reduces to a problem identical to and of equal difficulty as the description of turbulence. Indeed, it can be argued that the study of scattering in a turbulent fluid is nothing other than the study of turbulence itself, and that the results of such studies may provide some useful insights into the nature of turbulence itself.

Consideration of the sonic-boom problem affords a convenient point of view for illustrating the features of shock propagation in a random medium. Some results from sonic-boom theory and experiment, which are relevant to the current study, will be briefly discussed.

An airplane which flies supersonically in a uniform atmosphere generates a pressure wave which at large distances from the aircraft has an N-shaped profile (Whitham, Ref. 4), consisting of an expansion wave sandwiched between two shock waves. An N-wave with amplitude and time scale typical of that predicted to occur on the earth's surface under a supersonic transport flying at cruise altitude is shown in Figure 1.1.

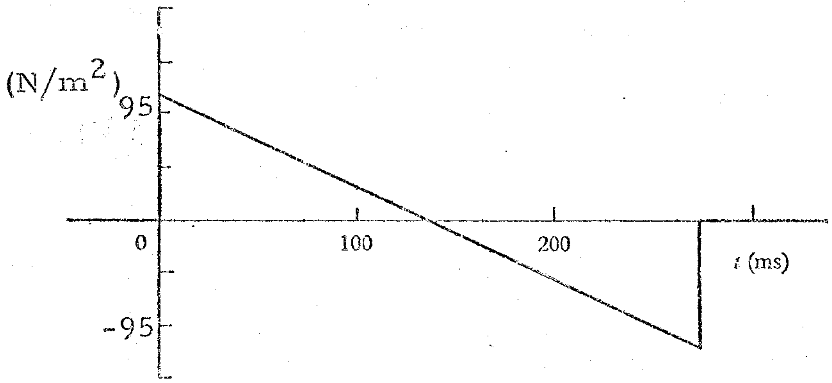

Figure 1.1 Typical Theoretically Predicted Sonic Boom Pressure Profile.

In practice, however, measurements made on the ground during flight tests indicate substantial departures from the predicted wave form, which occur in a random and unpredictable fashion. NASA investigators (Maglieri et al., Ref. 5) have documented the results of some of the tests and have classified the wave forms in three categories (Fig. 1.2): a) peaked, b) rounded, and c) normal.

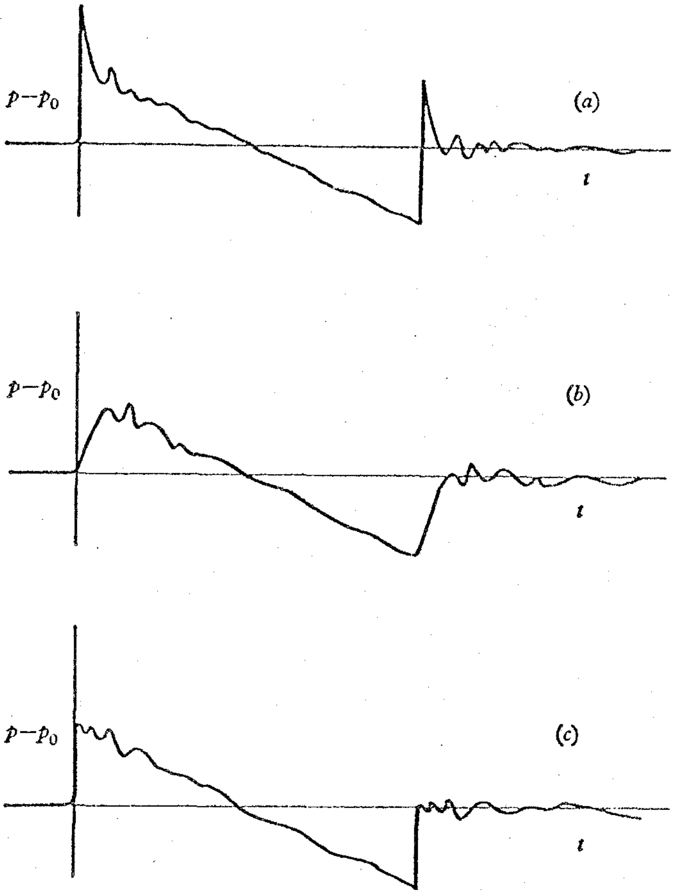

Figure 1.2 Typical Recorded Sonic Boom Pressure Profiles.

For the purpose of studying the modifications of the N-wave, the interaction of a single shock with turbulence can be considered. Crow (Ref. 2) first formulated a single-scattering theory which explained many features of the flight-test observations. However, in some cases documented by Maglieri, the rise time of the initial disturbance on the N-wave is observed to be up to three orders of magnitude greater than the shock thickness predicted by the Navier-Stokes equations.

Several investigators have proposed theories to explain these results. Crow pointed out that second-order scattering theory contains shock thickening, and George and Plotkin (Ref. 6) developed a second-order perturbation scheme which led to a Burgers-type equation for the wave structure, with the molecular viscosity replaced by a viscosity-like term depending on properties of the earth's turbulent boundary layer. Pierce (Ref. 7) suggested that the apparent rise times could be explained by geometrical effects, but his idea has not been developed in any detail. He proposed that the peaked and rounded profiles measured in sonic boom experiments can be explained in terms of fucusing and defocusing of the incident shock front. The increased rise time of the initial disturbance is accounted for by the occurrence of multiple folded wave fronts.

Ffowcs Williams and Howe (Ref. 8) introduced a statistical argument to show that the shock thickness predicted by George and Plotkin is an irrelevant upper bound and is a result of the apparent mean diffusion induced by random convection of a sharp wave front around its nominal position. Furthermore, they conclude that turbulence cannot be responsible for the observed shock thickness, and that a wave-front-folding mechanism is too slow to be effective in the practical sonic boom situation. They propose that the observed change in shock structure is caused by vibrational relaxation effects of oxygen and nitrogen in the earth's boundary layer. The relaxation frequencies of these gases are strongly dependent on the water vapor content in the air (Hodgson, Ref. 9), and, unfortunately, this quantity is not routinely measured during flight tests.

This investigation was designed to provide additional information of the propagation of weak shock waves through a random medium. For this purpose a classical scattering configuration is chosen and waves scatter from random variations of acoustical impedance and index of refraction (defined as the ratio of the sound speed in air to the local, variable sound speed in the scattering medium) which occur during the turbulent mixing of the two different gases. In this experiment, the scattering is principally from density fluctuations, and the contributions from the turbulence to the index of refraction are small. The scale and amplitude of the fluctuations before interaction with the shock waves are obtained from optical and point density measurements; the method of Uberoi and Kovasznay (Ref. 10) has been used to obtain length scales of the flow from shadowgraph and schlieren pictures, and the Brown-Rebollo (Ref. 11) density probe is used to measure local mean and rms density fluctuations and space- and cross-correlation functions.

To study the interaction of the shock with the turbulence, spark shadowgraph and schlieren pictures have been taken and pressure measurements have been made. Arrays of pressure transducers located in a false endwall downstream of the scattering volume record the shock front topography and the spatial variation of shock amplitude.

1.2 Research Goals

The research efforts were concentrated around the following objectives:

1. To measure the scattered wave field and in particular its dependence on the strength of the incident wave and the statistical properties of the scattering medium;
2. To investigate the modifications, if any, of the random medium due to the propagating shockwave; and
3. To determine the influence of nonlinear effects on the interaction process.

The current investigation was not designed to model a specific technical application. The aim of this scientific endeavor has been to provide unambiguous results under carefully controlled laboratory conditions. These results may point the way to a better physical understanding of this difficult interaction phenomenon.

II. DESIGN OF THE EXPERIMENT

2.1 Objectives

To study the propagation of weak shock waves through a random medium, a classical scattering configuration is chosen. The shock waves are generated in the GALCIT* 17-inch diameter shock tube. The random medium is produced in the turbulent mixer which is mounted at the end of the shock tube. Following are the design criteria for this apparatus:

1. To achieve within a 27 cm cube of gas a randomly varying acoustical index of refraction (ratio of the speed of sound in air at standard conditions to the local speed of sound),
2. To maximize the random perturbations of sound speed while still maintaining overall statistical homogeneity and isotropy,
3. To insert the nonuniform medium between regions of quiescent test-section fluid,
4. To match the mean acoustic impedance and the mean density of the interface between the gas in the test section and in the turbulent mixer,
5. To accommodate optical diagnostic tools such as schlieren and shadowgraph photography, and
6. To insure repeatability of mechanical functions within 0.5%.

---

*Graduate Aeronautical Laboratories, California Institute of Technology

2.2 Turbulent Mixer

2.2.1 General Description

The turbulent mixer, mounted at the end of the 17-inch shock tube, generates a rectangular volume of incompletely mixed gas (Figs. A.1 and A.2). The apparatus consists of an array of fine jets alternately of helium and freon-12 behind coarse grids located on opposite sides of a box. The grids are rapidly retracted flush with the side walls before the shock tube is fired. The other two side walls are fitted with optical windows for diagnostics. The vertical upstream and downstream walls of the box are fitted with shutters which can be opened rapidly just before shock arrival. This process is automated, and the arrival time of the shock relative to the decay time of the turbulent density field can be varied. The gas mixture is made neutrally buoyant so that the mean interface between the scattering region and the uniform gas in the shock tube remains parallel to the plane of the incoming wave.

2.2.2 Refractive Index Fluctuations

The speed of propagation of a sound wave in a gas depends on the thermodynamic properties and the macroscopic convection velocity, v, of the medium, i.e.,

$$a\ (x,t) = v\ (x,t) + \left(\gamma \frac{R_o}{M_w} T\right)^{\frac{1}{2}} \qquad (2\text{-}1)$$

where γ is the ratio of the specific heats, R_o the universal gas constant, M_w the molecular weight, and T the absolute temperature.

Therefore, in principle at least, acoustical index of refraction fluctuations may be generated by varying the temperature, velocity, or density of the fluid.

In this experiment, a mixture of gases was used for two reasons:

1. By randomly mixing two gases with a largely different molecular weight and structure, the acoustical index of refraction fluctuation could be maximized; and
2. The turbulent mixing process could be easily observed optically.

To exclude modification or scattering of the shock wave due to large-scale variations of the mean index of refraction, the average sound speed of the binary mixture must match the sound speed of air in the test section of the shock tube. Furthermore, by matching in addition the mean density, the interface between the turbulence region and the quiescent fluid is, on the average, parallel to the plane of the incoming shock wave. Consequently the mean acoustic impedance is matched as well, which minimizes the generation of reflected waves. Details of this calculation are left to a discussion in Appendix A2.

From all possible solutions, a mixture of 80% He by volume and 20% Freon-12 ($C\,C\ell_2\,F_2$: dichlorodifluoro methane) was chosen. The two gases have largely different densities and speeds of sound and are readily available commercially. Furthermore, they are chemically inert and exhibit no vibrational relaxation effects for times larger than 1 μsec, the resolution of the pressure transducers used in this experiment. Theoretical studies seem to indicate that the shock-wave structure of the sonic boom is perhaps partially determined by vibrational relaxation effects of nitrogen and oxygen in the earth's atmosphere, but in the current investigation this effect is excluded.

2.2.3 Flow Control System

A schematic of the flow control system is shown in figure A.7. Standard purity, gaseous helium is stored in four gas cylinders for a total capacity of 23 standard cubic meters. Four Matheson A-9 regulators reduce the cylinder pressure to the required working level. The gas is conveyed from the cylinders to two plenum chambers via two 2.5 m long and 1.25 cm diameter copper pipe systems. From the plenum chamber, the helium is injected into the mixing zone through 28 jets in the sidewall of the shock tube. Just upstream of the plenum chambers, each supply line contains two contoured nozzles in parallel. The flow in the throat is sonic under steady state running conditions. Therefore, the flow rate through the jets is solely controlled by the pressure upstream of the nozzles (assuming constant room temperature).

Freon-12 is stored in a cylinder as a liquid under its own vapor pressure for a total capacity of 18 standard cubic meters of gas. In the gas phase, it is kept in a 117 cm section of the 17-inch shock tube which acts as a storage and supply reservoir. From here the freon-12 passes through a pipe system similar to that for the helium to the two plenum chambers. Each chamber is connected to 28 jets through an equal number of ϕ 4.8 mm pipes which run through the helium reservoirs. The 56 helium and freon-12 jets in each sidewall are arranged in a checkerboard configuration. The gas supply to these jets is impulsively started and stopped by fast acting solenoid valves just upstream of the two contoured nozzles. Inside the mixing zone, grids can be retracted flush with the sidewall and in doing so cover up the jets as explained in Section 2.2.4.

2.2.4 The Grids

The purpose of the grids is twofold:

1. To cover the jets in the retracted position. The front surface of the grid then falls flush with the sidewall, which minimizes diffraction effects on the shock wave.
2. To produce, to a good approximation, homogeneous and isotropic turbulent density fluctuations.

During the design phase of the project, extensive documentation on grid turbulence was consulted (Batchelor, Ref. 5). As a result of this effort, the meshwidth M = 3.2 cm was chosen to maximize the density fluctuations, yet keep the integral scale small compared with the size of the rectangular shock tube test section (26.6 cm x 26.6 cm). The solidity of the grid, that is the ratio of the closed area to the total area, was designed to be 0.75. It was also thought important to avoid head-on collision of the jets on opposite sides of the box. Therefore, the grids were horizontally and vertically offset by $M/2 = 1.6$ cm.

The sidewalls containing the grids in the retracted position were made of Al-2024. A groove pattern was machined in each wall using an endmill specifically designed for this purpose (see Appendix A1). At each intersection a ∅ 3.2 mm hole was drilled, for a total of seven rows and eight columns. The sidewalls were then used as a mold for the grids themselves. First a support core was constructed consisting of Al-2024 bars, with a cross section of 10.2 x 4.8 mm. This structure was positioned 2.5 mm from the bottom of the grooves before the turbulent mixer was assembled. With the mold in the horizontal position, the grooves were then filled with a 50% mixture, by weight, of GE RTV-631 and RTV-632 rubber to a depth of 5 mm. The rubber is bonded to the aluminum core by GE primer SS 4155.

The remaining empty volume of the grooves was filled with Emerson & Cummings stycast FT4150. The aluminum oxide impregnated epoxy was selected to match the Al-2024 coëfficient of thermal expansion. Subsequently, the sidewalls containing the grids in the retracted position were ground to the proper thickness to remove excess stycast. The discussion of the drive mechanism for the grids is presented in Appendix A3.

The gas injected into the mixing zone is exhausted into the atmosphere via removable walls, hereafter referred to as shutters.

2.2.5 The Shutters

The purpose of the shutters is to separate the turbulence region from the quiescent air in the shock tube test section. This is accomplished by a device very much like a camera shutter. Both shutters contain four blades each. Each blade consists of two parallel plates with a cavity sandwiched between. The cavity is connected to the scattering medium through 14 ø 3.2 mm holes. The plate adjacent to the shock tube test gas is solid. The shutter blades exhaust to the atmosphere through a ø 1.25 cm exhaust line. The shock tube test section and the turbulent mixing volume are both at atmospheric pressure after the jets are turned off.

Each blade rotates around a pivot point. After a 45 degree turn from the closed configuration, the diagonal side of each blade coincides with the shock tube sidewall.* The four blades of each shutter are linked together by a 1.25 cm wide and 0.5 mm thick steel band (see Appendix A1). A four-linkage mechanism connects the shutter blades to a high-pressure air-driven linear actuator, (Dynamation DM 35) which drives the assembly. The kinematics of this system insures a 45 degree rotation of the blades with zero angular velocity at the end of the piston stroke (see Appendix A4). This arrangement prevents the four blades from colliding with each other with any appreciable angular momentum. The shutter opening time can be adjusted by varying the upstream pressure in the drive cylinders as well as monitoring the exhaust gas flow rate. The shutters are closed by reversing the flow direction through the actuators.

2.2.6 The Optical Windows

The top and bottom horizontal sidewalls of the mixing region are fitted with optical windows for diagnostics (ø 15.2 cm diameter and 3.2 cm thick BK-7 schlieren quality glass). Care was taken to

---

*This principle was developed according to a suggestion from Prof. Donald Coles.

adjust the two plates parallel in order to avoid ghost images due to multiple reflections between the plates. The windows can be located at four stations in the mixing zone sidewall (as indicated in Appendix A1) as well as upstream and downstream of the shutters.

2.2.7 The Cookie-Cutter

The cookie-cutter was designed to facilitate the transition from a circular cross section to a square one. The upstream edges are wedges with a 12 degree tip angle. The length of the tube, which is 122 cm, determines the test time of the experiment. In the Mach number range $M_s = 1.007$ to $M_s = 1.1$, this configuration assures that the reflected shock wave from the endwall of the 17-inch shock tube and the reflected wave from the endwall of the turbulent mixer meet upstream of the nonuniform gas mixture. The test time is then defined as the period in which the shock wave travels twice the distance from this meeting point to the endwall of the turbulent mixer.

2.2.8 Shock Tube Firing Mechanism

The firing mechanism of the GALCIT 17-inch shock tube had to be modified to permit automatic operation (details of the modifications are discussed in Appendix A5). The manual procedure previously used is well documented (Liepmann, et al. Ref. 13) and briefly summarized here.

The driver section is slowly pressurized. The diaphragm, which is clamped around the perimeter, deflects against a set of crossed straight knife blades. The shock tube fires when the membrane ruptures.

In the current experiments, the driver can be pressurized at an adjustable rate for a preset period of time. The knife blades are made movable as well. Now the firing procedure has been altered to the following:

Before a run is started, the driver pressure is preset to 0.014 atm below the bursting pressure. Then at a predetermined time in the experimental procedure (see Section 2.4) the driver pressure is monotonically increased at a rate of approximately 0.06 atm/sec until the diaphragm fractures. Furthermore, the firing time of the weakest shocks, $M_s = 1.007$, can be controlled by injecting the knife blades into the membrane (0.0127 mm thick mylar). The timing of the knife blade motion as well as the position with respect to the undeflected membrane was found to be very crucial. When the driver pressure is too low the shocks do not reach their equilibrium state before the end of the test section. On the other hand, if the knife blades are injected into the diaphragm when the driver pressure is less than 0.001 atm below the bursting pressure, the arrival time of the shocks at the mixing zone becomes erratic. The knife blades were therefore displaced when the driver pressure was approximately 0.002 atm below the bursting pressure. Furthermore, the knife blades should be located as close as is convenient to the diaphragm, yet be far enough away to insure a sufficiently high firing pressure.

2.3 Electronic Control System for the Turbulent Mixer

2.3.1 Objectives

Following are the required operating characteristics of the electronic control system (ECS):

1. To control the mechanical functions of the turbulent mixer, either in preprogrammed order or independently of each other;
2. To fire the GALCIT 17-inch shock tube automatically;
3. To supply the BETA signal (see Section 4.2.1) to the Analog-to-Digital Convertor for computer controlled data acquisition;
4. To generate a general purpose TTL compatible trigger signal;
5. To generate a timing signal for the spark gap control circuitry;
6. To prevent actions which may destroy elements of the turbulent mixer. In particular, the shock tube should neither be fired with the shutters closed nor gas injected into the mixing zone with the grids retracted;
7. To provide an option to bypass the safety checks; and
8. To optimize noise immunity under TTL operating conditions and to measure repeatability of the output signals within 0.5%.

2.3.2 Description of the Electronic Circuitry

The electronic control center, as indicated in Appendix A6, consists of nine channels which control the following functions:

1. the sparkgap,
2. the BETA signal,
3. a general purpose trigger signal,
4. the motion of grid 1,

5. the motion of grid 2,
6. the gas flow through the helium and freon-12 supply lines,
7. the motion of the shutters,
8. the flow into the driver section of the 17-inch shock tube, and
9. the motion of the knife blades.

Most channels consist of three basic elements: a delay, a timer, and an open collector inverter (see Appendix A 6). The delay and timer are SN 74121 monostable vibrators. An input trigger signal can be either delayed or transmitted directly to the timer. The timer output as well as the delay are adjustable in length. The timer signal then passes through an open collector inverter before it is conveyed to the output device. Two or more inverters connected in parallel are used as a logic comparator. All inputs have to be in the same (logical 0) state before a signal is transmitted to the common output line. This feature is used to check the status of elements in the turbulent mixer before executing the function of that particular channel.

The principle of operation can best be explained by considering Figure A. 14. The main switch, when flipped from the reset to start position, causes the grids to move away from the sidewalls. This is accomplished by a high-to-low transition (logical 1 to 0) from the solid state bounceless switch which is connected to the main toggle switch. This trigger then changes the status of the D-type flip-flop, and the inverter signal is amplified by the current amplifier whose output energizes the normally closed solenoid valves in the supply lines to the grid drive mechanism (see Appendix A3). At the end of the translation, two limit-switches signal the position of the grids to the control unit. Then, in the check mode with the safety checks operational, the trigger signal is conveyed to all channels except 8 and 9.

Thereafter, each channel executes its operation according to the status of the toggle switches and the values of the variable resistors which determine the duration of the delay and timer signals (see Appendix A6). The on-off switches in all output lines conveniently offer the option whether or not to transmit the command signals to the output devices. After the grids retract and the shutters open, the limit switches indicate their positions to the control center. A trigger pulse is then transmitted to channel 8 to pressurize the driver and move the knife blades, if desired. In the check mode, the shutters must be first closed and then opened before the shock tube will fire. In the bypass mode, no checks are performed on the status of the shutters or grids. Then the main-switch trigger signal is immediately transmitted to channel 8 after the grids have moved away from the sidewall. Under no circumstances, however, can gas be injected into the mixing zone when the grids cover the jets. The input to the open collector inverter is then high, thus preventing the timer signal from being transmitted. The knife blades cannot be moved unless the driver is being pressurized.

Solid state relays (Teledyne Relay 601-1401) were used whenever a 115 v AC had to be switched. This avoids electromagnetic noise and spikes in the common 115 v power lines usually associated with mechanical relays. Noise immunity from external sources is further enhanced by connecting all switching lines in the TTL logic circuits to + 5 v, using a differentiating circuit. The high or logical 1 output level is thereby raised from 3.3 v to 5 v increasing the noise immunity from 2.5 v to 4.2 v for a negative pulse going from high to low (logical 1 to logical 0).

2.3.3 Performance

All delays and timers were accurate and repeatable to at least 2 msec per 2000 msec or 0.1%. Thermal stability was better than 0.1% after the unit was turned on for half an hour. The noise immunity and the use of solid state relays made the electronic control unit perform excellently in a potentially noisy environment, i.e., a high voltage spark source switching 4.5 kv across the electrodes and 115 v AC solenoid valves opening and closing.

2.4 Experimental Procedure

A standard run is characterized by the following sequence of events:

1. The shock tube is purged of gases other than room air;
2. The shutters are closed;
3. The diaphragm is clamped in a mounting ring and inserted into the shock tube;
4. The driver is pressurized to 0.014 atm below the bursting pressure;
5. The main switch on the control center is switched from the reset to start position;

6. The grids translate from the retracted position 1.14 cm toward the center of the turbulent mixer. The end of the stroke signifies time $t = 0$;

7. The normally closed solenoid valves in the supply lines to the plenum chambers open for 1500 msec;

8. The grids start to retract at $t = 1300$ msec;

9. The gas flow is turned off at $t = 1500$ msec;

10. The shutters are opened at $t = 1600$ msec;

11. The shock tube is fired at the desired time in the decay process of the density fluctuations; and

12. The spark gap is flashed when the shock wave arrives at the center of the optical windows.

2.5 Performance of the Experimental Facility

The turbulent mixer performed extremely satisfactorily and within the design criteria during the course of the experiments. Under normal operating conditions, as described in Appendix A7, the shutters open in 200 msec ± 0.5% and the grids translate 1.14 cm in and out of the sidewall in 400 msec + 0.5%. The time required to activate the solenoid valves in the gas supply lines is 4-8 msec according to the manufacturer's specifications. Each valve was found to be repeatable within 1 msec. The variation in arrival time of the weakest shock waves, $M_s = 1.007$, at the mixing zone was very small, less than 5 msec in 2000 msec for a typical series of runs. The knife blades, which are injected into the diaphragm, are mainly responsible for this accurate timing mechanism.

The stronger shock waves cannot be fired so accurately in time. The knife blades are stationary for the $M_s = 1.03$ and $M_s = 1.1$ shocks. Therefore, variations in the properties of the diaphragm material and, for mylar, humidity and temperature conditions in the laboratory influence the exact firing time of the shock tube. For runs made the same day, repeatability of the firing mechanism was acceptable within the design criteria. From one day to the next, the delay in channel 8 had to be adjusted to compensate for changing peripheral conditions. The shock wave strength in all three cases, however, was very repeatable, typically better than 1% in the Mach number.

The fluid mechanical properties of the turbulent mixer are discussed in Chapter V. Here it suffices to say that the overall performance of the experimental facilities justifies ensemble averaging to obtain statistical information regarding the interaction process between the shock wave and the scattering medium.

III INSTRUMENTATION

3.1 Scope

The instruments, which are described in this chapter, were used to meet the following objectives:

1. To characterize the scattering medium in the absence of a shock wave,
2. To investigate the modifications, if any, of the random field due to the interaction with the shock wave, and
3. To measure the scattered wave field.

The scattering medium was characterized using point density measurements, and optical techniques. Two aspirating density probes, as described in Section 3.2, were used to calculate mean values and rms fluctuations, as well as space-correlation functions and space-time correlations. Characteristic length scales in the density field could also be obtained from schlieren, shadowgraph and Fourier transform photographs, as explained in Sections 3.3 and 4.3. Furthermore, with the shock photographed in the center of the observation window, the scattering medium could be analyzed in front as well as behind the wave. The density probe was not suitable for this purpose because the test time, in the present experiment, is short compared with all but the highest frequencies in the fluctuating density field.

Statistical information regarding the scattered wave field was acquired using piezoelectric pressure transducers.

3.2 Aspirating Density Probe

An improved version of the Brown-Rebollo (Ref. 11) density probe was built and used to measure local point densities. A Standard constant-temperature hot-wire circuit, designed and built at Caltech by Drs. Anthony Perry* and Brian J. Cantwell**, was used to operate the hot wire in the probe. The response of the hot wire to a square-wave input indicates a wire frequency resolution of 100 kHz. Konrad (Ref. 14), using a similar density probe, found that the frequency response of the probe was at least 45 kHz.

In the present application the spatial resolution is a matter of definition. There is no appreciable mean flow over the probe, although the instantaneous flow velocity may reach 1-2 m/sec. Therefore, the spatial resolution is arbitrarily defined as the radius of a spherical sampling volume on which surface the in-flow velocity is equal to 1 m/sec. The mass flux through this surface corresponds to the sink strength of the sonic throat on the tip of the density probe. Based on this definition, the spatial resolution is 0.2 mm. A detailed account of the density probe construction and response estimates is given in Appendix B1.

3.3 Optical Measurements

3.3.1 Optical Processor

The properties of the optical apparatus used in these experiments can probably be best explained by describing a general form

---

*Reader, University of Melbourne, Australia

**Research Fellow, California Institute of Technology of optical processor in terms which will be useful in subsequent sections. This system consists of two double convex lenses which image a point light source from the focal plane of the first lens onto the back focal plane of the second one, which can be referred to as the optical Fourier transform (OFT) plane (cf. Fig. 3. 1). For the purpose of describing the system, without sacrificing the essential physics in the problem, the discussion will be restricted here to monochromatic sources. In principle, the results can be extended to polychromatic radiation, but the mathematics describing the setup becomes considerably more involved.

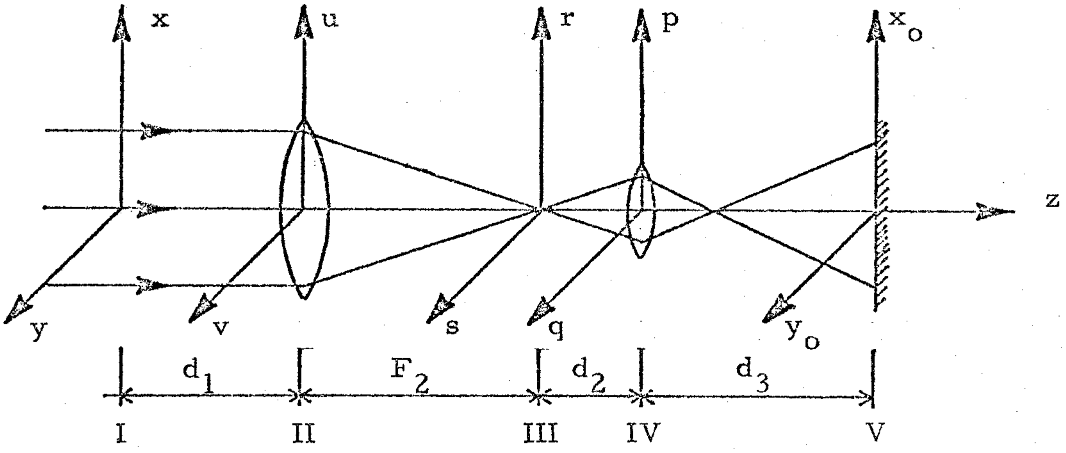

Figure 3. 1 Schematic of an Optical Processor

Consider the geometry of Figure 3. 1 with a rectangular coordinate system (x, y), (u, v), (r, s) and (p, q) attached to the planes I, II, III and IV, respectively. The object, located a distance d_1 in front of the lens, is illuminated by a normally incident plane wave of unit amplitude. The transmittance of the object is denoted by E_I (x, y), where the harmonic phase factor $e^{-i\omega t}$ is omitted. In plane III, the electric field amplitude can be computed (Goodman, Ref. 15) using diffraction theory and is given by

$$E_{III}(r,s) = \frac{1}{j\lambda F_2} \exp\left\{ i \frac{k}{2F_2} \left(1 - \frac{d_1}{F_2}\right)(r^2 + s^2)\right\}$$

$$\iint_{-\infty}^{\infty} E_I(x,y)\, P\left(x + \frac{d_1}{F_2} r,\ y + \frac{d_1}{F_2} s\right) \exp\left[-i \frac{k}{F_2}(xr + ys)\right] dx\, dy \tag{3-1}$$

where P is the pupil function for lens 2, i. e.,
$P\left(|x| > D_2/2,\ |y| > D_2/2\right) = 0$ and $P\left(|x| \le D_2/2,\ |y| \le D_2/2\right) = 1$.
Applying this same formula again to propagate the field distribution from plane III to plane V, $E_V(x_o, y_o)$ is found to be

$$E_V(x_o, y_o) = \exp\left\{ i \frac{k}{2F_3}\left(1 - \frac{d_2}{F_3}\right)\left(x_o^2 + y_o^2\right)\right\}$$

$$\iint_{-\infty}^{\infty} E_{III}(r,s)\, P\left(r + \frac{d_2}{F_3} x_o,\ s + \frac{d_2}{F_3} y_o\right) \cdot \tag{3-2}$$

$$\exp\left\{ - i \frac{k}{F_3}(r x_o + s y_o)\right\} dr\, ds$$

where again P is the pupil function for lens 3. In addition, if the camera focuses onto the object plane, then d_1, d_2, d_3, F_2 and F_3 are related by using the lens law:

$$d_3 = \frac{\left(d_2^2 - F_2^2 - d_1 F_2\right) F_3}{F_3 F_2 - F_3 d_2 - d_2^2 - F_2^2 - d_1 F_2} . \tag{3-3}$$

Combining equations 3-1, 3-2 and 3-3, $E_V(x_o, y_o)$ can be expressed in terms of $E_I(x,y)$ and geometrical parameters. The result of this calculation is not of immediate interest here, but will be presented for the OFT plane photography in Section 4. 3. 3, while in

3.3.2, 3.3.4 and 3.3.5, the above discussion will be used as a starting point for the treatment of the modifications of this basic scheme.

3.3.2 Schlieren System

The schlieren system is identical to that of the optical processor described in Section 3.3.1, except that the frequency content of the signal in the OFT plane is altered. This is accomplished by inserting a knife blade into the focal spot or by blocking the low frequencies with a dot. A knife blade with the cutting edge oriented parallel to the s coordinate and passing through the origin changes the limits of integration in equation 3-2 to the following:

$$E_V(x_o, y_o) = \exp\left\{\frac{ik}{2F_3}\left(1 - \frac{d_2}{F_3}\right)\left(x_o^2 + y_o^2\right)\right\}\int_0^{\infty}\int_{-\infty}^{\infty} E_{III}(r, s)$$

$$P\left(r + \frac{d_2}{F_3}x_o, \; s + \frac{d_2}{F_3}y_o\right)\exp\left[-i\frac{k}{F_3}(rx_o + sy_o)\right]dr\,ds \tag{3-4}$$

A dot with radius R centered around the origin modifies equation 3-2 to

$$E_V(x_o, y_o) = \exp\left\{\frac{ik}{2F_3}\left(1 - \frac{d_2}{F_3}\right)\left(x_o^2 + y_o^2\right)\right\}\int_R^{\infty}\int_R^{\infty} E_{III}(r, s)$$

$$P\left(r + \frac{d_2}{F_3}x_o, \; s + \frac{d_2}{F_3}y_o\right)\exp\left[-i\frac{k}{F_3}(rx_o + sy_o)\right]dr\,ds \tag{3-5}$$

where $r^2 + s^2 \geq R^2$.

Equations 3-1 and 3-3 are not altered as long as it is kept in mind that equation 3-1 is valid an infinitesimal distance upstream of the stops. Just behind these obstructions equation 3-1 is only applicable for either $r > 0$, in case of the knife blade, or $r^2 + s^2 > R^2$ for the dot with radius R. An account of the schlieren system that was specifically designed and built for this experiment is presented in Appendix B2.

3.3.3 Shadowgraph System

This method records the shadows cast by the object onto a photographic plate. The camera and second lens are replaced by a single photographic plate holder. The equations, 3-1 - 3-3, do not describe this system adequately. This configuration, however, has been analyzed in some detail by Taylor (Ref. 16), for the case of light propagating through turbulence. The schlieren setup, as described in Appendix B2, can be easily modified into a shadowgraph system by inserting a film plate holder between the object and the second lens.

3.3.4 Optical Correlator

Shadowgraph and schlieren pictures can be used to obtain space-correlation functions as first described by Uberoi and Kovasznay (Ref. 10). The method consists of making two identical transparencies of the original negative. The two copies are then placed back to face in an optical processor between the first two lenses. A photo detector is substituted for the camera and is located in the OFT plane. The two transparencies are matched, and the transmitted intensity is measured as a function of the displacement away from this position. Using the assumption of homogeneous and isotropic turbulence, the correlation function of the three-dimensional density field can be recovered.

The analysis for correlation functions obtained from schlieren pictures is given by Thompson and Taylor (Ref. 17), using ray optics, and an account of the physical setup of the correlator is given in Appendix B3.

3.3.5 Optical Fourier Transform Photography

Length scales of turbulence can also be obtained by positioning the photographic film in the OFT plane of the optical processor. Then equation 3-1 describes the electric field distribution from which the intensity can be computed using

$$I\ (r,s) = E_{III}\ (r,s) \cdot E_{III}^{*}\ (r,s) \qquad (3\text{-}7)$$

where the * denotes complex conjugation.

The analysis of the input response of the system with a slab of turbulence located between the two lenses is given in Section 4.3.3. As a result of that calculation, the size of the focal spot can be directly related to length scales in the scattering medium.

3.4 Pressure Measurements

3.4.1 Pressure Transducer Mounts

The Piezotronics PCB pressure transducers were found to be very susceptible to stress waves when mounted according to the manufacturer's specifications. In the shock tube, stress waves in the sidewall associated with the rupturing of the diaphragm reach the pressure gauges in the test section long before the shock waves do. Therefore, gauges would display an output signal ahead of the shock. This problem was especially severe for the smallest transducer, the 2.5 mm diameter PCB Model 105A. A solution was found by mounting the transducers in a plug which is illustrated in Figure 3.2. The central brass cylinder contains the pressure gauge and is vibration isolated from the wall in which it is mounted by a G.E. RTV 632 rubber ring. Grooves in the surfaces adjacent to the rubber, as well as small pins protruding out of the sidewall of the central brass cylinder, insure that the transducer remains in position under the pressure forces from the shock wave.

Seven transducers were used in the experiment. A Kistler pressure gauge, model 606A, was mounted in the 17-inch shock tube near the endwall. Just upstream of the mixing zone, a 2.5 mm PCB model 105A transducer was located in the sidewall of the turbulent mixer, using the above described mounting plug. Downstream of the scattering region, three PCB 113 A 21 gauges, one PCB 112 A 21, and one Kistler 606A transducer were mounted in a movable false endwall as indicated in Figure 3.3. With the Kistler gauge in the center, the PCB transducers were positioned 3.2 cm radially outward in a cross configuration. Four ∅ 1.25 cm standoffs located the plate with respect to the downstream shutter and provided sufficient vibration isolation to negate the need for the rubber isolation plugs. For the purpose of measuring the scattered wave field, the transducers in the false endwall were used, while the 2.5 mm PCB gauge registered the unperturbed incoming wave form. The Kistler sensor in the 17-inch shock tube sidewall provided the trigger pulse for recording the pressure signals on oscilloscopes.

3.5 Data Acquisition System

Short run times, typically 1.6 sec. for the entire experiment from start to finish, and the desire to reduce the density data on-line required the use of a high-speed data acquisition system. The GALCIT mobile computer-controlled data acquisition system, called Solo System, was used for this purpose. The Preston analog-to-digital converter (ADC) is capable of taking data with a resolution of 14 bits plus sign on 16 channels at a rate of $4\text{x}10^4$ conversions per second or $5\text{x}10^5$ conversions on a single channel. The Hewlett-Packard 2100 computer (32K memory) was used to acquire and reduce the data. Raw data, as well as reduced data, can be stored either on magnetic tape with a density of 1600 bits per inch, using the Hewlett-Packard read/write 7970E magnetic tape deck, or on a Hewlett-Packard magnetic disc 7901A. Peripheral devices with the system include a teletype and a Hewlett-Packard digital plotter 7210A.

IV. DATA ACQUISITION AND PROCESSING

4.1 Scope

Turbulence can only be described in statistical terms. Consequently, measurements must be averaged over a large number of realizations of the random field. Alternatively, when the ergodic theorem is applicable, time averaging may be substituted for ensemble averaging. Unfortunately, in shock tube research test times tend to be short. Therefore, emphasis has been placed on measurement techniques which obtain and store as many data as are conveniently possible per run. In this context, photographic methods are especially appealing because of their large space-bandwidth products. Furthermore, for the purpose of studying the scattering medium, the space-averaging property of these systems can be used advantageously, as explained in Section 4.3. For the data reduction of the point density measurements, a combination of time- and ensemble averaging was applied.

4.2 Point Density Measurements

4.2.1 Data Acquisition Procedure

All data are taken simultaneously with two aspirating density probes using a data acquisition scheme described in Appendix B4. The output of each hot-wire anemometer is connected to a differential amplifier. A DC offset is then subtracted from the probe output and the difference signal is amplified 10 times. After being filtered by a low-pass filter with an attenuation rate of 24 db per octave outside the pass band and a unity gain inside, the amplified signal is fed into the ADC of the Solo System.

One of the features of the ADC is that conversions take place under control of an external clock. For this experiment the clock signal is derived from a 20 kHz pulse train coming from a preset counter built into the Solo System. Based on this clock signal, data conversions take place on each channel at the rate of one per 100 μsec. Conversions can be prevented by an input to the ADC called BETA. If the BETA signal, which is derived from the electronic control system, is held false, no conversions will occur independently of the status of the signal on the clock line.

Data from the ADC are processed in the computer by a Fortran IV program. Input variables to the program are the number of records per tape file, the number of ADC channels, and the identification word for the run. An assembly-language subroutine, written by Prof. D. Coles, is used for data acquisition. It uses two data buffers of 4096 words each. While the second data buffer is filling, the first data buffer is being written onto magnetic tape, and so on. At the data rate of 20,000 conversions per second, no data are lost while writing gaps between records. The sequence of events comprising a typical run is now as follows:

1. The shutters are closed after the shock tube has been purged of foreign gas, and the program is initiated by feeding data characterizing the run into the computer. BETA is held false, and the preset-counter clock is running. The electronic control system is switch-programmed for the desired sequence of events with the main switch in the reset position.

2. After the run is started by flipping the main switch into

the run position, the grids move away from the sidewall. At the end of the stroke, BETA is made true and conversion in the ADC takes place until the preprogrammed number of records are written on tape. The program checks for format errors, i.e., whether or not a data block did end on last channel. No precautions are taken to detect or correct parity errors when writing.

3. At the end of the run, after the gas flow is turned off, the program starts processing the data. Resident in core is a calibration curve of a nondimensionalized density probe output $(V_{max} - V_p)/(V_{max} - V_{min})$ as a function of the concentration by volume of helium (see Appendix B1). V_{max} and V_{min} are the hot-wire anemometer output voltages for helium and freon-12 respectively, and they were measured twice a day by filling the mixing zone with either pure helium or freon-12. It was found that these values did not change within the experimental accuracy of the measurements as long as the hot-wire set was not turned off and the vacuum pump was not disconnected from the density probe. V_p, the output of the aspirating probe, is then transformed into a helium concentration. After the data are sorted into two blocks, one for each probe, the reduced data are written as a file on tape. Each standard file contains 16 records, which corresponds to a data acquisition time of 3276 msec. Occasionally a file contains 24 records, for instance during runs in which the shutters were not opened until $t = 3600$ msec. These data are used to analyze the effect of the opening of the shutters on the turbulent mixing process as discussed in Section 5.3.2. Finally, every 64th point

out of each record is plotted.

For each run, the maximum and minimum data points are computed, as well as the extreme values in every record, and then printed on the teletype. After a series of 16 good runs is completed, the data are further manipulated by calculating mean and rms values, as well as space-correlation coefficients and space-time correlations. Details of these calculations are presented in Sections 4.2.2, 4.2.3 and 4.2.4. Before the first, and after the last run of each day, all instruments are calibrated. No data are taken until all electronic circuitry has reached thermal equilibrium.

4.2.2 Computer Calculation of the Mean and rms Concentration Profiles.

For computation purposes, every reduced concentration data file containing q records of r words each is divided into k = q r/p intervals. The mean is calculated per interval and assemble averaged over N runs:

$$\bar{c}_k = \frac{1}{p\,N} \sum_{i=1}^{N} \sum_{j=(k-1)p+1}^{kp} c_{ij} \qquad 1 \le k \le \frac{qr}{p} \qquad (4\text{-}1)$$

where c_{ij} denotes the j-th data point in the i-th run. For a standard run p = 256, and q = N = 16. Using the computed mean, the rms deviation is calculated according to

$$m_{2,k} = \left\{ \frac{1}{pN} \sum_{i=1}^{N} \sum_{j=(k-1)p+1}^{kp} \left(c_{ij}^{2} - \bar{c}_k^{\,2} \right) \right\}^{\frac{1}{2}} \qquad 1 \le k \le \frac{qr}{p} \qquad (4\text{-}2)$$

4.2.3 Computer Calculations of the Cross- and Space-Correlation Functions

Consider two fluctuating concentration signals $c_1'(t)$ and $c_2'(t)$ with zero mean, measured by two density probes which are located a distance L cm apart. The signals are digitized and stored in a discrete data file. Each file contains n data words separated by the sampling time Δt. The cross-correlation function of $c_1'(t)$ and $c_2'(t)$ for a time lag $\tau = \ell \Delta t$ is defined by

$$R_{12}(\ell\Delta t) = \lim_{T\to\infty} \int_{-T/2}^{T/2} c_1'(t)\, c_2'(t+\ell\Delta t)\, \mathrm{comb}(\Delta t)\, \mathrm{rect}\left(\frac{t-\frac{n\Delta t}{2}}{(n-\ell)\Delta t}\right) dt \tag{4-3}$$

where ℓ is an integer $1 \leq \ell \leq n-1$,

$$\mathrm{comb}(\Delta t) = \sum_{i=-\infty}^{\infty} \delta(\Delta t - i) \tag{4-4}$$

δ is the Dirac delta function, and

$$\mathrm{rect}\left(\frac{t-\frac{n\Delta t}{2}}{(n-\ell)\Delta t}\right) = \begin{cases} 1 & \left| t - \frac{n\Delta t}{2} \right| \leq \frac{(n-\ell)}{2}\Delta t \\ 0 & \text{otherwise} \end{cases} \quad . \tag{4-5}$$

In the limit for $n \to \infty$ and $\Delta t \to 0$, equation 4-3 approaches the mathematical definition of the cross-correlation function for two continuous signals.

This calculation is based on fluctuating signals with zero mean. The experimental data with nonzero mean are therefore corrected by eliminating the low-frequency components. The mean value, which is calculated over 16 runs, is subtacted from the data in each run, and the nondimensionalized cross-correlation function is then computed using

$$R_{12,k}\,(\ell\Delta t) = \left< \sum_{j=1}^{n-\ell} \frac{\left\{c_1'\,(j\,\Delta t) + c_2'\,\left((j+\ell)\,\Delta t\right)\right\}^2}{Q} + \frac{\left\{c_1'\,(j\Delta t) - c_2'\,(j+\ell)\,\Delta t\right\}^2}{Q} \right> \qquad (4\text{-}6)$$

$$\text{and } Q = \left\{\sum_{j=1}^{n-\ell} \left(c_1'\,(j\Delta t)\right)^2\right\}^{\frac{1}{2}} \left\{\sum_{j=\ell}^{n} \left(c_2'(j\Delta t)\right)^2\right\}^{\frac{1}{2}}$$

where $\ell\Delta t$ is the time lag between the signals, and the brackets denote ensemble averaging. The space correlation $R(L, t)$ is obtained by computing $R_{12,k}\,(\Delta t)$ as a function of the separation L of the probes. The data used for the computations are the unreduced density probe signals. It is assumed that the output of the aspirating probe is linear with the concentration of helium. This assumption is justified for fluctuations of less than 10 percent around the mean. The advantage of this scheme is that the result of the computations is no longer dependent on the precise calibration curve for each probe.

4. 3 Optical Measurements

4. 3. 1 Measurement of the Shadowgraph and Schlieren Picture Correlation Function

The schlieren and shadowgraph pictures are taken with the optical system which is described in Section 3. 3. 3. The light source consists of a spark gap in an argon environment with a 0. 5 mm output aperture and a flash duration of a few microseconds. The argon atmosphere is isolated from air in the laboratory, which insures that the luminous intensity is very constant from shot to shot. Its intensity is sufficient to expose Tri-X-Pan 12.7 x 17.8 cm film. Standard development procedures using Kodak D-19 developer are then applied to obtain the negative. In the shadowgraph method, the actual light distribution is recorded in full size, while in the schlieren configuration, the object is reduced by a factor 2.2. For use in the optical correlator, which is described in Section 3.3.4, two transparencies are made of each shadowgraph and schlieren negative that is processed. The copies are obtained by illuminating the negatives with a collimated beam of white light from a point mercury arc source and imaging the negative onto 10 x 12.5 cm Kodak 4154 copy film. This film is processed in Kodak HC 110 developer according to the manufacturer's specifications. The image is reduced to record the physical object at 1/4 scale. The slides thus obtained are then placed back-to-face in the optical correlator, and the transmitted light intensity is measured as a function of the relative displacement.

4.3.2 Calculation of the Microscale for the Density Field Using the Shadowgraph Picture Correlation Function

Uberoi and Kovasznay (Ref. 10) first proposed the technique for obtaining three-dimensional space-correlation functions of a density field using two-dimensional space-correlation functions acquired from shadowgraph pictures. Their method principally relies on the assumption of a statistically homogeneous and isotropic flow. First, the correlation function measured in the optical correlator has to be provided with an ordinate. The peak in the curve corresponds to perfect alignment of the two transparencies and is denoted by 1, the normalized correlation coefficient. The position of the origin, which signifies zero correlation, cannot be directly measured. However, it can be shown (Ref. 10) that the first and third moments of the correlation function have to be zero for isotropic turbulence, if the light path through the medium is long compared with the integral scale

$$\int_0^\infty \beta(\xi)\, \xi\, d\xi = \int_0^\infty \beta(\xi)\, \xi^3\, d\xi = 0 \qquad (4\text{-}7)$$

where $\beta(\xi)$ is the measured picture correlation function. The correlation function for the flow can then be computed according to

$$R(r) = \frac{1}{8\pi D}\left(\frac{\rho_o}{kd}\right)\int_r^\infty \beta(y)\left[y\,\frac{2r^2 + y^2}{r}\cos^{-1}\left|\frac{r}{y}\right| - 3y\,(y^2 - r^2)^{\frac{1}{2}}\right]dy \qquad (4\text{-}8)$$

where ρ_o signifies the mean density, D denotes the thickness of the slab of turbulence, k is a constant associated with the photographic process, d is the distance between the density field and the photographic plate, and r is the displacement over which the correlation function is computed. In many cases though, the sole purpose of the correlation function is the determination of scales of turbulence. For that purpose equation 4-8 does not have to be computed. The integral scale L_ρ and the microscale, λ_ρ can be expressed immediately in terms of $\beta(r)$ from equation 4-8.

$$L_\rho = \int_0^\infty \frac{R(r)\,dr}{R(o)} = \frac{-\frac{\pi}{8}\int_0^\infty \beta(\xi)\,\xi^3 \log \xi\, d\xi}{\int_0^\infty \beta(\xi)\,\xi^2\, d\xi} \qquad (4\text{-}9)$$

$$\lambda_\rho^{\,2} = -\,2\,R(o)\,R''(o) = \frac{-6\int_0^\infty \beta(\xi)\,\xi^2\, d\xi}{\int_0^\infty \beta(\xi)\, d\xi} \qquad (4\text{-}10)$$

From equation 4-9 it can be seen that L_ρ depends principally on the behavior of $\beta(\xi)$ for large values of ξ; however, the correlation function is the least accurate there, mainly because the shadowgraph technique de-emphasizes the low wave number contribution that determines L_ρ. Therefore, it is to be expected that, using this method, the microscale is more accurately determined than the integral scale. For the purpose of studying the effect of the shock wave on the turbulence, equations 4-9 and 4-10 are not utilized, but the halfwidth and the distance between the first zero crossings of the central peak, the distance between the first minima as well as the average period of the outside lobes in the shadowgraph correlation function are used.

4.3.3 Calculation of a Length Scale for the Density Field Using Optical Fourier Transform Photography

The equations, which are presented in Section 3.3.1 to describe the properties of the optical processor, are based on diffraction theory. Using equation 3-1 as a starting point, the effective radius of the focal spot in a system with a slab of turbulence present between the two lenses can be computed. This calculation, which is valid for square aperture pupil functions, is lengthy. However, the wavelength of light is small compared with the smallest scale in the turbulence, $\lambda << \lambda_\rho$, and also $\sqrt{\lambda D} << \lambda_\rho$, where D is the thickness of the slab. Therefore, geometrical optics can be used as a valid approximation to diffraction theory. The calculation then becomes relatively simple and will be presented here.

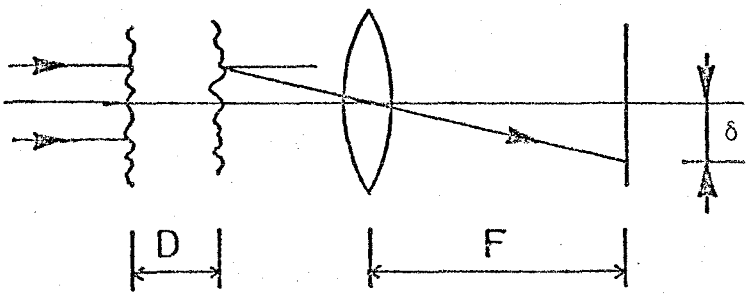

Figure 4.1 Optical Setup for Fourier Transform Photography

Consider the optical arrangement of figure 4.1. The scattering medium is characterized by a fluctuating index of refraction $n = 1 + \mu$, where $\mu << 1$, and a space-correlation function N. The mean angle of deviation of a ray from its initial direction is denoted by $\bar{\theta}$.

$$\bar{\theta} = 4K_1 D \tag{4-11}$$

where K_1 is a constant (Chernov, Ref. 1). In the case of isotropic scattering K_1 takes on the value

$$K_1 = -\frac{1}{2}\overline{\mu^2}\int_0^\infty \frac{1}{2}\frac{\partial}{\partial_r}\left(r^2\frac{\partial N}{\partial r}\right)dr \ . \qquad (4\text{-}12)$$

The mean radius of the focal spot in the presence of turbulence, R_{turb}, can now be computed simply using

$$\overline{\delta} = \overline{\theta}\cdot F \quad . \qquad (4\text{-}13)$$

Thus, by measuring $\overline{\delta} = R_{turb} - R_{noturb}$, the effect of the scattering medium on the impulse response of the system can be evaluated. The scale L_ρ can be computed from equations 4-11, 4-12 and 4-13 using an assumed shape for the correlation function N.

4.4 Pressure Measurements

4.4.1 Data Acquisition Procedure

All pressure signals are displayed on oscilloscopes and recorded on Polaroid 667 Land Film, and at the beginning of each day a calibration run is made.

Three different strength shock waves are fired, Ms = 1.007, Ms = 1.03 and Ms = 1.1, and the pressure transducers in the false endwall are stationed at two locations, 6.4 mm and 22.2 cm downstream of the scattering medium. For the weakest waves, 16 runs for each location of the false endwall are performed, while for the strongest shocks 8 runs are made.

Before each series of runs the gas flow control system in the turbulent mixer is checked and, if necessary, fine tuning is done according to the procedure described in Section 5.2.

4.4.2 Data Reduction Scheme for Pressure Signals in the Scattered Wave Field

All pressure data are obtained from oscillograms, of which a schematic trace and its important features is shown in Figure 4.2.

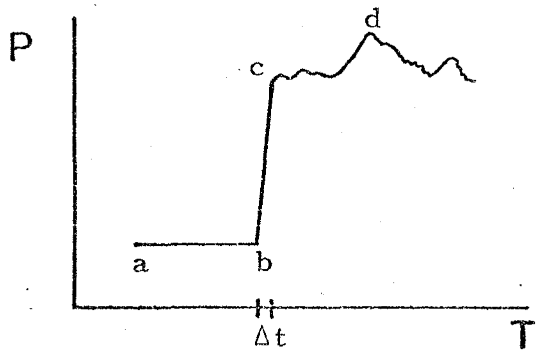

Figure 4.2 Schematic Pressure Profile

For each run, data from five transducers are obtained and used to characterize the scattered wave field. A sixth trace recorded the unperturbed incoming wave. The characteristic points in each signal are indicated by the letters a to d. The distance a-b denotes the arrival time of the wave front, measured from the point at which the three scopes are triggered simultaneously. The rise time, Δt, of the shock is determined by that portion of abscissa which is bounded by the intersection of the maximum slope at the wave front with line a-b on the one end and the intersection with a vertical line through point c, the maximum shock pressure, on the other end. The distance on the ordinate between b and c signifies the shock pressure. Sometimes a precursor compression precedes the shock wave. In those cases point b is taken to be the bifurcation point of the tangent to the shock wave and the actual measured pressure signature, as shown in Figure 4. 3.

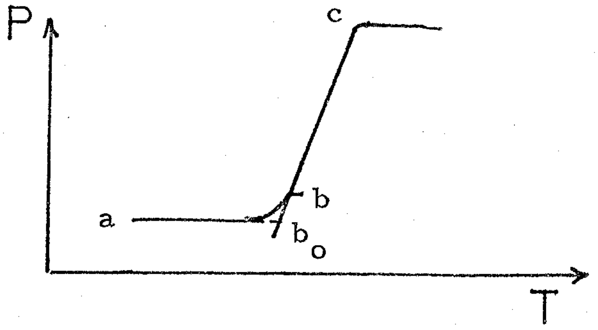

Figure 4. 3 Wave Front Showing Precursor

The arrival time in these cases is measured based on the the distance $a - b_o$. The peak pressure of the signal is denoted by point d and its lag behind the front by the distance between the projections of points c and d on the time axis. The measured shock and peak pressures are normalized using the unperturbed shock strength. The shock wave topology is calculated by subtracting t_{ab}, the time between points a and b measured with the gauge in the center of the false endwall, from the time t_{ab} which is recorded on the other four gauges. At the beginning of each day, the settings of the turbulent mixer were adjusted so that this time difference Δt_{ab} was zero for an unperturbed shock wave. The measured Δt_{ab} values for each transducer are ensemble averaged over either 16 runs for the $M_s = 1.007$ and $M_s = 1.03$ shocks, or 8 runs for the $M_s = 1.1$ waves, and the rms fluctuations are computed around this mean:

$$\sqrt{\overline{t'^2}} = \left\{ \frac{1}{N} \sum_{i=1}^{N} \left(t_i^2 - \bar{t}^2 \right) \right\}^{\frac{1}{2}} \qquad (4\text{-}14)$$

where N denotes the population of the ensemble, t_i the time difference Δt_{ab}, and $\bar{t}$ the first moment.

In some instances the pressure profiles show an overshoot in the shock pressure followed by an expansion as indicated in Figure 4.4. In these cases the width of the spikes Δt_s is measured in addition to the above mentioned characteristics.

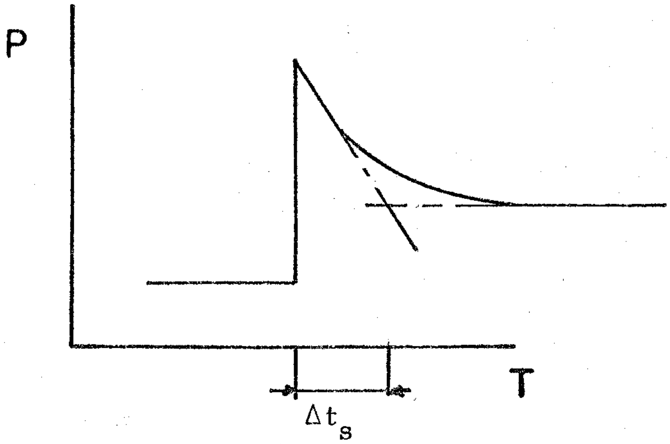

Figure 4.4 Schematic Pressure Profile Showing a Peaked Wave Front

V. CHARACTERIZATION OF THE SCATTERING MEDIUM

5.1 Scope

For the purpose of studying wave propagation through a random medium it may be helpful to consider the fluctuating density field as a random collection of irregularly shaped convex and concave lenses. Each lens is described by a characteristic length and an index of refraction. The random nature of the medium does not permit a detailed description based on individual elements, but rather a statistical description is necessary. In this context space-correlation functions describe the possible range of length scales in the turbulence, and rms density fluctuations characterize the magnitude of the index of refraction variations. An aspirating density probe is used to measure mean and rms fluctuations at different stations in the flow in the absence of a shock wave. With a pair of probes located a distance L apart, space- as well as cross-correlation functions are obtained.

Auxiliary information is acquired from shadowgraph, schlieren, and Fourier-transform photographs. Both correlation functions as well as length scales are determined by processing the pictures as described in Section 4.3. In addition, the optical techniques are utilized to describe the effect of the shock wave on the turbulence in terms of changes in length scales of the random medium.

5.2 Experimental Procedure for Tuning the Flow Control System

The mean density profiles, which are measured at locations indicated in Figure 5.1, form the basis for tuning the flow control system of the turbulent mixer. First, one probe is located in front of each grid (positions 2 and 3). The average density is calculated over 5 runs, and the pressure regulator settings in the supply lines are altered until both probes indicate the same mean concentration of helium to within ± 1%. The instruments are then removed, and a further test on the properties of the medium is performed by propagating a $M_s = 1.03$ shock through the mixing volume after the turbulent density fluctuations have completely decayed. The regulator settings are then adjusted until the recorded signals in the false endwall indicate that the shock wave has not been modified. This is a very stringent criterion. It verifies that the mean speed of sound is equal to that of air in the shock tube, and, at the same time, it substantiates that the mean acoustic impedance of the mixture is matched to that of air. In addition to the density and shock wave measurements, shadowgraph pictures are taken to qualitatively judge the statistical homogeneity and isotropy of the flow field. After the turbulent mixer is fine tuned, no further changes are made in the flow control parameters, and all measurements are performed on similar realizations of the scattering medium.

5.3 Results

5.3.1 Mean and rms Density Profiles

The purpose of the mean density measurements is to study the mixing process and to verify freedom from horizontal or vertical stratification. Vertical strata can result from buoyancy effects, as a result of the large difference in molecular weight of the two gases. Stratification in a horizontal plane can be caused by injecting different quantities of helium and freon-12 through the grids.

The important features of the mean density profiles are shown in Figure 5.2. The upper trace represents the mean concentration of helium by volume, while the bottom graph denotes the rms fluctuations as a function of time. At time t = 0, the jets are turned on for 1500 msec, as indicated by the tick mark to the left of the t = 1600 msec marker, while at t = 1600 msec, the shutters are closed. The shock is fired at approximately t = 1940 msec.

The triangles represent data obtained with two different probes, which were spaced a distance L = 1.09 cm apart, and located at measuring station 2 at a height of 13.3 cm above the bottom wall (see Fig. 5.1). The circles represent measurements which were acquired at position 1, 6.7 cm above the lower wall.

The important characteristics of the mean profiles can be explained as follows: Initially, the probe samples air in the test section, and the output voltage of the hot-wire anemometer has a value between the signal for pure helium and pure freon-12. However since the instrument is only calibrated for a binary gas mixture, the probe cannot distinguish air from a mixture of 50% helium and 50% freon-12, which would produce the same voltage output. The beginning portion of the curve does not represent the true helium concentration and should only be interpreted as an indication of the rate at which the air is flushed out of the mixing zone. From the graph it is clear that the steady-state concentration level is reached much earlier near the grids than in the middle of the box. This is not surprising because the center is a stagnation region, and the motion of the fluid particles in this vicinity is slower than for the gas elsewhere. Based on the flow rate through the supply lines, it is estimated that an amount of gas, equal to four times the volume of the mixing zone, is needed to reach the steady state level of slightly more than 80% helium. The equilibirum state is perturbed when the jets are simultaneously turned off. At that instant, all plena store the same volume of gas, but the pressure in the freon-12 tank is higher than in the helium reservoir, and furthermore, the helium is depleted at a faster rate. Consequently, the helium content of the injected gases becomes lower as time progresses. Later at t = 2500 msec, the newly reached steady state plateau drops again. This decrease in concentration is caused by air that has penetrated into the scattering medium after the shutters are opened.

The rms fluctuations show three corresponding regimes. The first peak is associated with the removal of air from the box, and the magnitude of the rms value decreases monotonically until the steady state value has been reached. The low level suggests that the turbulent mixing process is very efficient. This is partly due to the grid geometry, which enhances the mixing by bringing the two species into closer contact, and partly due to the long residence time of gas particles inside the scattering region. After the jets are turned off, the rms fluctuations again increase, mainly because the concentration of helium decreases with increasing time until the plena are depleted. In the final phase of the turn-off process, almost pure freon-12 is injected with a very low velocity through jets which are spaced 6.3 cm apart. During this phase the characteristic length scale ℓ_ρ in the process increases and so does the diffusion time τ based on ℓ_ρ^2/D_m, where D_m denotes the molecular diffusion coefficient for the two species. It is therefore expected that the rms fluctuation level will go up. This behavior suggests an alternative operating scheme for the turbulent mixer for the purpose of increasing the rms fluctuations, which, however, was not adopted for the present experiments. The test section can first be filled with pure helium and then freon-12 is injected for such a length of time that after the jets are turned off the average concentration is 80% helium by volume. However, in this method the flow control system cannot be tuned according to the scheme described in Section 5.2. Even after a long period of decay of the density fluctuations, the shock wave pressure profiles which are measured in the false endwall show a considerable modification of the unperturbed wave form. This indicates that large-scale gradients are still present in the scattering region.

In the conventional setup, in which helium and freon-12 are injected simultaneously through both grids, the mean concentration is measured at seven different locations, as indicated by stations 1 to 7 in Figure 5.1. The measurements are performed at three different height locations: the first one is 6.6 cm, the second 13.3 cm, and the third 19.9 cm above the bottom wall. Moreover at location 2, a depth survey is made by measuring the mean concentration at six different heights, as shown in Figure 5.3. For this purpose the mean concentration is calculated using only five runs per measuring station; the observed 2% variation in the mean value probably indicates constant density, within the accuracy of these measurements. Similarly, the mean concentration measured at the other locations is constant to within the same error margin. These results are confirmed using the arrival-time data, which are obtained from the pressure measurements of the scattered wave field.

5.3.2 Shutter Opening Effect

It is important to determine the perturbation on the decaying density field due to the opening of the shutters. The wake caused by the motion of the shutters tends to scramble the interface between the gas in the mixing region and the quiescent air in the shock tube. Furthermore, due to turbulent diffusion, air penetrates into the scattering region and a mixture of helium and freon-12 penetrates into the air. The extent of the transition region between the two media is studied by positioning one probe half way between the two horizontal sidewalls and 5.7 cm away from the perforated shutter face and another probe at the same height but 1 cm closer to the shutter. The measured mean profiles are shown in Figure 5.4. The squares denote the output of the probes when the shutters are opened at $t = 1600$ msec, while the stars represent data acquired when the shutters are activated at $t = 2600$ msec. The gas flow is terminated, in both cases, at $t = 1500$ msec. The shutter effect on the random field, indicated by the probe closest to the shutters and less pronounced by the probe further away, is considerable. The mean value drops by 20%, and the rms fluctuations increase almost tenfold. However, the effect of the turn-off mechanism of the jets by itself causes a 5% decrease in the mean level and a twofold raise in the rms fluctuations. The difference is due to air which has penetrated into the mixing zone.

This effect is apparently slightly less pronounced when the shutters are opened at t = 2600 msec. The motion of the fluid particles in the random medium has then subsided and the effect of the induced velocities, due to the rotation of the shutter blades, is slightly less. This is also noticeable in the rms curve. The graph denoted by 2 corresponds to the probe which is located 5.6 cm away from the shutters. At this location, the rms fluctuations have approximately two-thirds the amplitude of those measured 1 cm closer to the shutters. By moving the probes away from the shutter, it is found that the transition region extends approximately 8 cm into the mixing zone when the shock tube is fired. However, on the interface, both the mean density and speed of sound are matched, and thus the mean impedance is matched as well, and therefore the transition region should have little effect on the shock wave. This is confirmed by the pressure measurements, as indicated in Section 5.2.

5.3.3 Cross- and Space-Correlation Functions

A sample of the raw data used for the data reduction is shown in Figures 5.5 and 5.6. Figure 5.5 shows data taken during the time that the jets are on, and Figure 5.6 shows data after the jets are turned off. The separation between the probes is 1.51 cm. In either case, except immediately around t = 1700, the amplitude of the fluctuation is 4-5%, and the frequency content of the signals is less than 5 kHz.

Using the computation schemes indicated in Section 4.2, cross-correlation functions and space-time correlations are calculated, using the output of two probes which are located at position 6 in Figure 5.1. For four different separations of the probes, L = 0 cm, L = 1.09 cm, L = 1.51 cm, and L = 3.3 cm, the space-correlation coefficient is calculated over a period of 410 msec, starting at t = 1843 msec. These coefficients are then used to construct a correlation function. The exact shape is not of interest, only the integral length scale that can be obtained from it. The resulting graph is shown in Figure 5.7. Except near the origin an exponential function, with an exponent $x/2.2$ cm, seems to fit the four data points the best. Results obtained at other measurement stations look similar.

The cross-correlation functions are primarily calculated to obtain an indication of the flow velocities inside the box. A typical example is given in Figure 5.8. The velocity is calculated by dividing the distance between the probes by the time which is associated with the peak in the cross-correlation function. Typical velocities are 1.0 - 1.5 m/sec when the jets are in operation.

5.3.4 Length Scales Obtained from the Optical Measurements

Schlieren and shadowgraph pictures and Fourier transform photography are used to characterize the flow before it has been processed by the shock wave. The results obtained by Uberoi and Kovasznay (Ref. 10) show that the distance to the first minimum in the shadowgraph-correlation function is approximately equal to λ_ρ, the microscale for the flow. In this experiment, the smallest scale in the density field is based on the distance to the first minimum. However, the results have to be interpreted with caution. The analysis employed by Uberoi and Kovasznay is based on infinitesimal deflections of the light rays from the unperturbed paths and the distance from the film plate to the scattering region has to be large compared with the propagation length in the random medium. In the current experiments the film plate is positioned either seven (Fig. 6.15 and 6.16) or five (Fig. 6.17) thicknesses of the scattering medium away from the nearest window. The deviation of the light rays from the unperturbed path can be determined by considering the modifications of the perimeter of the optical window. The shadowgraph photographs (Figs. 6.15 and 6.16) indicate deviations of the order of 1-2 mm. For distances closer to the random density field, Taylor (Ref. 16) has calculated the shadowgraph intensity field, but his single scattering theory is not applicable in the current investigation. The parameter $k^2 \left\{\sqrt{\overline{\mu^2}}\right\}^2 L_\rho d \gg 1$, where $k = 10^7$ cm is the wave number of light, $\sqrt{\overline{\mu^2}} = 3 \times 10^{-5}$ the rms fluctuation in index of refraction, $L_\rho = 1.4$ cm is a characteristic length scale, and $d = 26.6$ cm the thickness of the scattering medium. The Born approximation is not valid and a higher order scattering theory is necessary to analyze the photographs. Moreover, the white lines in the shadowgraphs are probably caustics and near a caustic linear geometrical optics breaks down. However, in the neighborhood of the region where the caustics are first formed, the scale obtained from the shadowgraph pictures still corresponds to the length scale of the fluid elements which produced them. The microscale defined in this investigation as the distance to the first minimum in the optical correlation function is therefore not necessarily equal to the Taylor microscale, but is a measure of a small scale in the flow. An example of a shadowgraph picture correlation function is given in Figure 5.9. (This picture shows a shock wave, indicated by the dark line, moving from left to right; the correlation function is measured ahead of the shock.)

On the abscissa, the correlation distance is shown in millimeters for the full size picture, and on the ordinate the correlation coefficient is plotted. Correlation functions obtained from schlieren pictures look qualitatively very much alike. The results of these measurements are shown in Table 1. The position where the data were obtained is indicated by "before" and "after" and the signs // and ⊥ denote the direction in which the correlations are made with respect to the shock wave. Four alternative scales based a) the distance between the first minima, b) the full width of the central lobe at the 1/e peak value, c) the distance between the first zero crossings and d) the average period of the outside lobes, are listed in the four columns. Using these length scales, the effect of the shock wave on the random medium can be determined (cf. Chapter VII).

The optical Fourier transform pictures are taken with an optical bandpass filter (filter 466-3295 from Optics Technology, Inc.) in front of the light source. The pass band is 30 μm around 475 μm. The full aperture of the window is used to obtain the pictures. Without turbulence, the recorded focal spot is 0.8 mm. This diameter is increased to 3.1 mm by the presence of the random medium. The length scale, $L_\rho = 3.3$ mm, is then calculated according to equation 4-13, using a 3% rms fluctuation in the concentration of helium. This scale agrees with the results obtained from the shadowgraph correlations and therefore must be related to the small scale in the turbulence. This is not surprising since small lengths in the object plane produce wide spectra in the Fourier transform plane.

5.4 Summary of the Results Characterizing the Selected Scattering Medium

The random density field at approximately $t = 1900$ in the decay process is characterized by the following parameters:

The mean concentration of the mixture by volume is

C(He) = 80%;

C(Freon-12) = 20%;

The rms concentration fluctuations are approximately 3%;

The acoustical index of refraction is $n = 1 \pm 0.066$;

The optical index of refraction is

$n = 1.00024073 + 3.0683 \times 10^{-5}$;

The microscale $\lambda_\rho \approx 1.5$ mm; and

The integral scale $L_\rho \approx 1.4$ cm.

VI EFFECTS OF THE SCATTERING MEDIUM ON THE SHOCK WAVE

6.1 Scope

The scattered wave field is investigated using pressure transducers downstream of the scattering region and optical techniques inside the random medium. The objective is to document the characteristics of the acoustical field and to try to understand the physical processes that cause the modification of the incoming wave. In this section, the anatomy of the pressure signatures is presented. It is shown that the design of the experiment has successfully insured that the effects of the mean properties of the scattering medium on the shock are small and that the observed modifications are caused by the random field. The shock wave front, as shown on the pictures, seems to break up, and evidence of this effect is found in the pressure signatures also. The presentation of the data is in the form of histograms based on the characteristic features of the signals as explained in Section 4.4.1.

6.2 Representative Pressure Data Profiles

In figure 6.1, the effect of the decay time of the density fluctuations on the shock is shown. The traces represent the signals measured by the two PCB Model 113A 21 pressure transducers in positions 1 and 2 of the false endwall (see Fig. 3.3). The measuring station is near the downstream shutter. The abscissa on the oscillogram represents the time and the ordinate indicates the pressure. The Mach number of the incoming wave is $M_s = 1.03$. The picture to the left shows the response of the transducers if the shock wave is fired 2.4 seconds after the jets in the turbulent mixer are turned off. In these experiments, the shutters are opened at t = 3600, just before shock arrival at t = 3940 msec. The modification of the unperturbed profile caused by the mean density is small. The high-frequency fluctuations immediately behind the front are due to ringing of the transducers at the resonance frequency. The longer wavelength perturbations are mainly diffracted waves from the small gaps between the shutter blades and the sidewall of the turbulent mixer and indicate the signal-to-noise ratio for the subsequent scattering measurements. It is concluded from pictures like this one that the mean properties of the scattering medium, and the interface between the quiescent air in the shock tube and the helium-freon-12 mixture in the turbulent mixer do not significantly modify the unperturbed shock-wave profile.

The effect of the turbulence on the incoming wave form is shown in the picture on the right of Figure 6.1. The traces are obtained during a standard run as described in Section 2.4. The signals are measured with the same transducers and at the same measuring stations but indicate a significant alteration of the wave form. The portion of the wave front displayed on the top trace represents an increase in the shock strength followed by an expansion and a slow compression. The bottom trace indicates that the signal arrived earlier at transducer 2 than at 1 and that the frequency content of this front is considerably lower than for the one on the top trace. No pressure overshoot is observed in this portion of the wave, and the leading pressure jump is followed by a compression which increases the pressure, on the average, to the unperturbed value. This oscillogram indicates that for a given run the pressure signatures can be very different at different locations on the wave front. This is true for most of the data; but sometimes two or more traces in a run look alike to some degree, which indicates that scales of the order of the separation between the gauges may be important in the scattering process. A cross-correlation function, computed for pressure signals which are measured at different separations between the gauges, may in fact be very useful in determining the dominant scale in the turbulence that is important for the scattering process. Manual data processing is not very suitable for this purpose, and this is the reason that the calculation has not yet been performed in this research.

The time quoted in this section for rise times, wave separations, etc., can be related to possible effects of the random medium by bearing in mind that the time taken for a soundwave (or weak shock wave) to traverse one correlation length ($L_\rho = 1.4$ cm) is 40 μsec or one microscale ($\lambda_\rho = 1.5$ mm) is 4.2 μsec.

To illustrate the extent of the modifications, a representative series of oscillograms is shown in Figure 6.2. The traces represent the three cases, $M_s = 1.007$, $M_s = 1.03$ and $M_s = 1.1$. The numbers 1 through 4 on the right hand side of the page indicate the location of the transducers in the false endwall. The two oscillograms for each Mach number are obtained during the same run.

For the $M_s = 1.007$ case, trace 1 shows three discrete pressure jumps in the initial portion of the wave form. It is possible to interpret these jumps as representing a succession of three shocks. Trace 3 probably shows a succession of two shocks, separated by 24 μsec, but the rise time of the second shock is considerably longer than that of the initial one. The front on trace 4 may also be composed of three shocks, but their amplitudes are small, so they are somewhat difficult to distinguish.

For the $M_s = 1.03$ case, the second trace is of interest because it shows a sharp peak at the front, followed by an expansion. Traces like this one can also be observed for focusing shock waves, as shown by Sturtevant and Kulkarny (Ref. 18). This does not imply that this trace necessarily represents a focusing wave, but it is a possible interpretation. Trace 3 also shows an overshoot of the shock pressure, and trace 4 indicates two shocks, one trailing behind the other. The apparent change in rise time of the two shocks can possibly be explained by the oblique angle at which the shock approaches the transducer, as explained in Section 6.3.4. The picture also shows a typical arrival-time difference between the four signals. For the $M_s = 1.1$ case, the signatures look very similar except that the magnitude of the perturbations is reduced. The second trace shows very clearly two shocks with very rapid rise times.

6.3 Characteristics of the Scattered Wave Field

6.3.1 Shock Amplitude Results

The definition of the strength of the shock wave is given in Section 4.4.2. In most cases this criterion is perfectly adequate to determine the shock amplitude. However, for the weakest waves, the classification of precursors which are sometimes observed ahead of the first front is somewhat arbitrary. For the M_s = 1.007 shocks, 7 profiles from a total of 64 measured near the downstream shutter show precursors, and 11 profiles from a total of 64 measured near the endwall indicate precursors. For the stronger waves they do not occur. In other shock-wave phenmena, precursors have been observed. Sturtevant and Kulkarny (Ref. 18) found that after a shock wave has passed through a focus, diffraction waves run ahead of the shock. Abd - El-Fattah, et al. (Ref. 19) observed precursor shock waves for the refraction of plane shocks at an interface of gases with largely different sound speeds. In both cases, the precursors are associated with folded wave fronts. On the other hand, this initial portion of the signature can also be a genuine part of the shock wave structure. In this work a subjective criterion has been established (Section 4.4.2) to identify precursors. Table 3 is a list of those traces in which precursors are found.

The results of the shock amplitude measurements are shown in Figures 6.3 and 6.4. The sample population is 64 for the M_s = 1.007 and M_s = 1.03 shocks and 32 for the M_s = 1.1 shocks.

Bars to the left of the zero line indicate attenuation of the shock front, while the bars to the right imply amplification.

For all cases (except for the $M_s = 1.1$ measurements near the downstream shutter) the average normalized shock strength is less than 1. This indicates that energy is scattered out of the wave front. The $M_s = 1.1$ case is probably not an exception but a peculiarity due to the low sample population. However, by calculating the mean value of the pressure for times up to 140 μsec behind the front, it was found that the ensemble averaged value is indeed equal to the unperturbed shock strength within the accuracy of the calculations. Because the observations are made downstream of the scattering volume this implies that apparently very little energy is scattered backwards toward the diaphragm station.

Due to nonlinear effects, perturbations behind the shock will tend to catch up with the front. This mechanism channels energy back into the shock, which is apparent from the histograms; the value for the minimum normalized shock amplitude increases with increasing Mach number, as shown in Figures 6.5, 6.6. The maximum shock over-pressure, on the other hand, decreases with increasing Mach number. The detailed explanation of this effect can be given in terms of focusing shock waves. Sturtevant and Kulkarny (Ref. 18) showed that for focusing shockwaves the maximum shock amplification decreases for stronger shocks. This is due to nonlinear effects which increase the size of the focal volume, and distribute the energy over a larger portion of the shock front. Similarly, pressure perturbations caused by impedance fluctuations will be smoothened by nonlinear effects (Whitham, Ref. 20), even if the wave front is not curved.

6.3.2 Peak Amplitude Results

The peak amplitudes are normalized by the unperturbed shock strength and the results are shown in Figures 6.7 and 6.8 . Figure 6.7 displays the histograms for the peak pressures measured near the downstream shutter and Figure 6.8 shows the results for the pressure profiles acquired near the shock tube endwall. The histograms indicate that all peak pressures are larger than or equal to the unperturbed shock strength. This is consistent with the fact that the average amplitude of the pressure signature behind the front is, within the accuracy of the measurements, equal to the strength of the unmodified shock, while, by definition, the peak pressure is larger than or equal to the mean value. For all Mach number cases, except for the $M_s = 1.03$ signatures measured near the shock tube endwall, the value of the most probable nondimensionalized peak pressure is 1.25.

From a comparison between the histograms for the normalized shock- and peak amplitudes (Figs. 6.3, 6.4, 6.7, 6.8) it is deduced that the largest peak pressure occurs <u>on</u> the wave front for the $M_s = 1.007$ and $M_s = 1.1$ shocks and <u>behind</u> the front for the $M_s = 1.03$ case. The time lags between the peak value and the wave front for the different Mach number cases are shown in Figures 6.9-6.10. The histograms indicate that the peak value occurs with highest probability within an interval of 20 μsec behind the front. The probability that the peak is observed farther behind the initial portion of the wave decreases with time but seems to increase again after t = 100 μsec for the $M_s = 1.03$ shocks.

This result is as yet not understood. For the $M_s = 1.1$ shocks not enough data has been obtained to determine a definite trend, and it is therefore not possible to determine whether or not this phenomenon is real or due to the extent of the sample population.

Finally, Figures 6.5 and 6.6 show that the maximum normalized peak pressure decreases slightly with increasing Mach number.

6.3.3 Shock Wave Front Topology Results

The results of the rms arrival-time fluctuations are shown in Figure 6.11. This result reveals the effect of the scattering medium on the shock wave topology. The fluctuations in index of refraction tend to accelerate and decelerate the front in a random fashion, and consequently, the arrival time of the wave front measured by the gauges in the false endwall is different than for an unperturbed front. Nonlinear effects, on the other hand, tend to straighten and stabilize the wave front, so reducing the dispersion of arrival-time data. Nonlinearity also explains why the rms fluctuations in the arrival time decrease with increasing Mach number. Also, after the shock has passed through the scattering medium, and is propagating in uniform air, nonlinear effects further decrease the ripples on the wave front. The rms fluctuations of arrival time, measured near the shock tube endwall station, should therefore be smaller than those obtained near the location of the downstream shutter, and the percentage decrease is expected to be the largest for the strongest shock. Neither of these changes is observed in our experiments; the reason is as yet unknown.

The mean value for the arrival time difference between the top and bottom gauge (3 and 4 in Figure 3.3) and the mean value for the arrival time difference between the horizontal gauges (1 and 2 in Figure 3.3) are tabulated in Table 4. The results indicate a slight vertical stratification. The maximum mean arrival time difference between the top and bottom gauge is 14.9 μsec, which corresponds to a 1.5% variation in the acoustical index of refraction.

6.3.4 Wave Front Thickness Results

The shock wave rise time is based on the maximum slope thickness as described in Section 4.4.2. The results are shown in Figure 6.12. The minimum value is limited to 1 μsec by the time response of the pressure gauge. The rise time implied by the thickness of the weakest shock in these experiments is calculated to be approximately 0.1 μsec, so a change in the thickness of the wave of one order of magnitude cannot be detected. However, Figure 6.12 shows that in 13 out of 64 of the traces recorded in these experiments rise times of from 4 to 10 μsec were observed. A measured rise time larger than the resolution of the pressure gauges can be accounted for by either a change in the shock wave structure or, possibly, by geometrical effects associated with the approach of the shock to the transducer.

Geometrical Effects. Geometrical effects which can cause an apparent increase of rise time include tilt of the shock wave away from the plane of the transducer and wrinkling of the shock front on a scale smaller than the diameter of the transducer. Consider first the effect of the shock wave tilt suggested by the measurement of the mean arrival time difference between any two transducers, tabulated in Table 4 . The largest mean arrival time difference has a value of 14.9 μsec between the top and bottom gauges. The separation between the transducers is 6.3 cm. This implies that the mean rise time caused by an obliquely arriving shock wave on a 5 mm diameter gauge, if the scale of the perturbations on the shock is no less than 6 cm, cannot be more than 1.2 μsec. Therefore, mean large-scale geometrical effects cannot explain observed rise times greater than the time response of the pressure gauges.

However, it might be possible for the tilt of any individual shock wave at a transducer to be large enough to explain the occasional large rise time observed. The maximum time separation in a single run between the signals on the center gauge and any of the other transducers is 20 μsec (run 4670) acquired near the downstream shutter and is 24 μsec (run 4708) measured near the shock tube endwall. If we assume that in these infrequent events the half-wavelength of the perturbations on the shock happens to be coincident with the gauge separation in such a way as to give maximum arrival-time difference, and also that the largest values of observed rise time are due to arrival of the most tilted portion of the same perturbed fronts at a single transducer, then we obtain 5 μsec for the estimate of the largest possible rise time at the downstream shutter location and 6 μsec near the shock tube end wall. This estimate compares favorably with observed maximum rise times of order 4-8 μsec. Thus, at least in a few cases, shock wave tilt can explain long rise times.

A difficulty in interpreting the observed rise times in terms of geometrical effects arises from the fact that the measured rise times near the endwall of the shock tube look similar to those obtained near the downstream shutter. Consider Figure 6.13. A shock wave moves from top to bottom in the figure, and a pressure transducer can be located at plane I or II.

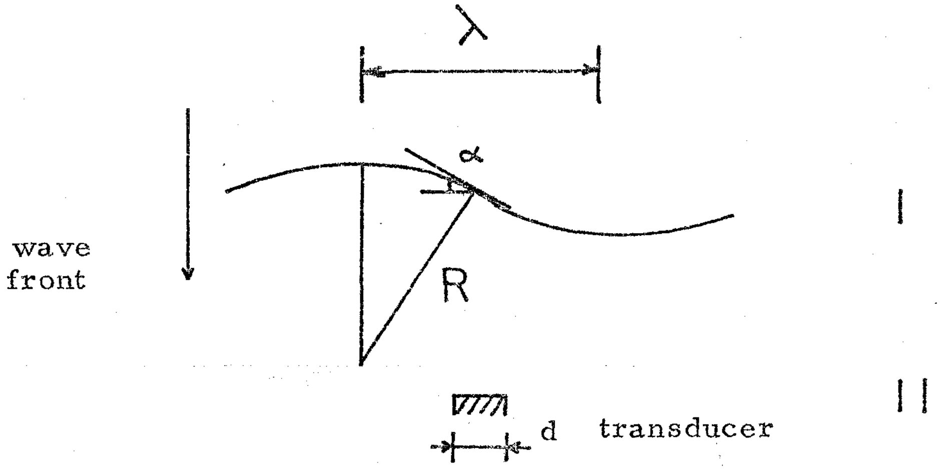

Figure 6.13 Geometrical Effects on Shock Wave Topology

Perturbations on the shock have a lateral scale λ and are of such an amplitude as to give a radius of curvature R. The size of the transducer d is small compared with λ. We suppose that the slope of the wave α determines the apparent rise time of the transducer in plane I. Following the propagation of the shock to plane II according to geometrical acoustics, if the radius of curvature R is less than one-half the propagation distance between I and II, the slope α on the transducer in plane II must be smaller because the radius of curvature has increased. Consequently, the apparent rise time due to tilt must have decreased. Only in the limiting case, when the radius of curvature is equal to one-half the distance between planes I and II, will the measured rise time at II be the same as at I. In the present experiments, the propagation distance between I and II is 22 cm, so perturbations on the shock wave of 10 cm radius of curvature generated by inhomogeneities of scale 6 cm would exhibit the same apparent rise time at I as at II, but perturbations of significantly different scale would not.

Another mechanism that would explain unchanged rise times at plane II is the inverse of the process described at the end of the next paragraph; namely large-scale perturbations at I tending to focus on small scales (smaller than the transducer diameter) by a process that might be called the 'shadowgraph effect' from its familiar occurrence in optical shadowgraphy.

Another geometrical effect that can cause apparent rise times larger than those due to the actual shock structure is wrinkling of the shock front on a scale smaller than the diameter of the transducer. The 5 mm diameter of the pressure transducers used in these experiments is too large to resolve wrinkling of the shock front on the scale of, say, the micro-structure λ_ρ of the density inhomogeneities. A large array of transducers smaller than the microscale is presently being constructed in this laboratory, and experiments will soon be carried out to determine the small scale structure of the shock topology. It should be noted that in the case $\lambda << d$, the same apparent rise time should be observed at the shock tube endwall (plane II) as at the downstream shutter location (plane I); because, though typical wavelengths of the perturbations grow as the shock propagates according to geometrical acoustics, the separation between the initial and final disturbances on the crossed and folded wavefronts at II will remain the same as the amplitude of the initial perturbation on the shock at I.

Unfortunately, the shadowgraph and schlieren photographs provide no further clues about the apparent rise time of the weakest shock waves, $M_s = 1.007$, for, in this case, the shocks are indistinguishable from the turbulence (Figs. 6.15 and 6.18). For stronger shocks, the waves are visible in the schlieren photographs; but neither do the photographs show any high frequency ripples on the wave fronts, nor do the pressure traces show any long rise times.

Shock structure. The long rise times observed in a few of the present experiments would be explained if for some reason the thickness of the incident shock front had been increased by almost two orders of magnitude by the scattering process. A mechanism for this effect has been suggested and quantified by George and Plotkin (Ref. 6). Because the present experiments have not been conducted with sufficient resolution to determine the detailed topology of the shock front, it is not possible to resolve the question whether the long rise times observed in some of the results are due to thickening of the shock structure or to geometrical effects.

Nonlinear effects. The discussion in the last three paragraphs did not include nonlinear effects. A wave with thickness δ steepens to its equilibrium structure in a distance L

$$L \approx \frac{\delta}{2\,(M_s - 1)} \qquad (6\text{-}1)$$

where M_s denotes the shock Mach number. Using L = 22 cm and $M_s = 1.007$ in equation 6-1, δ is computed to be $\delta = 3.1$ mm, which corresponds to a rise time of 8.8 μsec. In other words, nonlinear steepening should reduce the observed rise time at the endwall station to the resolution of the transducer if small scale wrinkling or a genuine change in shock structure are responsible for the increase in rise time. The results shown in Figure 6.12 indicate that these mechanisms by themselves cannot explain the observations. Of course, combinations of geometrical effects and shock structure changes could explain the observed rise times near the shutter location.

6.3.5 Peak Width Results

The measured values for the width of the peak immediately behind an amplified shock front are shown in Table 5. A possible explanation for the spike width is given by Pierce (Ref. 7). The decrease in pressure behind the front is caused by diffraction waves from the edges of the disturbance of scale L which caused the ripple on the wave front. He finds that

$$\Delta t_{sp} \approx \frac{n'}{a_o} L \qquad (6\text{-}2)$$

where n' denotes the rms fluctuation in the index of refraction, and a_o is the speed of sound in air. Using $\Delta t_{sp} \approx 8$ μsec, $n' = 0.066$ and $a_o = 350$ m/sec, L is calculated to be L = 3.8 cm. The radius of curvature of the wave front ripple is given by

$$R \approx \frac{L^2}{\pi^2 \ell_m} \qquad (6\text{-}3)$$

where ℓ_m denotes the ripple amplitude. Using the rms arrival time fluctuations (Section 6.3.3) to calculate ℓ_m, it is found that $R \approx 8$ cm. Pierce also indicates that the spike width should be of the same order of magnitude as the ripple amplitude divided by the speed of sound. In the current investigation the rms arrival time fluctuations are of the order 5-6 μsec, and the spike width is approximately 8 μsec.

6.3.6 Schlieren and Shadowgraph Pictures

The effect of the scattering medium on the shock wave is observed by taking shadowgraph and schlieren pictures of the wave field inside the turbulence region. In the absence of turbulence, the shock wave is indicated by a single straight line in both the shadowgraph and schlieren photographs. (cf Fig. 6.14). The shadowgraph pictures are taken 1.7 m (Fig. 6.15 and 6.16) and 1.3 m (Fig. 6.17) away from the near observation window, and the picture is 1.3 x full scale. The schlieren pictures are taken with the camera focused on the central plane in between the two windows, and the flow field is printed in actual size. In both techniques, of course, the pictures show the integrated results along the path of the light rays in the turbulence.

Figures 6.15-6.17 show photographs of the three Mach number cases. Though the weakest wave is supposed to be in the center of the picture it cannot be observed inside the scattering region, presumably because the optical effect of the random density field overshadows that of the shock.

The two methods seem to show different aspects of the phenomenon. The schlieren pictures indicate that the wave front is broken up into a collection of fronts, but this could be caused by a single, wrinkled wave front with or without a slight tilt relative to the optical axis. The arrival-time data obtained from the pressure measurements indicate that the maximum apparent thickness due to tilt can be as much as 7mm. This could account for some of the structure observed in Figure 6.20 but it is unlikely that it is sufficient to describe all of the observations. Indeed, it also appears on the pressure traces that several waves are propagating in close succession. For example, in the $M_s = 1.1$ case this is clearly shown in run 4734 and for the $M_s = 1.03$ wave in run 4647; other examples are shown in the top trace of the upper right picture and the lower trace in the upper left oscillogram in Figure 6.2.

In the shadowgraph pictures, the wave field behind the front is almost completely obscured by the turbulence for the $M_s = 1.03$ waves but is somewhat more visible for the $M_s = 1.1$ shocks as a 1 cm wide band following the front. Individual wavelengths cannot be resolved due to the lower sensitivity of this method. The effect of the shock on the turbulence is discussed in Section 7.2.

6.4 Comparison of the Shock Front Topology Results with Geometrical Acoustics Theory

The objective of this section is to relate the measured rms fluctuations in arrival time for the $M_s = 1.007$ shocks to the properties of the scattering medium. The propagation of discontinuities is related to the propagation of high frequency sound waves (Whitham, Ref. 20) and is described by geometrical acoustics. Using this theory, consider the following: The propagation time for an acoustic wave through a random medium with an acoustical index of refraction $n = a_o/a$, where a is the local speed of sound and a_o the speed of sound in air at standard pressure and temperature, is given by

$$t = \frac{1}{a_o} \int_o^s n(x,y,z)\, dx \tag{6-4}$$

where s denotes path length of the rays through the scattering medium. The difference in arrival time of rays propagating through a nonuniform medium from those in a uniform medium is then given by

$$\Delta t = \frac{1}{a_o} \int_o^s \left(n - 1\right) dx \ . \tag{6-5}$$

Under the assumption of a homogeneous and isotropic scattering medium and for $n = 1 + \mu(x,y,z)$, where $\mu \ll 1$, equation 6-4 can be transformed into

$$\Delta t \doteq \frac{1}{a_o} \int_o^D \mu dx \tag{6-6}$$

where D is the thickness of the slab of turbulence.

Using standard mathematical techniques (Chernov, Ref. 1), equation 6-6 is expressed in terms of a correlation function N for the medium

$$\overline{\Delta t^2} = 2 \frac{\overline{\mu^2}}{a_o^2} D \int_o^\infty N\,d\,r \quad , \tag{6-7}$$

where the bar denotes ensemble averaging. Assuming a Gaussian correlation function,

$$N = e^{-r^2/L^2} \tag{6-8}$$

where L denotes a length scale in the random medium, equation (6-7) becomes

$$\overline{\Delta t^2} = \frac{\overline{\mu^2}}{a_o^2} L D \sqrt{\frac{\pi}{2}} \quad . \tag{6-9}$$

For small fluctuations, the quantities $\sqrt{\overline{\mu^2}}$ and $\sqrt{\overline{c'^2}}$ (where c' is the concentration of helium) are linearly related. For $\sqrt{\overline{c'^2}} = 0.03$, $\overline{\mu^2} = 4.36 \times 10^{-3}$. Using the following numerical values

$a_o = 346$ m/sec, and
$D = 35.2\ \ 10^{-2}$ m, and
$L = 1.4 \times 10^{-2}$ m

$\sqrt{\overline{\Delta t^2}}$ in equation (6-9) becomes

$$\sqrt{\overline{\Delta t^2}} \approx 15\ \mu\text{sec},$$

This calculated value is a little higher than the measured quantities (Fig. 6.11). The discrepancy can possibly be explained by nonlinear effects, which tend to steepen the wave, and of course the length scale

L can be varied widely over the range of scales. Using a scale L = 4 mm, the calculated result is very close to the observed values.

VII. EFFECTS OF THE SHOCK WAVE ON THE SCATTERING MEDIUM

7.1 Scope

The objective of this section is to study the effect of the shock wave on the random density field. For this purpose shadowgraph and schlieren pictures were taken and processed in the optical correlator. Only information regarding the scales of turbulence has been obtained. It is found that the strongest shocks alter the density field the most and that the changes cannot be explained by isotropic shock compression alone. The ratio of scales in the direction parallel and perpendicular to the shock is increased after the fluid has been processed by the shock.

7.2 Scale Changes in the Density Field Induced by the Shock Wave

7.2.1 Data Obtained from Schlieren Pictures

Two schlieren pictures, numbers 170 and 173, are analyzed for the $M_s = 1.1$ case. Picture 173 is shown in Figure 6.20. The shock is moving from right to left, and the bottom of the picture is closest to grid 2. The photographs are made in the schlieren system by blocking the low frequency components of the signal in the optical Fourier transform plane, as explained in Section 3.3.2. The pictures show the flow field in actual size, and the camera is focused on the central plane of the scattering volume. However, the depth of field is at least as large as the box size, so the pictures show integrated results along the path of the light rays in the turbulence.

Upon casual inspection, the pictures for the weakest shocks,

M_s = 1.007 and M_s = 1.03 (see Fig.6.18 and 6.19), do not exhibit any visible effect of the shock wave on the density fluctuations in the nonuniform medium. However, measured correlation functions from the shadowgraph pictures for M_s = 1.03 do show an effect on the turbulence, as shown in Table 1. The strongest shocks (M_s = 1.1, Fig. 6.20), on the other hand, obviously change the characteristics of the processed fluid substantially. The scales of the turbulence are reduced, and the medium has become more anisotropic.

For the purpose of analyzing these pictures, optical correlation functions are made in two directions. In front of the shock, the correlation function is obtained by sliding the two transparencies parallel to the wave, but no perpendicular correlation function can be obtained due to lack of space. Behind the shock, correlation functions are measured in both directions. The area over which the data are averaged is in all cases 3.2 cm in diameter. The characteristic scales which are obtained from the correlation functions are tabulated in Table 1. Table 2 shows the ratio of the scales behind and in front of the shock, where a negative sign indicates a reduction in size. The results show a substantial decrease of all scales. This may also explain the larger number of bright white lines in the photographs of the processed fluid. Smaller scales represent higher spatial frequencies in the object plane, and because the dot acts like a high-pass filter, these frequencies show up in the picture.

A measure of the anisotropy of the shock-compressed fluid is indicated by the data in Table 6. They document the clearly visible fact that the streaks seem to be aligned more parallel to the shock front than perpendicular.

The results cannot be explained solely on the basis of isotropic shock compression because the ratio of the densities for a $M_s = 1.1$ shock is only $\rho_2/\rho_1 = 1.16$, where ρ_1 denotes the density of the undisturbed fluid, and ρ_2 the density behind the shock.

The possibility of spurious optical effects due to boundary-layer action on the observation windows can also be ruled out. The boundary-layer thickness during the experiment is estimated to be approximately 0.1 mm; it is very unlikely that this layer, which is so thin in comparison to the box size (26 cm), can have such a pronounced effect. Furthermore, it is predicted that the boundary layers are actually laminar in these experiments.

Therefore, the visible effect of the shock on the random medium must be due to direct interaction of the shock wave with the turbulence. Though the details of this interaction are not yet understood, it is certainly related to the entropy-sound interaction described by Chu and Kovasznay (Ref. 21).

7.2.2 Data Obtained from Shadowgraph Pictures

The shadowgraph technique is sensitive to second derivatives of the density fluctuations and, therefore, tends to emphasize small scales. Thus, the results of measurements on schlieren and shadowgraph pictures are not necessarily expected to be the same.

An example of a shadowgraph correlation function, derived from picture 98, is shown in Figure 5.9. On the abscissa is the displacement (of the full-size picture), and on the ordinate, the space correlation function. The contrast on the photograph to the left is artificially high and is caused by the copying process; negatives developed for use in the optical correlator show less contrast.

The shadowgraphs used for the correlation technique are pictures 97 and 98 for the $M_s = 1.03$ shocks and 184 and 185 for the $M_s = 1.1$ waves (Figs. 6.16-6.17). Photographs 97 and 98 are taken at a position 1.7 m and pictures 184 and 185 at a station 1.3 m away from the near observation window of the turbulent mixer.

The shock wave moves from right to left, and the photographs show the flow field enlarged by a factor 1.3. The weakest shock, $M_s = 1.007$, which is supposed to be located in the center of the picture (Fig. 6.15), is not visible because of the stronger optical effect of the turbulence. The $M_s = 1.03$ shock in Figure 6.16 does not change the turbulence characteristics in an obviously noticeable fashion, but the $M_s = 1.1$ wave does seem to alter the flow field. The correlation functions for pictures 97 and 98 are obtained ahead of and behind the shock by moving the slides parallel to as well as perpendicular to the wave. For photographs 184 and 185, the upstream fluid can only be characterized by correlation functions made parallel to the front. The area over which the correlation function is averaged is 3.2 cm in diameter.

For the $M_s = 1.03$ waves, the results in Tables 1 and 2 show that the fluid ahead of the shock is not completely isotropic. This is expressed by the ratio Γ, the quotient of the parallel to the perpendicular scale (see Table 6). In the unprocessed fluid, this ratio is less than 1. The length scale based on the width of the central lobe in the picture correlation function, which is probably the most accurately measured scale, indicates that the derivation from complete isotropy is approximately 4%. This could be due to the fact that the gases are injected into the box perpendicular to the axis of the shock tube and are taken out through the shutters, which at the window location causes a preferred direction parallel to the axis. After the fluid has been processed by the shock, the ratio Γ becomes larger than 1. This result is the same for all scales obtained from the measured correlation function except for that obtained from the period of the outside lobes. The effect of shock strength is also shown in Table 6. For the stronger waves ($M_s = 1.1$), the ratio Γ in the processed fluid is larger than it is for the weaker ($M_s = 1.007$) waves.

VIII. CONCLUSIONS

The conclusions of the study of propagation of weak shocks through a random medium are listed in the following paragraphs.

1. The experimental facility used in this investigation has performed very satisfactorily within the design criteria. The capability of characterizing the density field in the absence of a shock wave allows us to adjust the mixture in the test section so that both the mean density and the mean speed of sound match the values for air. The perturbations on the shock caused by the mean properties of the medium are therefore minimized.

2. The effect of the turbulence on the shock wave is considerable. The shock amplitude is modified, a random pressure field is generated behind the shock, and an apparent increase of the rise time of the initial disturbance is observed, possibly due to multiple folding of the wave front. Quantitative results are presented for four different characteristic features of the pressure signatures: a) the shock strength, b) the shock rise time, c) the peak amplitude, and d) the time delay between the front and the peak amplitude.

a) The value of the observed shockwave amplitudes, which are normalized with the unperturbed shock strength, vary from .1 to 1.9 for the weakest incident wave. For stronger waves the minimum and maximum normalized pressures are progressively less widely dispersed about the undisturbed value, 1.0. Scattered waves tend to coalesce with the primary front by gasdynamic nonlinearity, a mechanism which tends to balance the attenuation of the wave by turbulent scattering.

b) The measured rise time for the $M_s = 1.007$ shock varies between 1 μsec, the time resolution of the transducer, and 10 μsec. At both measuring stations, one near the downstream shutter and one 22 cm further downstream, the result is the same. This observation can possibly be explained in terms of the geometrical theory of acoustic wave propagation. A tilt or ripple in the wave front can cause an oblique arrival of the wave on the gauge, which yields an apparent increase of rise time. It is shown that perturbations on the shock wave of 10 cm radius of curvature generated by inhomogeneities of scale 6 cm would exhibit the same apparent rise time at both measuring stations, but perturbations of significantly different scale would not.

Another geometrical effect that can cause apparent rise times larger than those due to the actual shock structure is wrinkling of the shock front on the scale of the micro structure λ_ρ of the density inhomogeneities ($\lambda_\rho = 1.5$ mm). Currently, a large array of small pressure transducers is being constructed in this laboratory, and experiments will soon be carried out to determine the small scale structure of the shock topology.

The long rise times observed in a few of the present experiments would be explained if for some reason the thickness of the incident shock front had been increased by almost two orders of magnitude by the scattering process. A mechanism for this effect has been suggested and quantified by George and Plotkin (Ref. 6). However a difficulty with this explanation is that nonlinear effects should steepen the wave into a sharp front with greatly reduced thickness during its travel from the shutter location to the endwall.

c) The maximum observed peak pressure, which is non-dimensionalized by the unperturbed shock strength, is 1.9, and this value decreases with increasing Mach number. The trend of the peak pressure with incident shock strength can be understood by considering the tendency of portions of the scattered wave fronts to focus. As shown by previous experiments on shock-wave folding, the overshoot in pressure profile is characteristic of focusing wave fronts. Near a focus the pressure rises sharply above the unperturbed value, the magnitude of the amplification depending on the strength of the wave and the initial curvature of the wave front. The curved wave fronts and the intersections of waves seen in the schlieren pictures, suggest that focusing of wave fronts indeed can occur.

d) The maximum peak amplitude decreases slightly with Mach number and is most likely observed within 20 μsec behind the front. The probability of finding the peak amplitude farther behind the front decreases with distance. However, the probability does not decrease monotonically but increases again beyond a certain time behind the front for the $M_s = 1.03$ case. This phenomenon is as yet not understood.

Based on the optical observations and the pressure signatures, it is concluded that wave fronts can break up under the interaction with turbulence. This can possibly be explained by wave folding due to focusing.

3. A formulation based on geometrical acoustics (Pierce, Ref. 7) indicates that wave front ripples of scale 4 cm and with radius of curvature 8 cm can cause peaked profiles with a spike width of 8 μsec. This implies that scales comparable to the integral scale in the scattering medium can be responsible for some of the observed over pressures. These scales are similar in size to those that would exhibit the observed rise time at both measuring stations (cf. VIII 2)).

4. The effect of the shock wave on the turbulence is demonstrated by the schlieren and shadowgraph photographs. The strongest shocks reduce the scales of turbulence in the shock-compressed fluid and the medium becomes more anisotropic; apparently a fluid element is stretched in a direction parallel to the wave front and compressed in the perpendicular direction. This visual observation is confirmed by quantitative data from the optical correlator.

In conclusion, it can be stated that data have been obtained describing the interaction of a shock wave with a random medium in a classical scattering configuration in which mean effects do not significantly affect the process. An attempt has been made to account for the important features of the phenomenon, but by no means have the data been explored for their full potential. This will be the subject of future research.

APPENDIX A. DETAILS OF EXPERIMENTAL APPARATUS

A.1. Elements in Turbulent Mixer

Figure A. 1 shows a top view and horizontal cross section of the apparatus, which is mounted at the end of the GALCIT 17-inch diameter shock tube. The shock wave moves from left to right. The transition section inside the 17-inch shock tube is called the cookie-cutter. The shutters are shown in the closed position. The jets in the vertical sidewalls are alternately in a checkerboard configuration (see Fig. A. 9) connected to the two plenum chambers. The $C\ CL_2\ F_2$ reservoir is connected to the jets in the sidewall by pipes inside the chamber.

Figure A. 2 shows the shutters in the closed position as viewed from the endwall. The units to the left and the right of the shock tube are the plenum chambers with the grid drive mechanisms removed. A more detailed view of the shutters, the shutter and grid-drive mechanisms and the grids is shown in Figures A. 3-A. 7 and A. 9-A. 11. A photograph of the four units which make up the turbulent mixer is shown in Figure A. 3. The units on the left and right form the shutter assembly and the two units in between are the plenum chambers with the grids. A black grid, mounted in the sidewall, is visible in the reservoir farthest away. On the right hand side of the plenum chamber in the front the white inlet pipe is visible. The four blocks mounted at the back of this reservoir are the lead screw assemblies. The drive mechanisms for the grids and shutters are not shown in this photograph. Figure A. 4 is a close-up picture of the shutter assembly in the opened position. The face plates of the shutter blades do not show the exhaust holes as indicated in Figure A. 7. The drive mechanism is also not shown. Figure A. 5 depicts a plenum chamber unit with the grid in the outward position away from the sidewall. The white pipes on the right-hand side are the inlets to the two reservoirs. Figure A. 6 shows a side view of the assembled turbulent mixer as mounted at the end of the 17-inch shock tube (located on the left). The vertical black cable cylinder in the front drives one grid and the shutters are shown in the opened position. The air piston on the upper left side drives a shutter. The two pieces of flexible tubing that are attached to it form the inlet and exhaust lines. The exhaust lines on the shutter blades themselves are removed. The wooden cover on the left constitutes a part of the enclosure around the turbulent mixer and optical system.

The four positions of the optical window in the mixing zone are indicated in Figure A. 12. The position for all the pictures used in this thesis is indicated by the solid line. The center is 10. 8 cm away from grid 2 and 13 cm from the upstream shutter. The centers at the four locations are separated by 5 cm in the transverse direction and 9 cm along the shock tube axis.

A2. Calculations of Mean Molecular Weight and Speed of Sound in a Binary Gas Mixture

The speed of sound in an ideal gas is given by:

$$a^2 = \left(\frac{\partial p}{\partial \rho}\right)_s = \gamma R T \qquad (A-1)$$

where $\gamma = c_p/c_v$, the ratio of the specific heats, R is the gas constant, s is the entropy and T the absolute temperature. For a mixture of two gases, 1 and 2, this ratio is

$$\gamma_{mix} = \frac{\alpha_1 c_{p1} + \alpha_2 c_{p2}}{\alpha_1 c_{v1} + \alpha_2 c_{v2}} , \tag{A-2}$$

where α denotes the mass fraction.

The gas constant is determined by

$$R_{mix} = \alpha_1 R_1 + \alpha_2 R_2 \tag{A-3}$$

Therefore, equation A-1 can be used to calculate the speed of sound in a mixture according to

$$a_{mix}^2 = \gamma_{mix} R_{mix} T = \gamma_{mix} (\alpha_1 R_1 + \alpha_2 R_2) T$$

$$= \gamma_{mix} \left(\frac{\alpha_1}{\gamma_1} a_1^2 + \frac{\alpha_2}{\gamma_2} a_2^2 \right)$$

$$a_{mix}^2 = \frac{\alpha_1 c_{p1} + \alpha_2 c_{p2}}{\alpha_1 c_{v1} + \alpha_2 c_{v2}} \left(\frac{\alpha_1}{\gamma_1} a_1^2 + \frac{\alpha_2}{\gamma_2} a_2^2 \right) \tag{A-4}$$

The molecular weight for a mixture is

$$M_{mix} = c_1 M_1 + c_2 M_2$$

where c denotes the concentration by volume.

A3. Drive Mechanism Grids

The power unit in the drive mechanism for the grids consists of a pneumatic cable cylinder (Tol-O-Matic, 3.8 cm bore) as shown in Figure A.10). The cable is connected to four leadscrew units through a system of chains and sprockets. The linear motion of the piston is transformed into a rotation and in the leadscrews this sequence is reversed. At the end of the stroke an air cushion decelerates the piston. In this fashion a very smooth operating system has been devised. The cable cylinder is activated by fast acting solenoid valves.

A4. Shutter Drive Mechanism

The shutter drive mechanism is shown in Figure A.11. It is a four linkage mechanism that is mounted at the sidewall of the turbulent mixer. The shutters are operated by the motion of the pneumatic linear actuator. In the retracted rod position the shutters are closed, as indicated in Figure A.11, by the dashed line. In the extended rod position, lever 1, which is connected to the shutter blades, has rotated 45°. At that position the angular velocity of the blades is zero and a further extension of the piston rod will reverse the direction of rotation.

A5. The Shock Tube Firing Mechanism

The shock tube firing mechanism consists of a high pressure vessel (11 atm. max pressure) which is connected through a 2.5 cm diameter pipe to the driver section of the GALCIT 17-inch shock tube. A bypass line with a metering valve (1 cm maximum opening) is used for small, accurate flow rates. A fast actuating solenoid valve starts and stops the flow into the driver. Inside the test section a small ϕ 4 cm pneumatic linear actuator injects the movable knife blades into the diaphragm. This piston is also activated by a solenoid valve.

A6. Electronic Control Circuitry

In Figure A.15, a schematic of a single channel is shown. An input trigger pulse is transmitted through an open collector inverter, which in turn triggers the SN74121 monostable vibrator. An external R.C circuit controls the duration of the output pulse, which is used for the delay signal. This chip can be completely bypassed and then the timer SN74121 is triggered immediately by the SN7406. The output of the timer is variable and is connected to a Teledyne solid state relay.

Appendix A7. Normal operating conditions

Following are the normal operating conditions for the Turbulent Mixer.

--He regulator pressure: $T_1 = 71$ psig; $T_4 = 56$ psig
--Freon-12 tank pressure: $P_0 = 60$ psig
--Grid drive regulator pressure: $P_g = 42$ psig
--Shutter drive regulator pressure: $P_s = 45$ psig
--Auxiliary tank pressure: $P_{aux} = 80$ psig
--Auxiliary flow time: $t = 250$ msec

APPENDIX B. INSTRUMENTATION

Appendix B1. Density probe

The density probe construction is shown in Figure A. 1. The instrument consists of a hot wire, $1.27\ 10^{-3}$ mm diameter, which is stretched across a small glass (0. 2 mm) capillary tube. The capillary tube is connected to a vacuum pump, and the flow through the nozzle upstream of the hot wire is sonically choked. The flow past the wire is then independent of the free stream velocity (to $0(M_\infty^2)$) and is only contingent upon the conditions at the throat. The output of the hot wire is therefore only influenced by the properties of the gas being sampled.

The probe is calibrated in a chamber in which the concentration of helium in a mixture with freon-12 can be controlled. The output of the hot wire is then measured as a function of the concentration of helium. These data are curve fitted and a calibration plot which relates the concentration to a nondimensionalized output voltage $(V_{max} - Vp)/(V_{max} - V_{min})$ is computed. V_{max} and V_{min} denote the hot wire anemometer output voltages for helium and freon-12 respectively. During an experiment this calibration curve is stored in the computer memory of the data acquisition system, the Solo system (see Section 4. 2. 1). The response of the hot wire to a square wave signal indicates a 100 kHz wire frequency resolution. The signal to noise ratio of the probe is sufficient to detect concentration fluctuations of ± 1%.

In this experiment there is no appreciable mean velocity over the probe although the instantaneous flow velocity may reach 1-2 m/sec. Therefore, the spatial resolution is arbitrarily defined as the radius of a spherical sampling volume on which surface the air inflow velocity is equal to 1 m/sec. The mass flux through this surface corresponds to the sink strength of the sonic throat on the tip of the probe. For a throat diameter of .025 mm, the spatial resolution is 0.2 mm.

Appendix B2. Schlieren system

A general purpose schlieren system for use with the GALCIT 17-inch shock tube was designed during the course of this experiment. The arrangement of the optical elements is illustrated in figures B.2 and B.3. Figure B.2 shows a side view of the optical system in relation to the turbulent mixer and the 17-inch shock tube. The first concave reflector is closest to the light source (Fig. B.3) and is used to obtain a collimated beam. The parallel beam is then reflected 90° downward, perpendicular to the observation windows. Another flat mirror reflects the light onto the second concave reflector, which focuses the beam onto the Optical Fourier Transform plane (OFT) (Fig. B.3). A camera is used to focus onto the object inside the turbulent mixer. Provisions are made upstream of the second reflector to accommodate a film plate holder for the shadowgraph configuration. In the OFT plane a knife edge or dot can be inserted into the beam to block a portion of the focal spot. Standard with the system is a high voltage spark gap (5 kV) and a continuous Hg vapour light source. The apparatus is suspended from a rail mounted on the ceiling of the laboratory and is vibration isolated from the shock tube facility. The unit is completely enclosed in a darkroom to facilitate daytime observations.*

The smallest scales in the turbulence that can be observed with the system is determined by diffraction effects. Scales of turbulence of order a diffract light of wave length λ at an angle

---

*The author wishes to thank Dr. Kulkarny for his assistance with the construction of the system.

$\theta = \lambda/a$. For the shadowgraph setup, the limiting aperture in the instrument is the film plate, and scales smaller than $a \approx 0.01$ mm are not visible because the light is not collected on the film but scattered out of the system. For the schlieren configuration the minimum observable scale is approximately $a \approx 0.005$ mm.

Appendix B3. Optical correlator

The optical correlator used for obtaining the shadowgraph and schlieren correlation functions is shown in figure B.4. An Hg vapour point arc source is placed in the front focal plane of a double convex achromat, which collimates the beam onto the two slides to be correlated. One slide is mounted in an Ardel kinematic positioning stage with three degrees of freedom (horizontal, vertical, rotational), and one slide is stationary. Upstream of the stages, an adjustable aperture controls the area over which the correlation is taken. The transmitted light is collected by a second double convex achromat and focused onto a photo detector. A flat mirror can be positioned between the detector and the second lens to image the two slides onto a viewing screen.

The experimental procedure to obtain a correlation function is as follows: two transparencies (36 mm slides) are made from the negative of interest. This is done by placing the original negative in a collimated light beam to assure uniform illumination. The two slides are then placed back-to-face in the optical correlator and the linear stages are used to align the slides. During this process, the slides are imaged onto a viewing screen.

After alignment the viewing mirror is removed and the position of the slides is fine tuned by moving the one slide until a maximum detector output is obtained. One slide is then translated relative to the other by a dc motor drive. The position of the movable slide is recorded by a precision 25 turn 500 Ω Beckman D series potentiometer. The spatial resolution of this system is

3 μm. The output of the detector and the position of the translational stage can be measured simultaneously to obtain a correlation function as shown in Figure 5.9. The actual physical set up is shown in Figure B.5 .

Appendix B4. Data acquisition system

The schematic of the data acquisition system is shown in Figure B.6. The output of the hot wire set, designed and built at Clatech by T. Perry and B. Cantwell, is connected to the input of a differential amplifier, Princeton Applied Research, model 113 A, and Instrument Amplifier 1, built at Caltech. A dc offset signal from Analogic model An 3100 is subtracted from each hot wire signal, and the difference is amplified 10 times. After being filtered by a low-pass filter with an attenuation rate of 24 db per octave outside the pass band (Kron hite 3202 A), the signal is fed into the ADC of the Solo System. For all data taken, the cut off frequency set on the filter is 5 kHz. The ADC is sampling at a rate of 10 kHz per channel.

TABLE 1

LENGTH SCALES OBTAINED FROM PICTURE CORRELATION FUNCTIONS

	Slide Number	Position of Correlation	Direction of Correlation	$\Delta \ell$ for 1st Minima (mm)	Full Width at 1/e Peak (mm)	$\Delta \ell$ for Zero Crossing (mm)	Period of Outside Lobes (mm)
SHADOWGRAPH	184	Before	//	3.03	1.26	2.46	2.33
		After	//	3.79	1.28	2.87	3.59
			⊥	3.79	.97	1.77	3.38
	185	Before	//	3.21	1.05	1.79	3.54
		After	//	4.38	1.41	3.10	3.15
			⊥	2.18	.90	1.49	2.69
	98	Before	//	2.23	.85	1.72	2.23
			⊥	3.79	.87	2.56	1.69
		After	//	3.03	.95	2.23	2.31
			⊥	2.82	.85	1.46	2.51
	97	Before	//	1.82	.77	1.38	1.56
			⊥	2.79	.82	1.51	1.95
		After	//	4.79	.95	2.08	1.97
			⊥	2.64	.95	2.05	2.08
SCHLIEREN	170	Before	//	10.9	2.15	8.38	5.18
		After	//	4.82	1.54	3.41	3.23
			⊥	3.51	1.13	2.10	3.23
	173	Before	//	7.69	1.87	4.23	6.62
		After	//	4.49	1.41	3.59	3.62
			⊥	3.33	1.31	2.87	2.21

TABLE 2

CHANGES IN TURBULENCE LENGTH SCALES INDUCED BY THE SHOCK WAVE

	Slide Number	Position of Correlation	Direction of Correlation	Change of $\Delta \ell$ (minima) (in %)	Change of Full Width (in %)	Change of $\Delta \ell$ (Zero crossing) (in %)	Change in Period of Lobes (in %)
SHADOWGRAPH	184	Before	//	--	--	--	--
		After	//	+25	+2	+17	+54
			⊥	+25	-22	-28	+45
	185	Before	//	--	--	--	--
		After	//	+37	+34	+73	-11
			⊥	-32	-15	-17	-24
	98	Before	//	--	--	--	--
			⊥	--	--	--	--
		After	//	+36	+12	+30	+3
			⊥	-26	-3	-43	+48
	97	Before	//	--	--	--	--
			⊥	--	--	--	--
		After	//	+163	+23	+50	+26
			⊥	-6	+16	+36	+7
SCHLIEREN	170	Before	//	--	--	--	--
		After	//	-56	-29	-59	-38
			⊥	-68	-48	-75	-38
	173	Before	//	--	--	--	--
		After	//	-42	-25	-15	-45
			⊥	-57	-30	-32	-67

TABLE 3

LIST OF TRACES WITH PRECURSORS

Downstream Shutter Location		Endwall Location	
Run	Trace No.	Run	Trace No.
4669	4	4684	1
4670	3	4688	4
4673	4	4689	4
4674	3	4691	4
4677	4	4694	1
4679	1,2	4698	1
		4701	1
		4703	2
		4708	1
		4709	2,4

TABLE 4

MEAN VALUE FOR THE ARRIVAL TIME DIFFERENCE BETWEEN PRESSURE GAUGES MOUNTED IN FALSE ENDWALL

	Shutter Location		Endwall Location	
	Gauge	Gauge	Gauge	Gauge
	$\Delta t_{ab,1}-\Delta t_{ab,2}$ (μsec)	$\Delta t_{ab,3}-\Delta t_{ab,4}$ (μsec)	$\Delta t_{ab,1}-\Delta t_{ab,2}$ (μsec)	$\Delta t_{ab,3}-\Delta t_{ab,4}$
M = 1.007	-2.46	+14.92	-2.06	+8.96
M = 1.03	- .82	- 7.31	5.25	5.56
M = 1.1	-3.0	+ 2.38	-5.13	+4.01

TABLE 5

PEAK WIDTHS BEHIND AMPLIFIED SHOCK

Mach No.	Position	Run	Peak Width (μsec)	Average (μsec)
1.007	shutter	4661	6	
		4663	7	
		4668	8	6.2
		4674	4	
		4678	6	
1.007	endwall	4687	5	
		4688	12	8.7
		4699	10	
		4703	8	
1.03	shutter	4589	10	
		4589*	10	10
		4593	8	
		4594	8	
		4603	14	
1.03	endwall	4720	6	23
		4722	40	
1.1	shutters	4743	8	
		4749	3	7
		4758	10	
1.1	endwall	4736	8	8

---

*Run 4589 showed two pressure profiles with a peaked wave front.

TABLE 6

CHARACTERIZATION OF THE ANISOTROPY OF THE SHOCK COMPRESSED FLUID

SHADOWGRAPH

Slide Number	Position of Correlation	$\Delta \ell$ for 1st Minima	Full Width at 1/e Peak	$\Delta \ell$ for Zero Crossing	Period of Outside Lobes
184	After	1.00	1.32	1.62	1.06
185	After	2.01	1.57	2.08	1.17
98	Before	.59	.98	.67	1.32
	After	1.07	1.12	1.53	.92
97	Before	.65	.94	.91	.80
	After	1.81	1.00	1.01	.95

The table lists values of $\Gamma = \frac{/\!/ \text{ scale}}{\perp \text{ scale}}$ based on the four characteristic length scales of the correlation function.

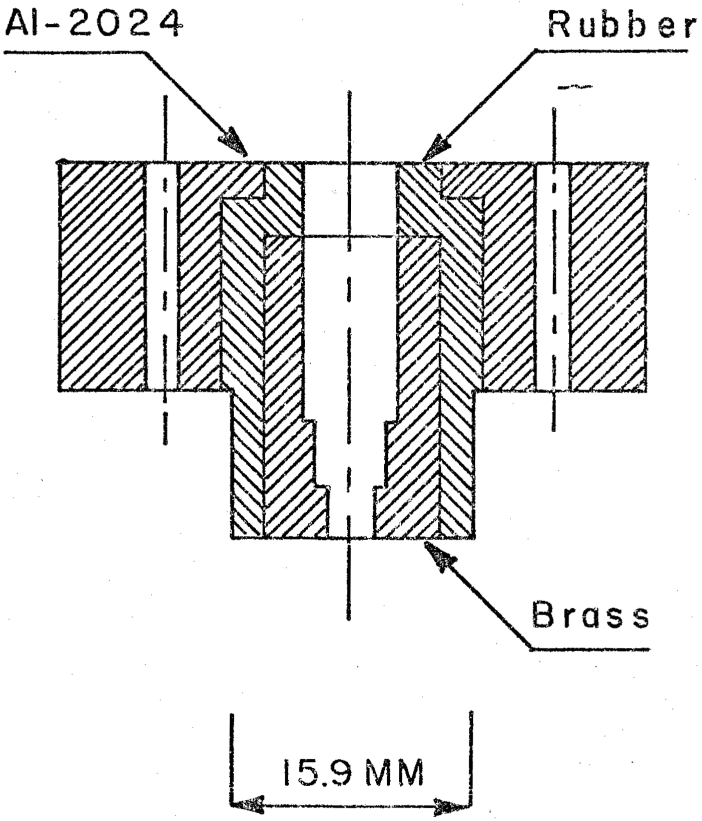

FIG.3.2 PRESSURE TRANSDUCER MOUNTING PLUG.

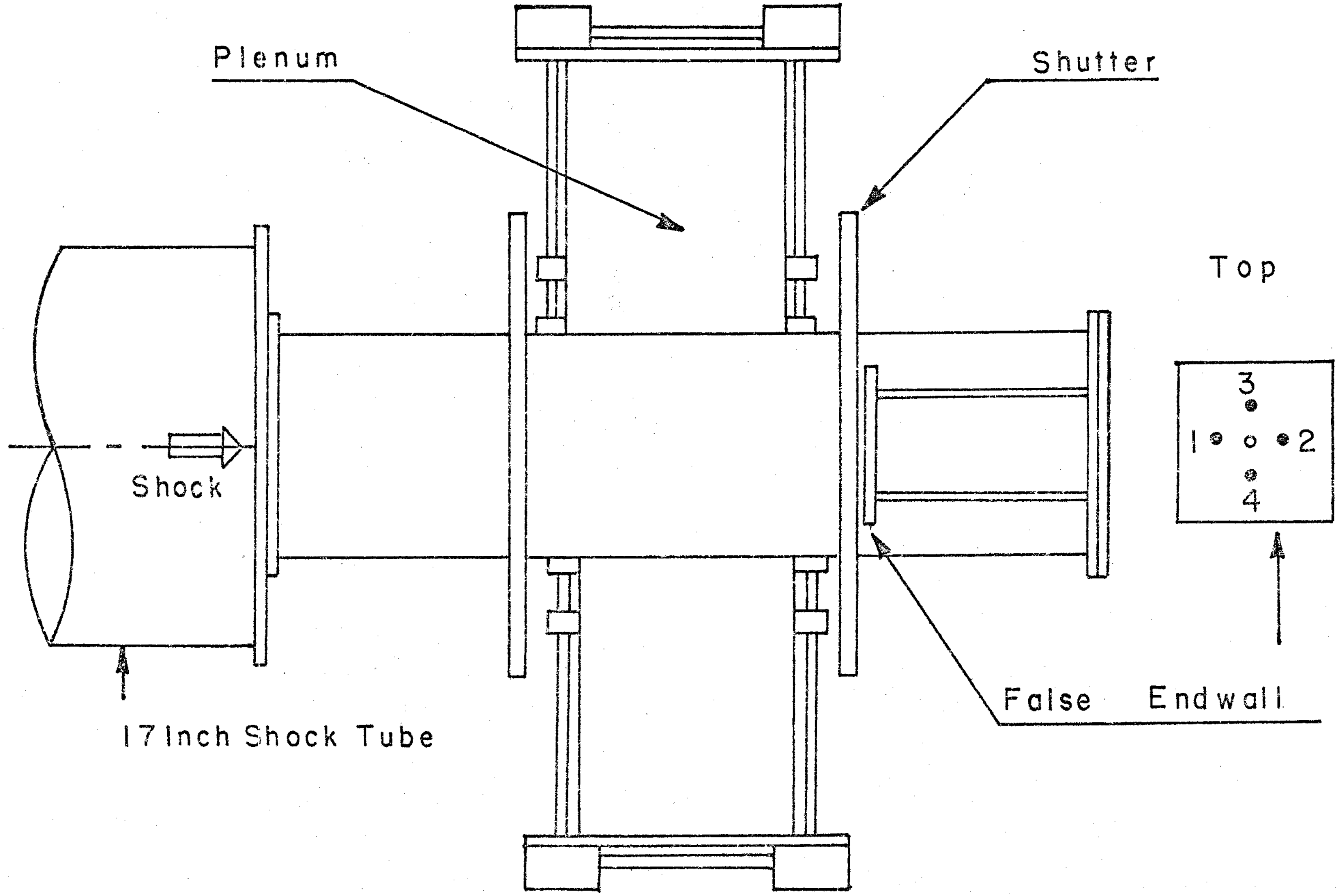

FIG. 3.3 FALSE ENDWALL FOR PRESSURE TRANSDUCERS

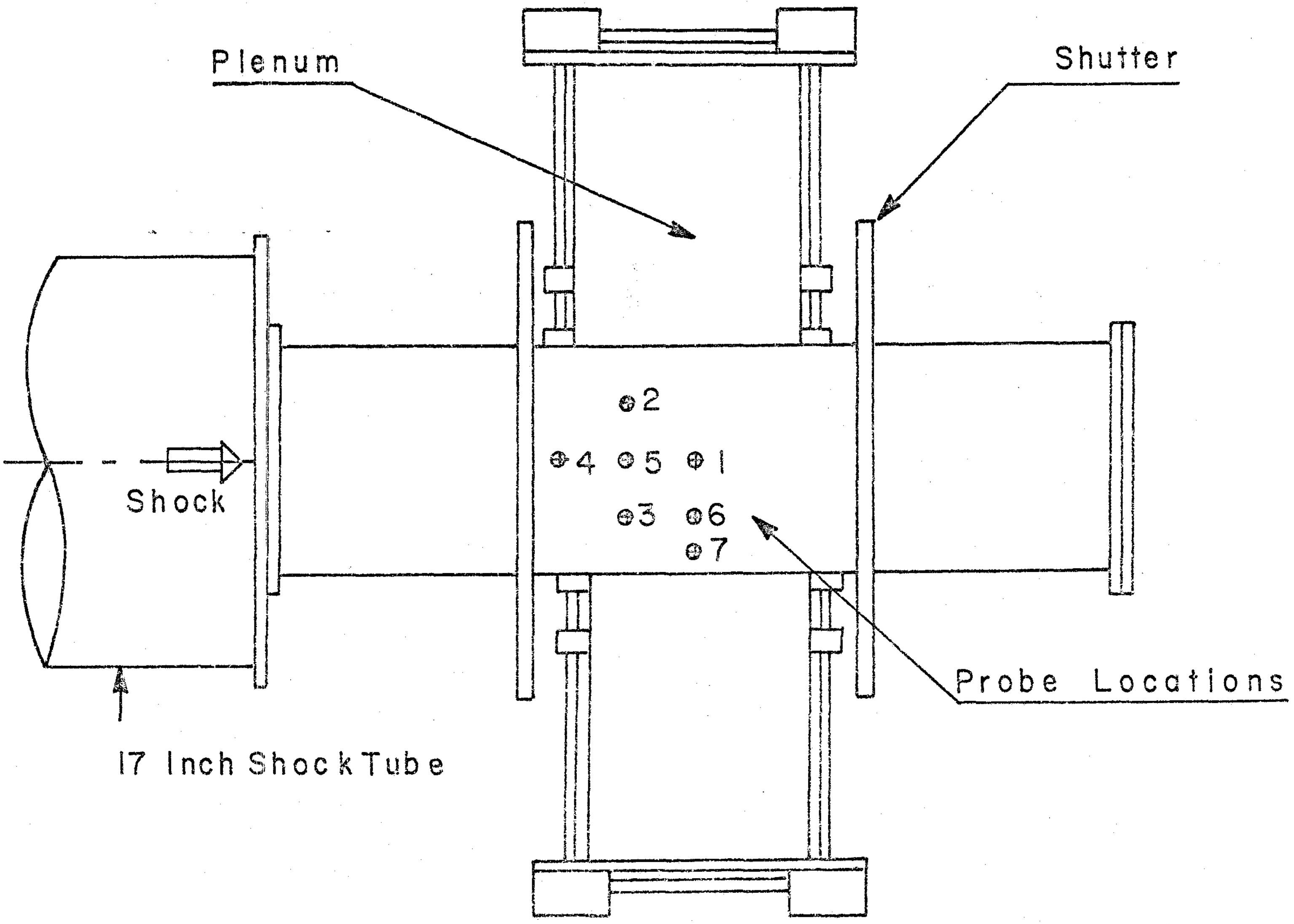

FIG. 5.1 DENSITY PROBE LOCATIONS

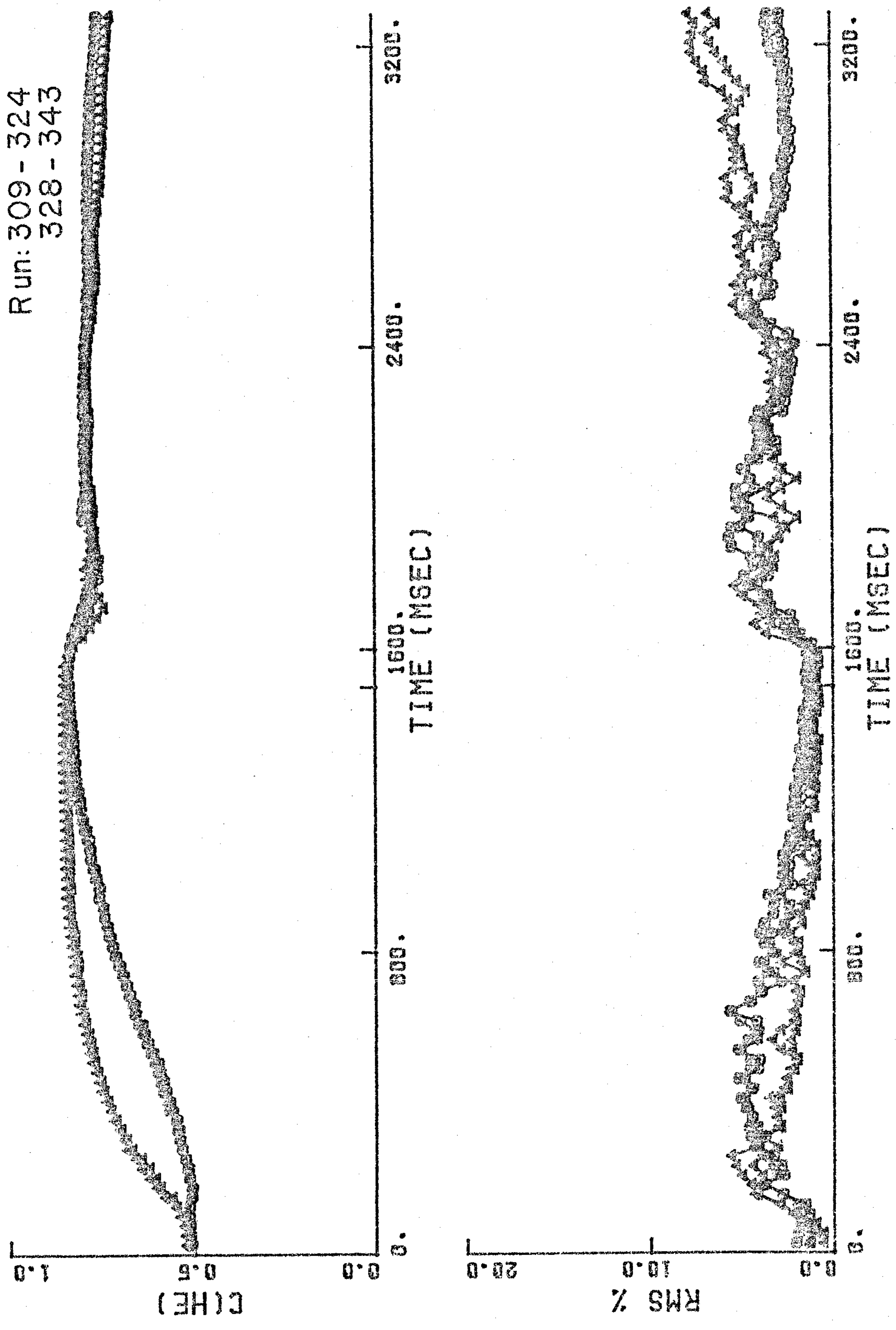

FIG.5.2 MEAN AND RMS DENSITY PROFILE

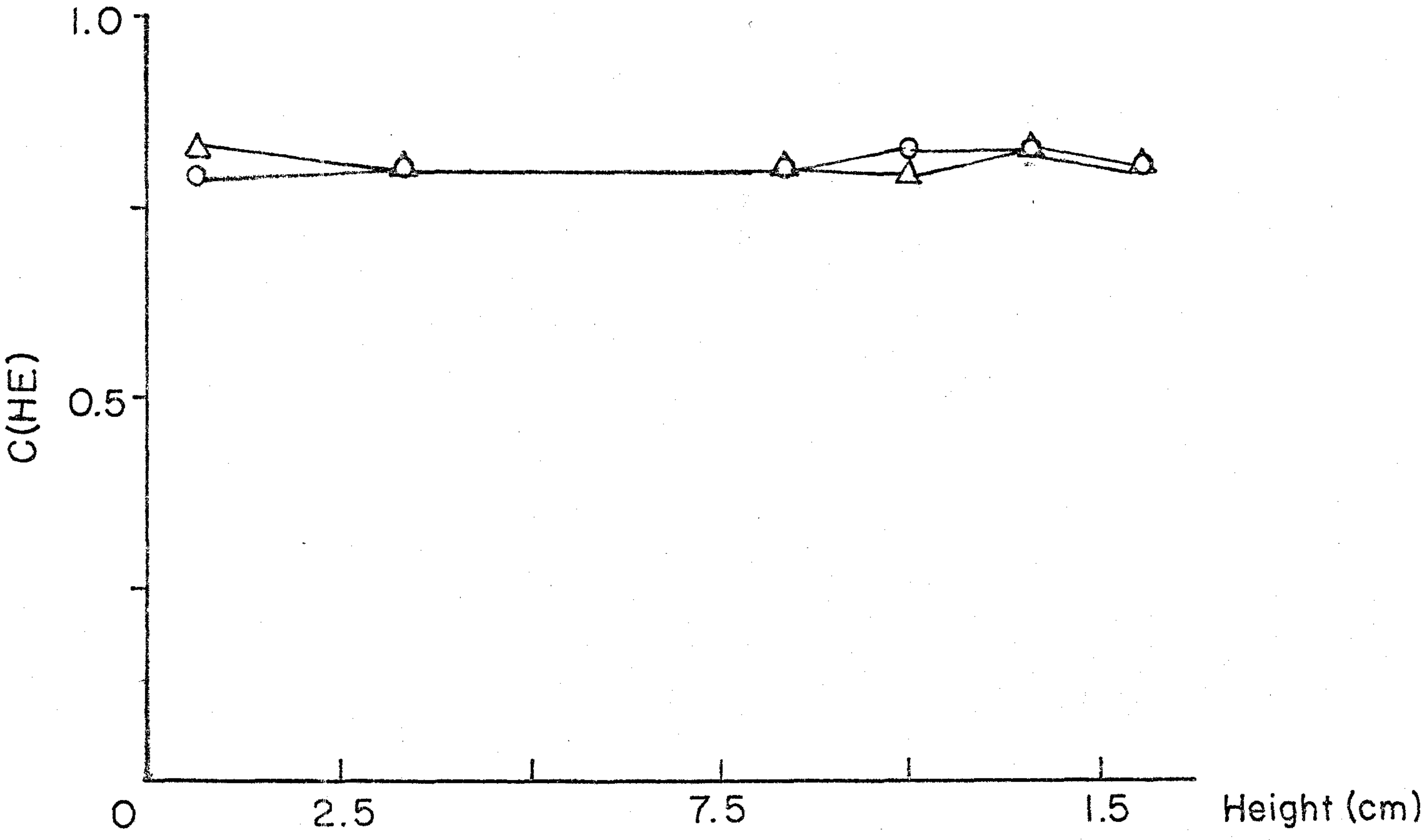

FIG.5.3MEAN CONCENTRATION AS A FUNCTION OF THE HEIGHT ABOVE THE BOTTOM

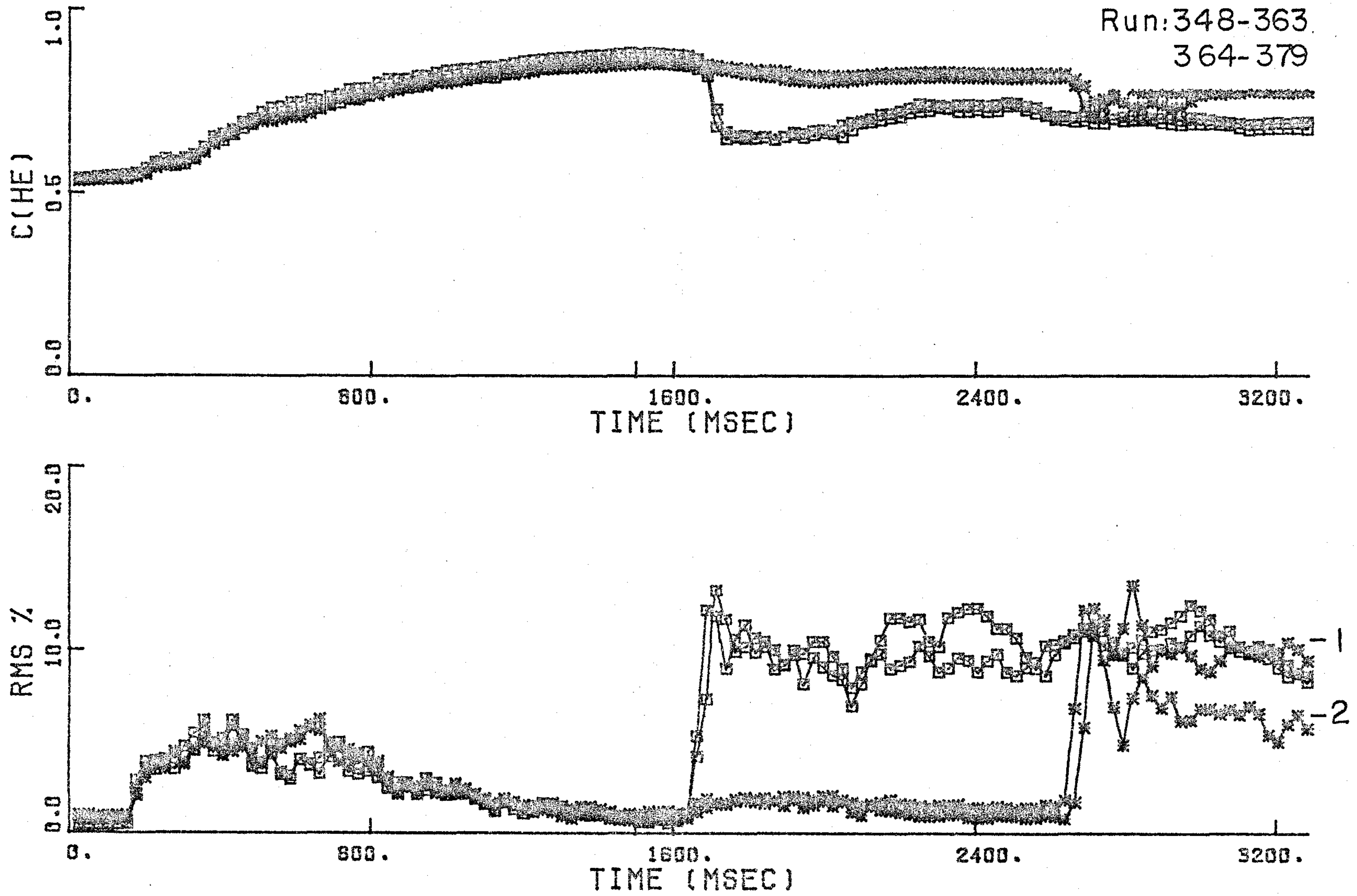

FIG. 5.4 MEAN AND RMS DENSITY PROFILE SHOWING SHUTTER EFFECT

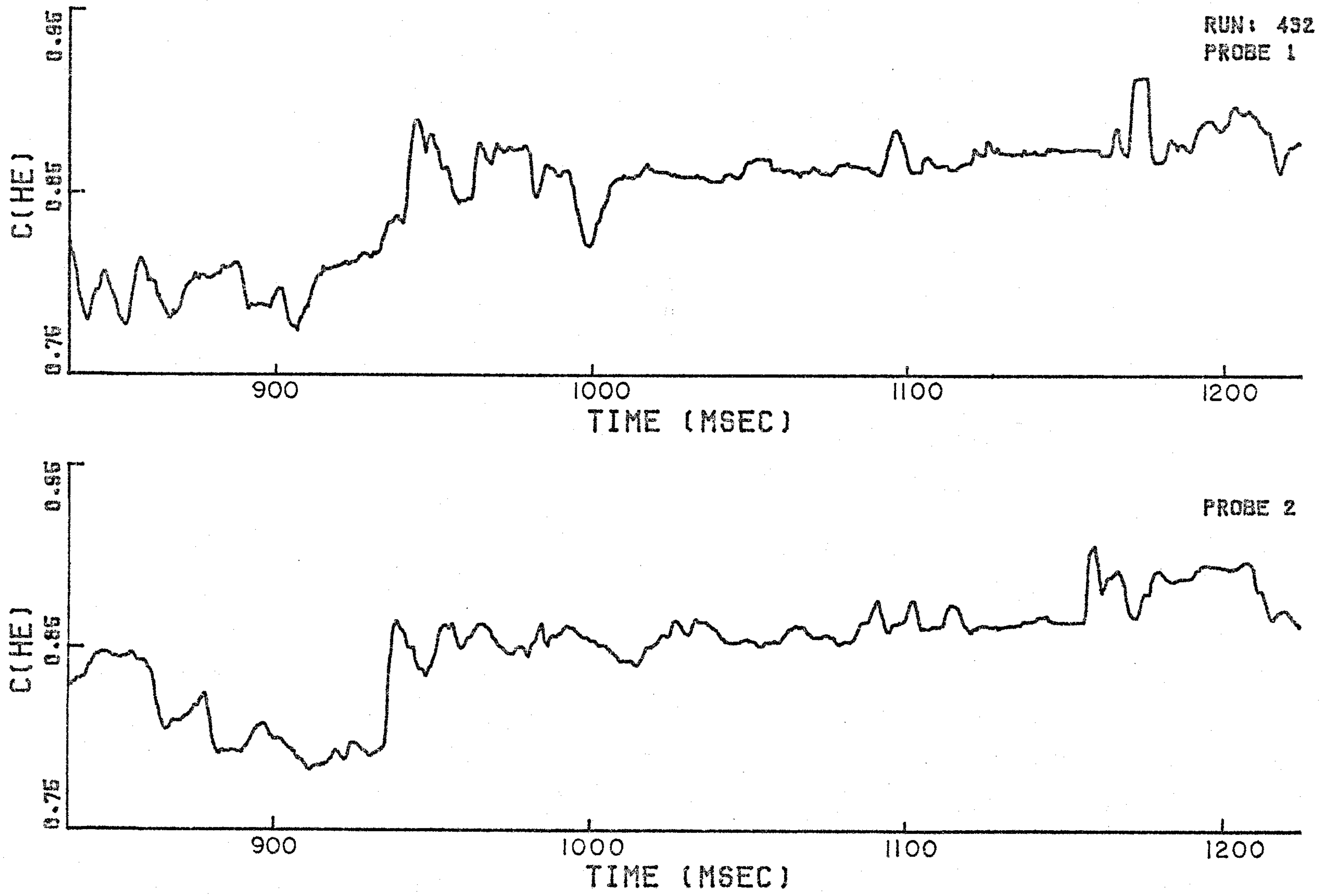

FIG. 5.5 RAW DENSITY DATA (JETS ON)

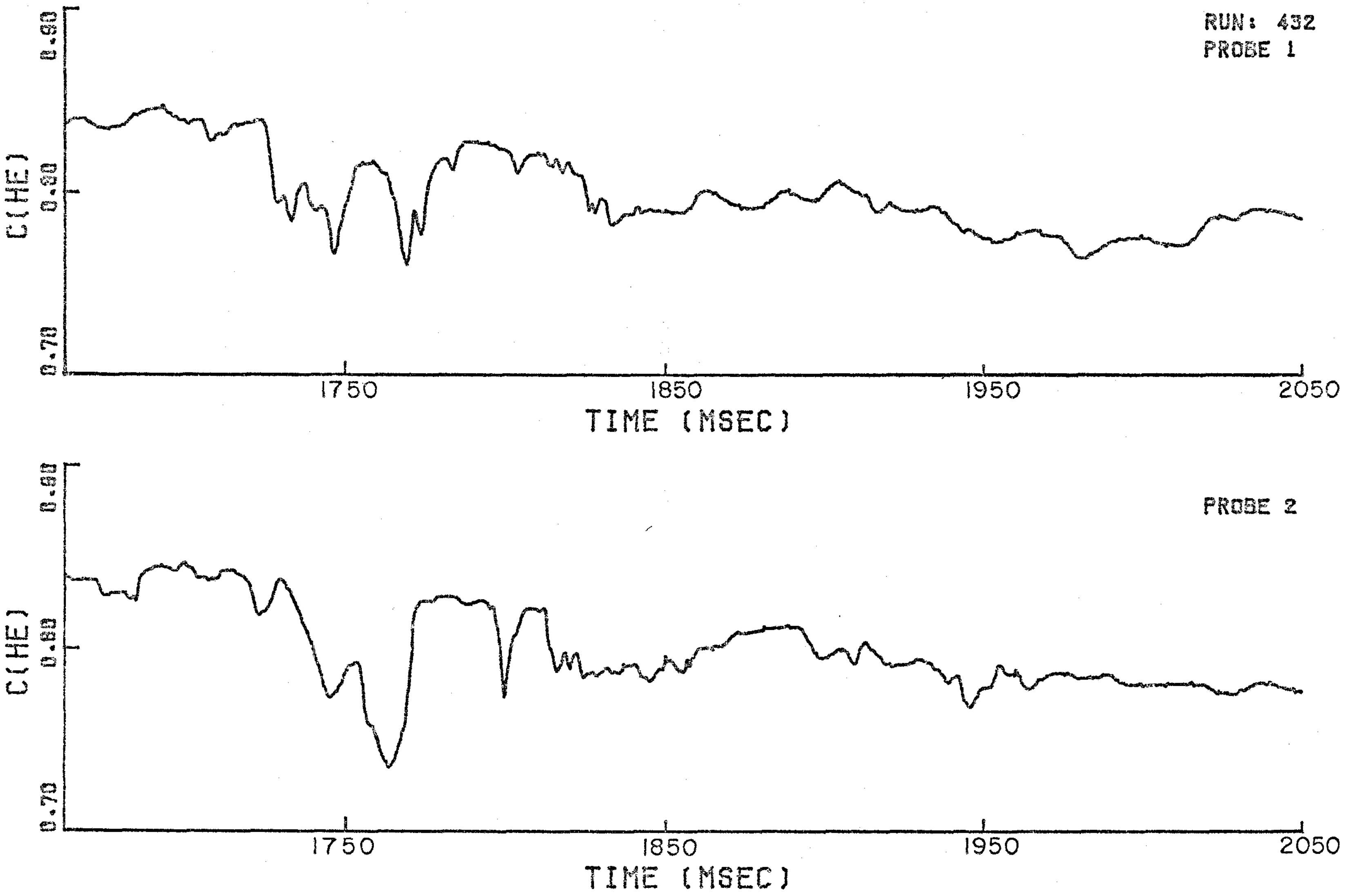

FIG.5.6 RAW DENSITY DATA (JETS OFF)

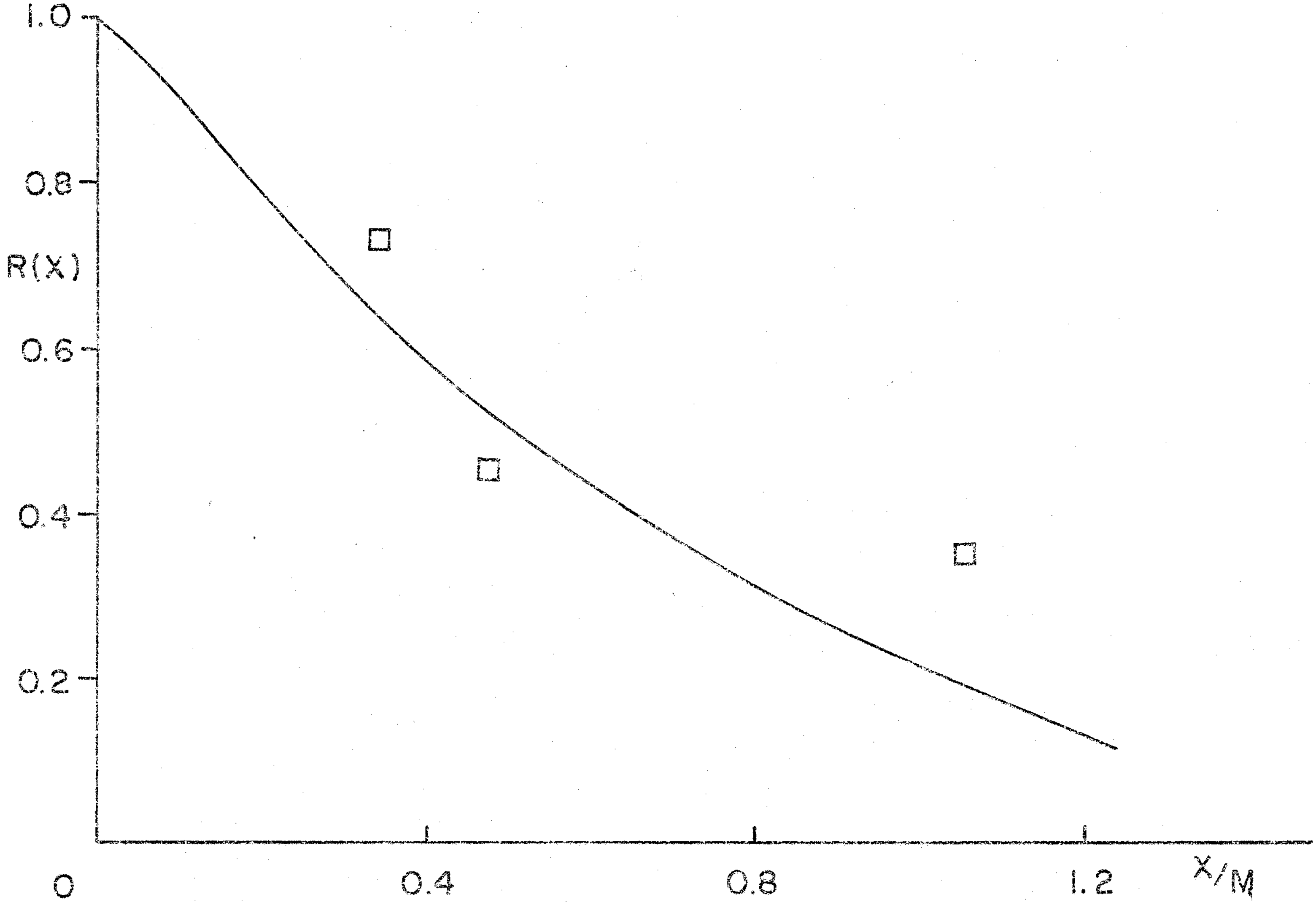

FIG.5.7 SPACE-CORRELATION FUNCTION (M=3.2 CM)

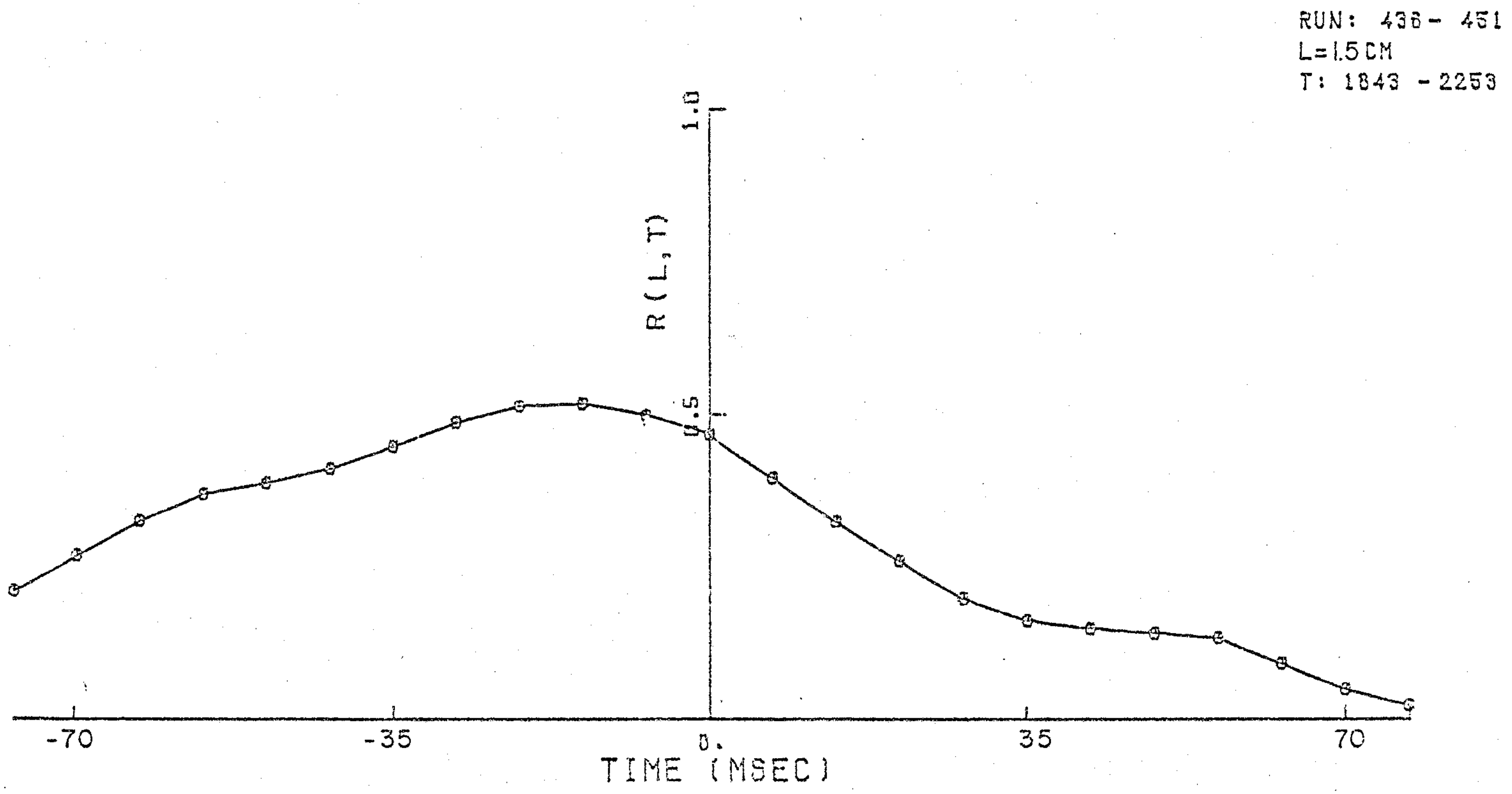

FIG.5.8 CROSS-CORRELATION FUNCTION

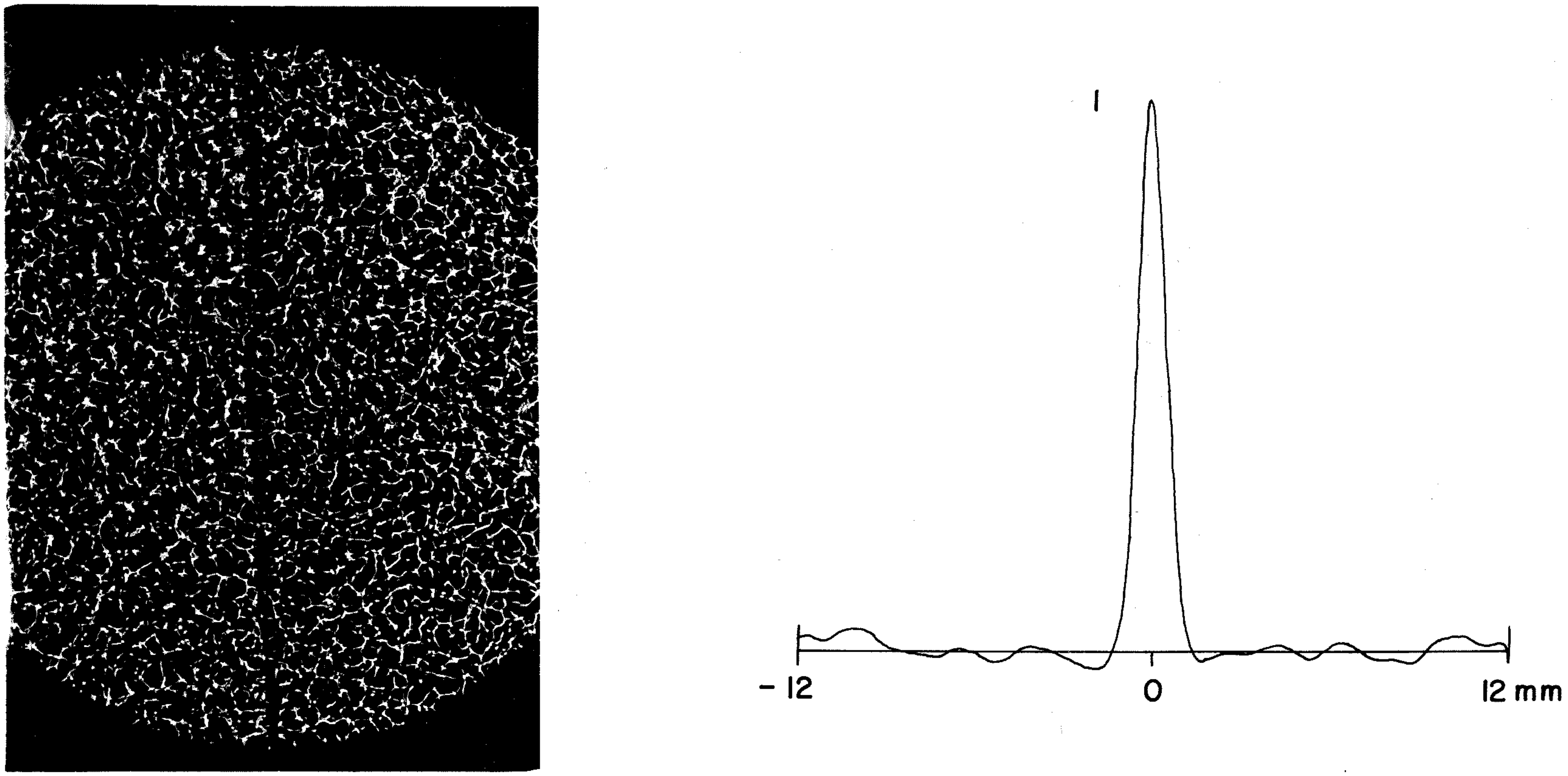

FIG.5.9 EXAMPLE OF SHADOWGRAPH CORRELATION FUNCTION ($M_s = 1.03$)

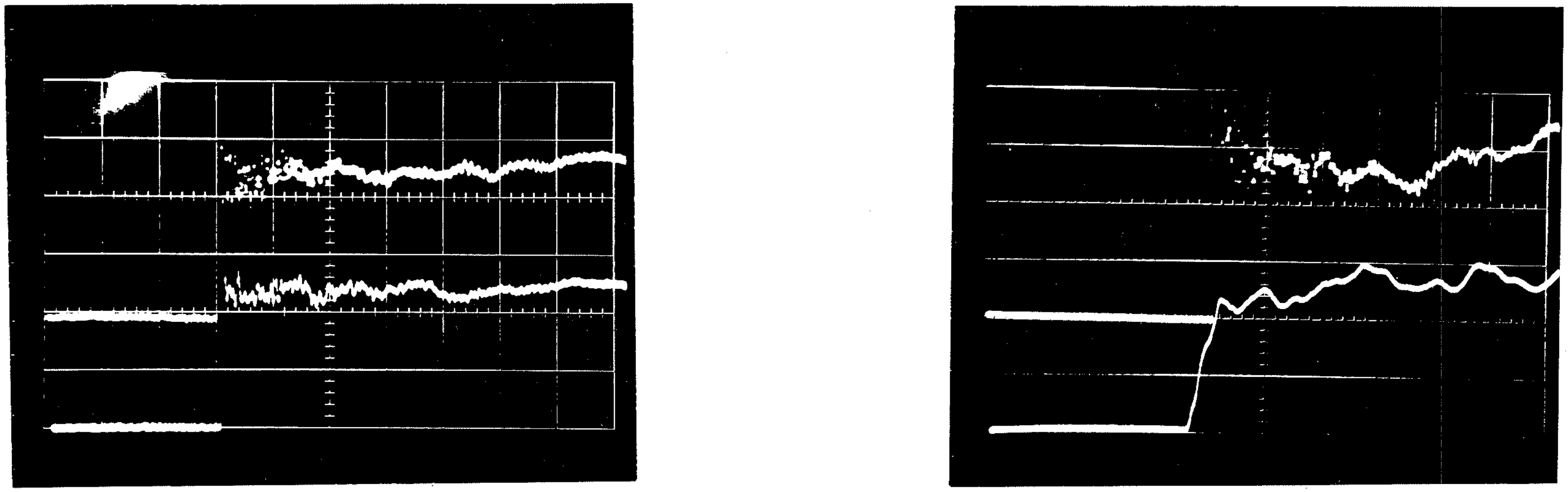

Decay Time = 2.4 sec., 1.5 psig/cm., 20 μ sec/cm.

No Scattering

Decay Time = 0.4 sec., 1.5 psig/cm., 20 μ sec/cm.

Scattering

FIG. 6.1 THE EFFECT OF THE DECAY TIME OF THE DENSITY FLUCTUATIONS ON THE SHOCK WAVE

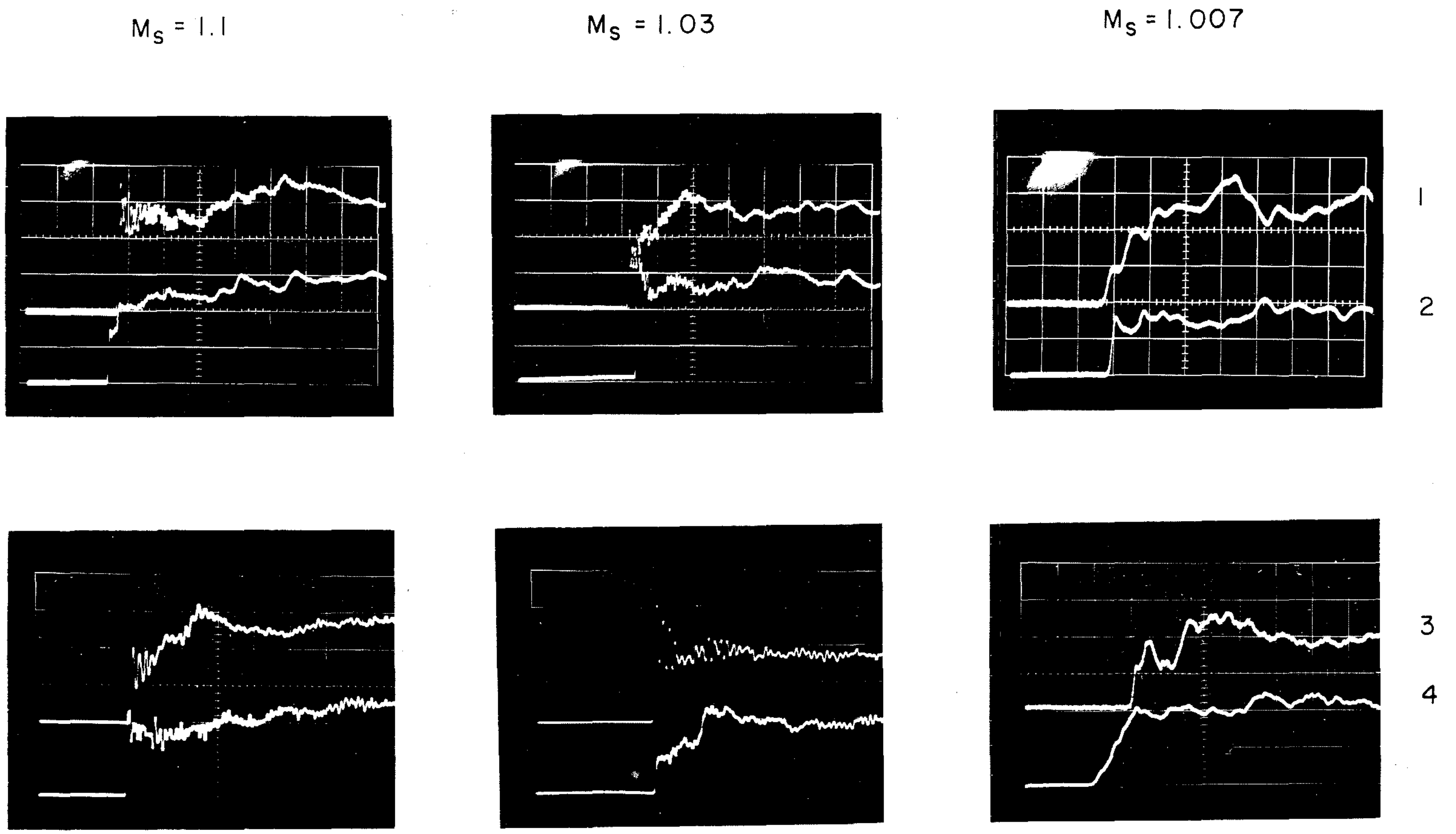

FIG. 6.2 REPRESENTATIVE PRESSURE TRACES MEASURED IN FALSE END WALL (HORIZ. 20 μsec./cm.)

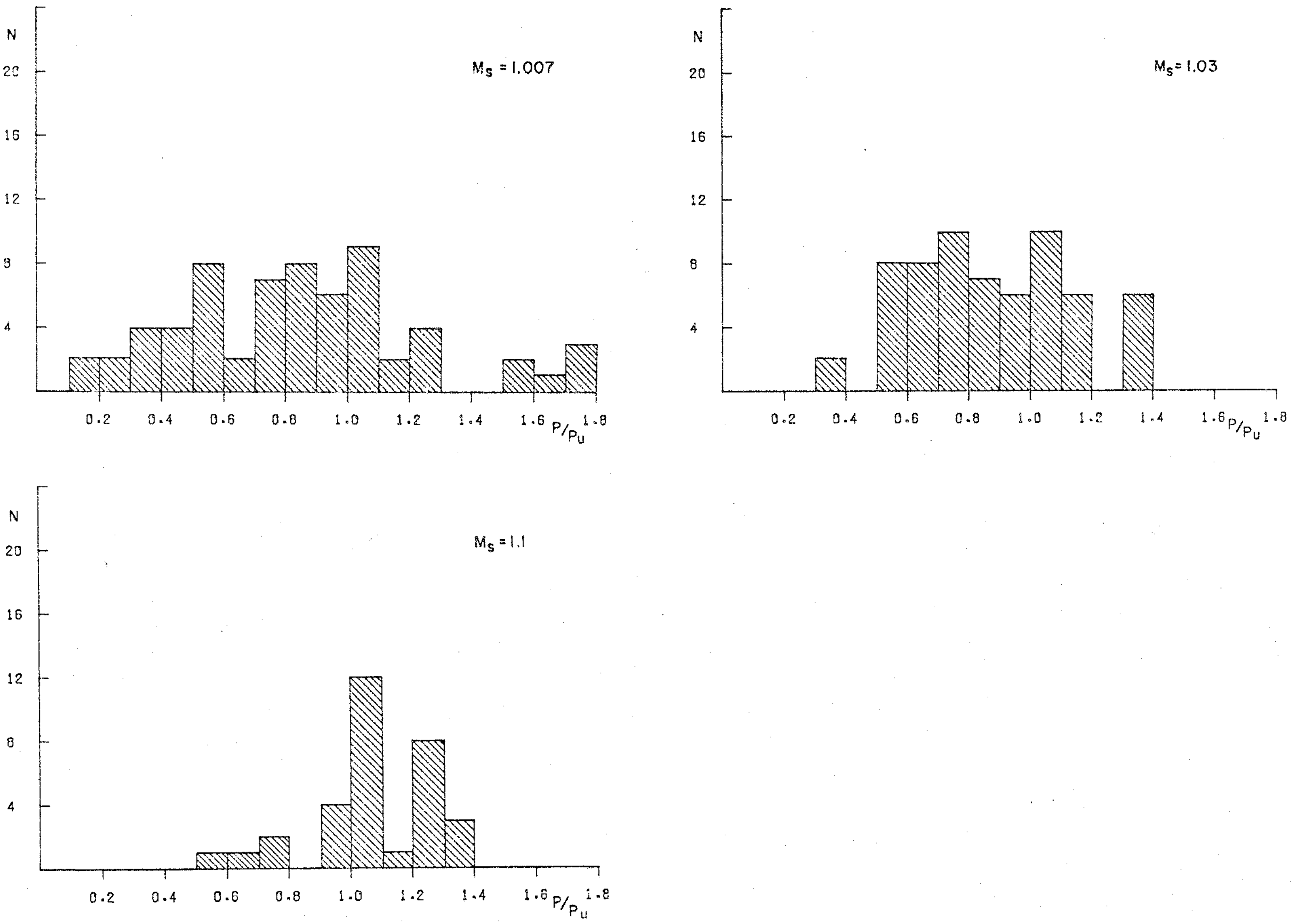

FIG. 6.3 HISTOGRAMS OF NORMALIZED SHOCK PRESSURES AS A FUNCTION OF MACH NUMBER. (MEASURED NEAR DOWNSTREAM SHUTTER)

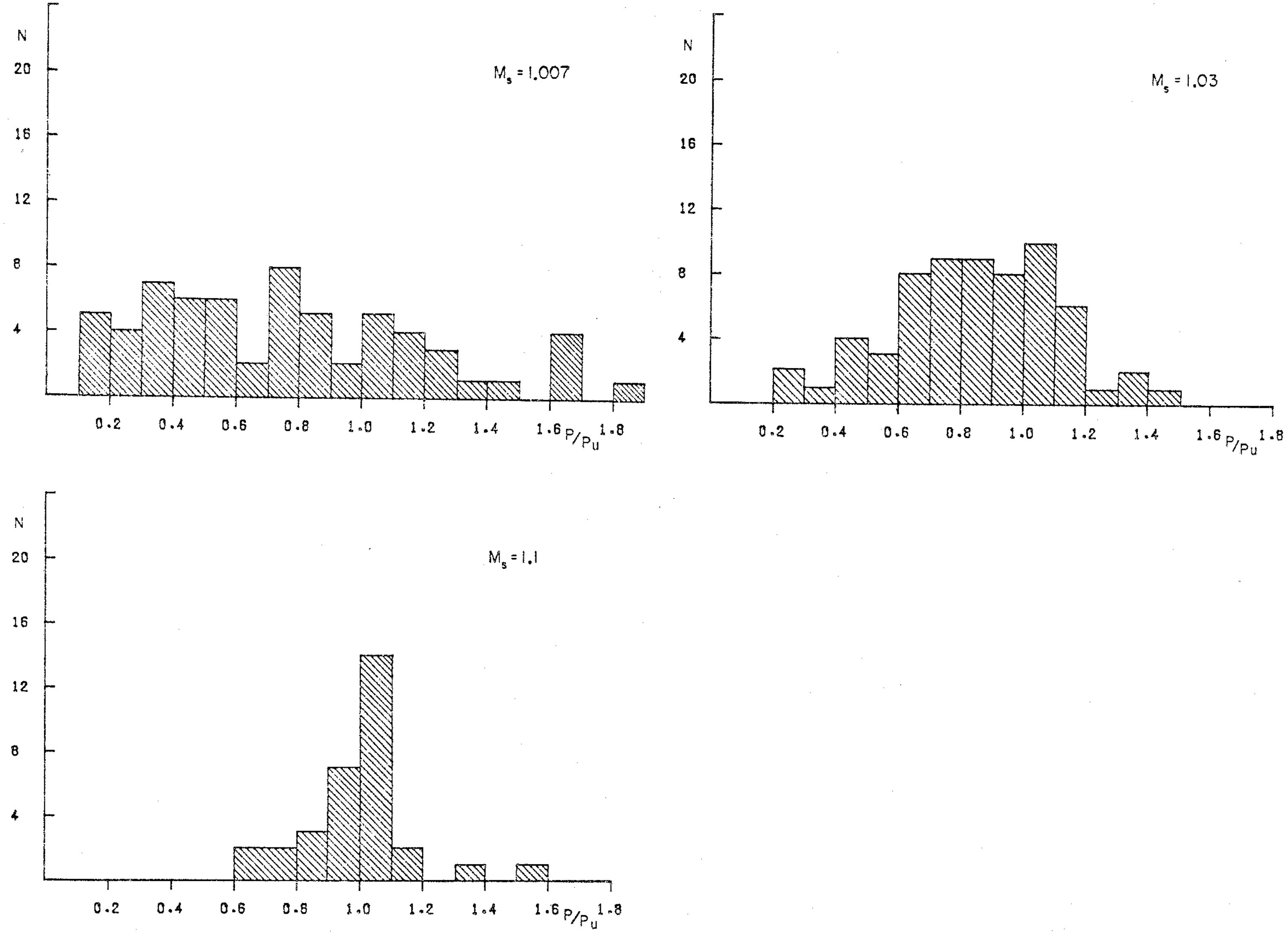

FIG.6.4 HISTOGRAMS OF NORMALIZED SHOCK PRESSURES AS A FUNCTION OF MACH NUMBER
(measured near endwall)

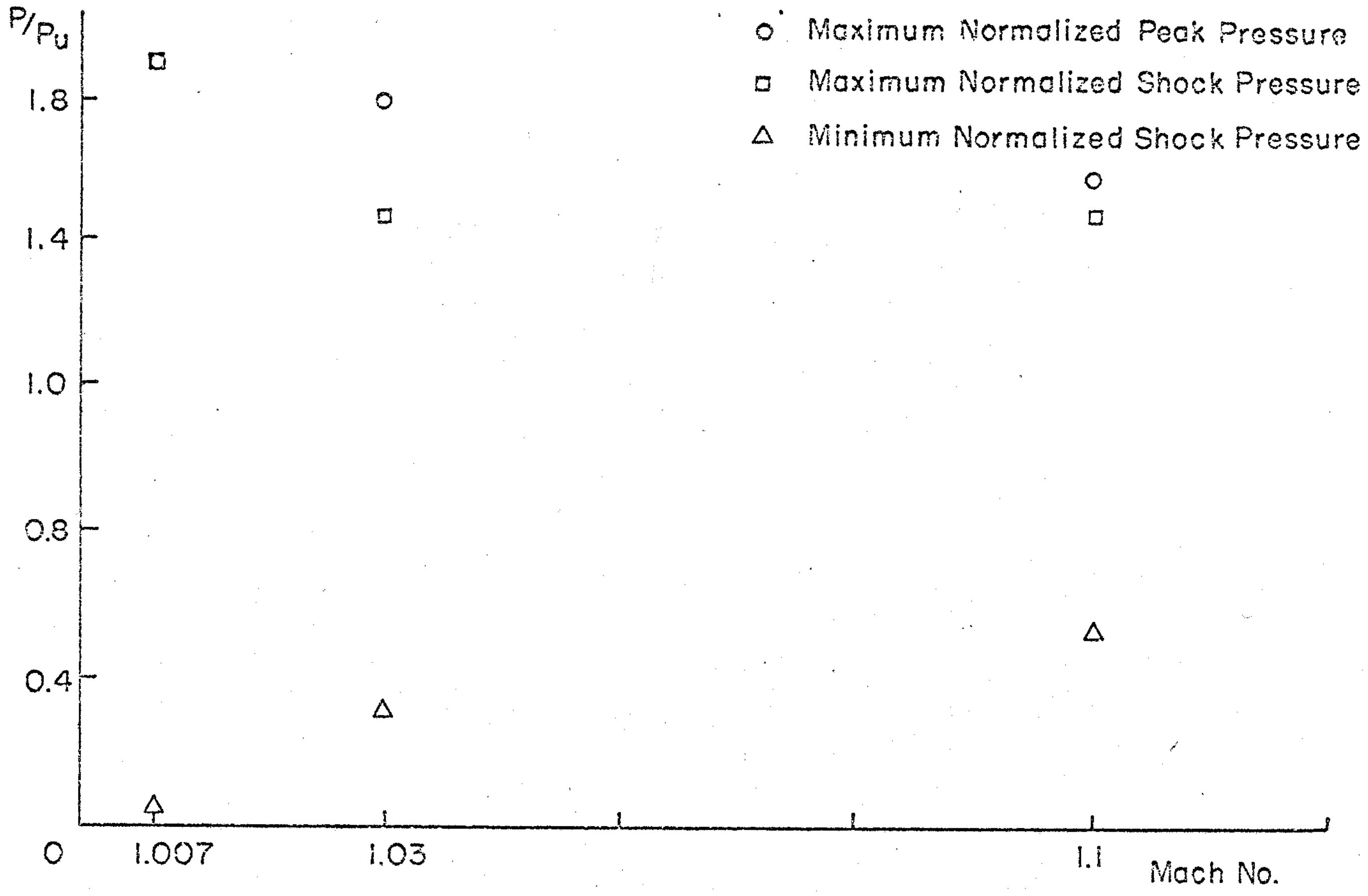

FIG.6.5EXTREME VALUES OF NORMALIZED PRESSURES AS A FUNCTION OF MACH NUMBER (measured near down stream shutter)

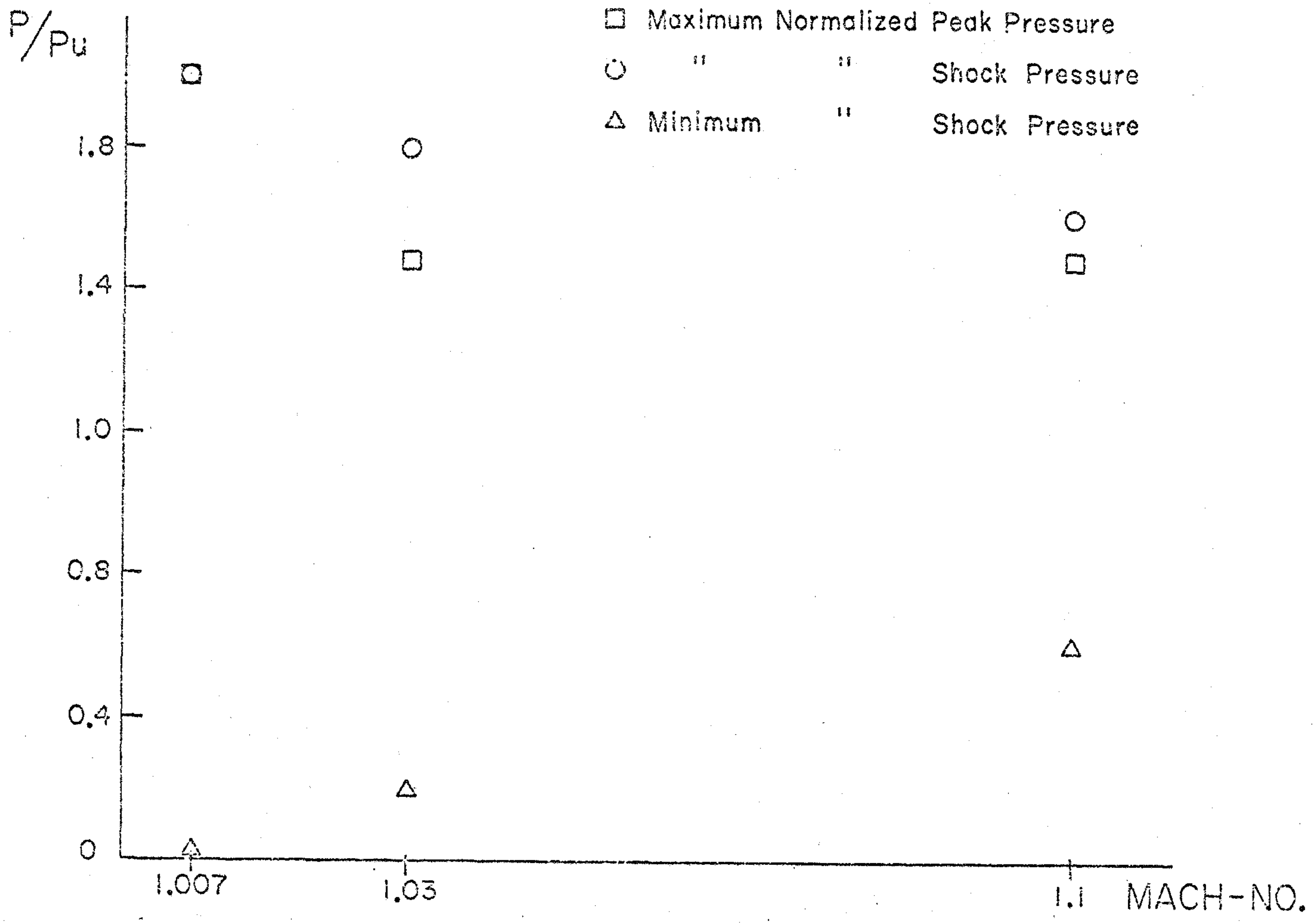

FIG. 6.6 EXTREME VALUES OF NORMALIZED PRESSURES AS A FUNCTION OF MACH NO. (measured near endwall)

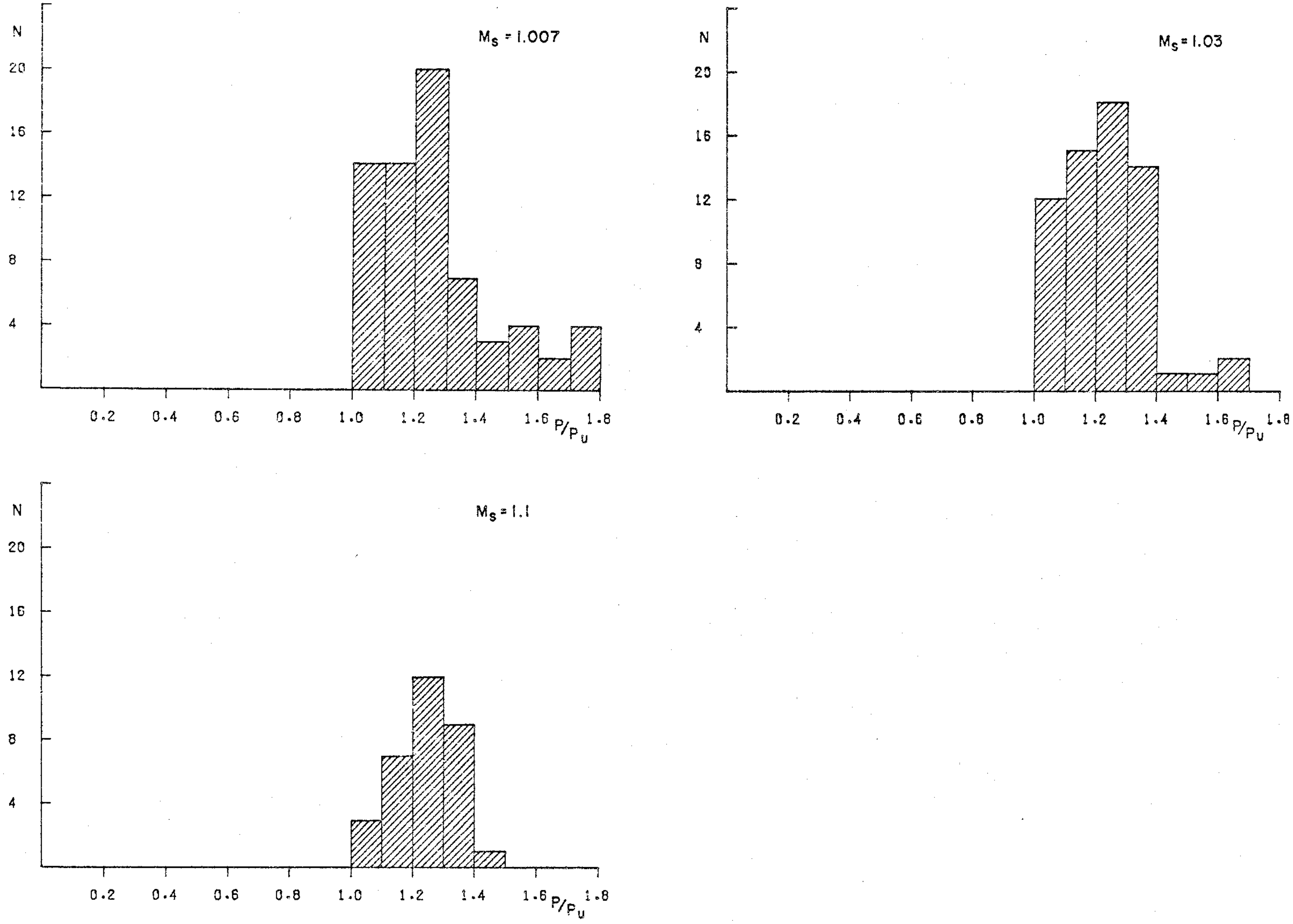

FIG. 6.7 HISTOGRAMS OF NORMALIZED PEAK PRESSURES AS A FUNCTION OF MACH NUMBER. (MEASURED NEAR DOWNSTREAM SHUTTER)

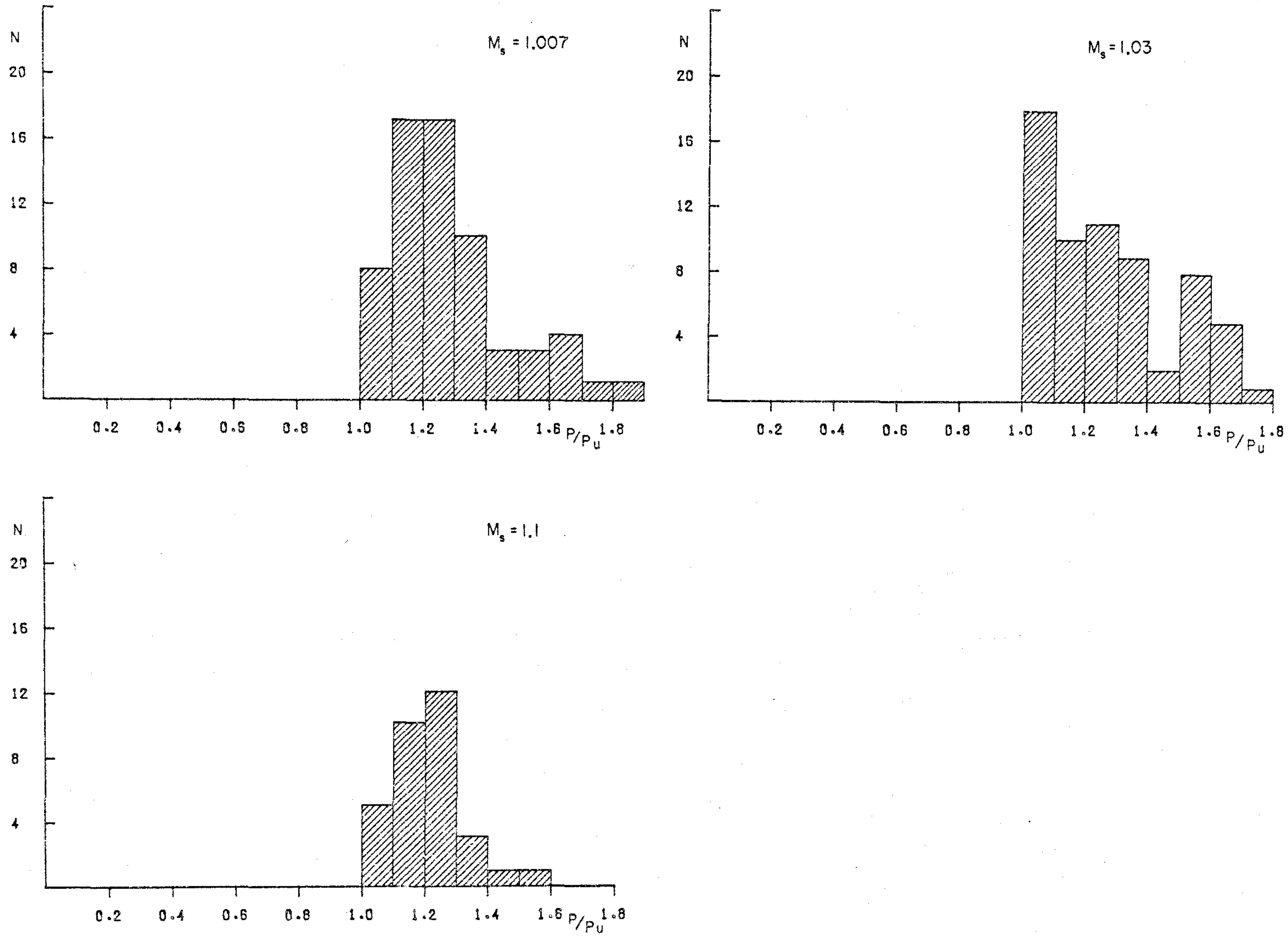

FIG. 6.8 HISTOGRAMS OF NORMALIZED PEAK PRESSURES AS A FUNCTION OF MACH NUMBER
(measured near endwall)

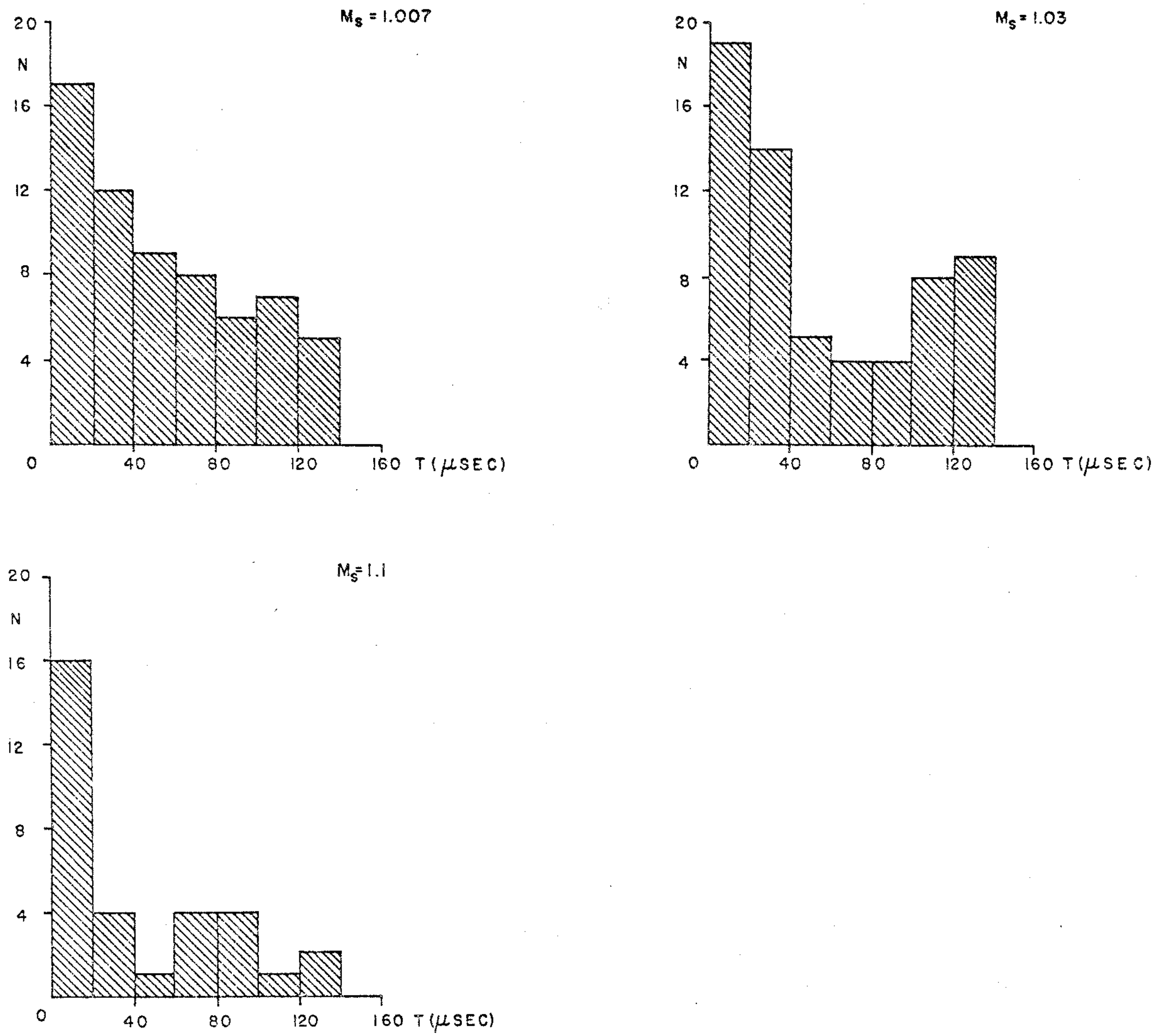

FIG.6.9 HISTOGRAMS FOR THE TIME LAG OF THE PEAK PRESSURE BEHIND THE FRONT. (MEASURED NEAR DOWNSTREAM SHUTTER)

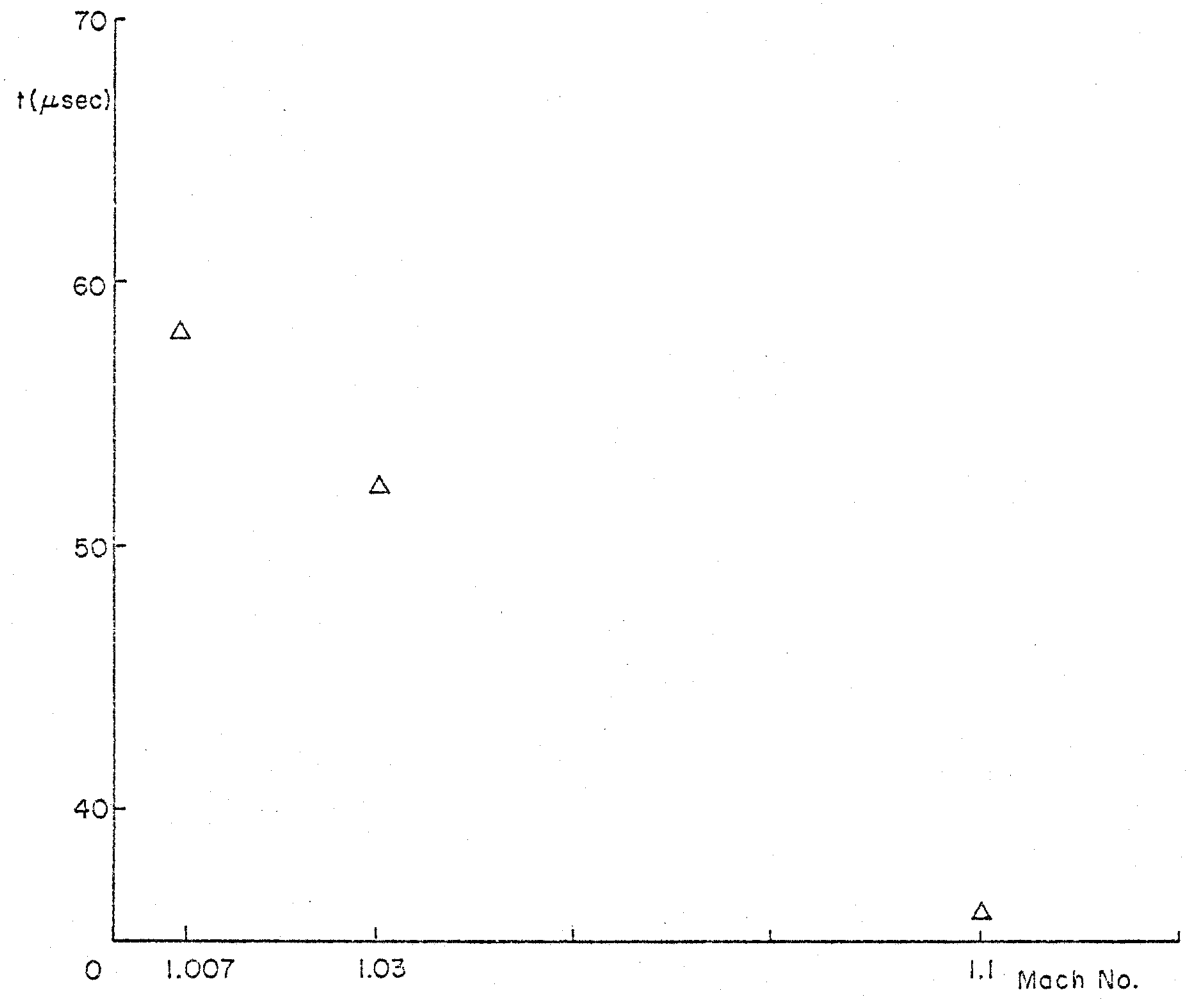

FIG.6.10 MEAN VALUES FOR THE TIME LAG BETWEEN PEAK AND SHOCK FRONT PRESSURES (measured near down stream shutter)

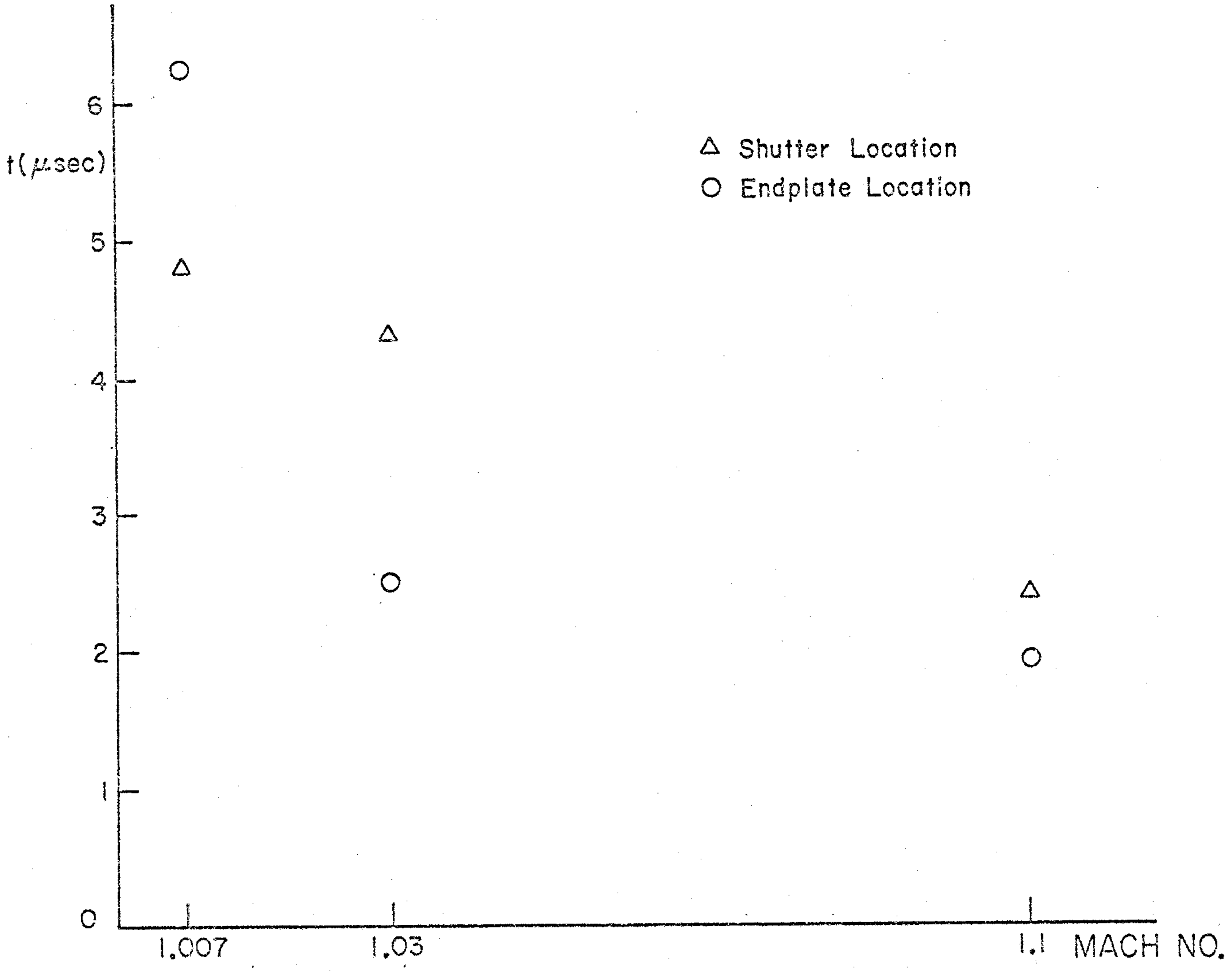

FIG. 6.11 RMS ARRIVAL TIME FLUCTUATIONS AS A FUNCTION OF MACH NUMBER

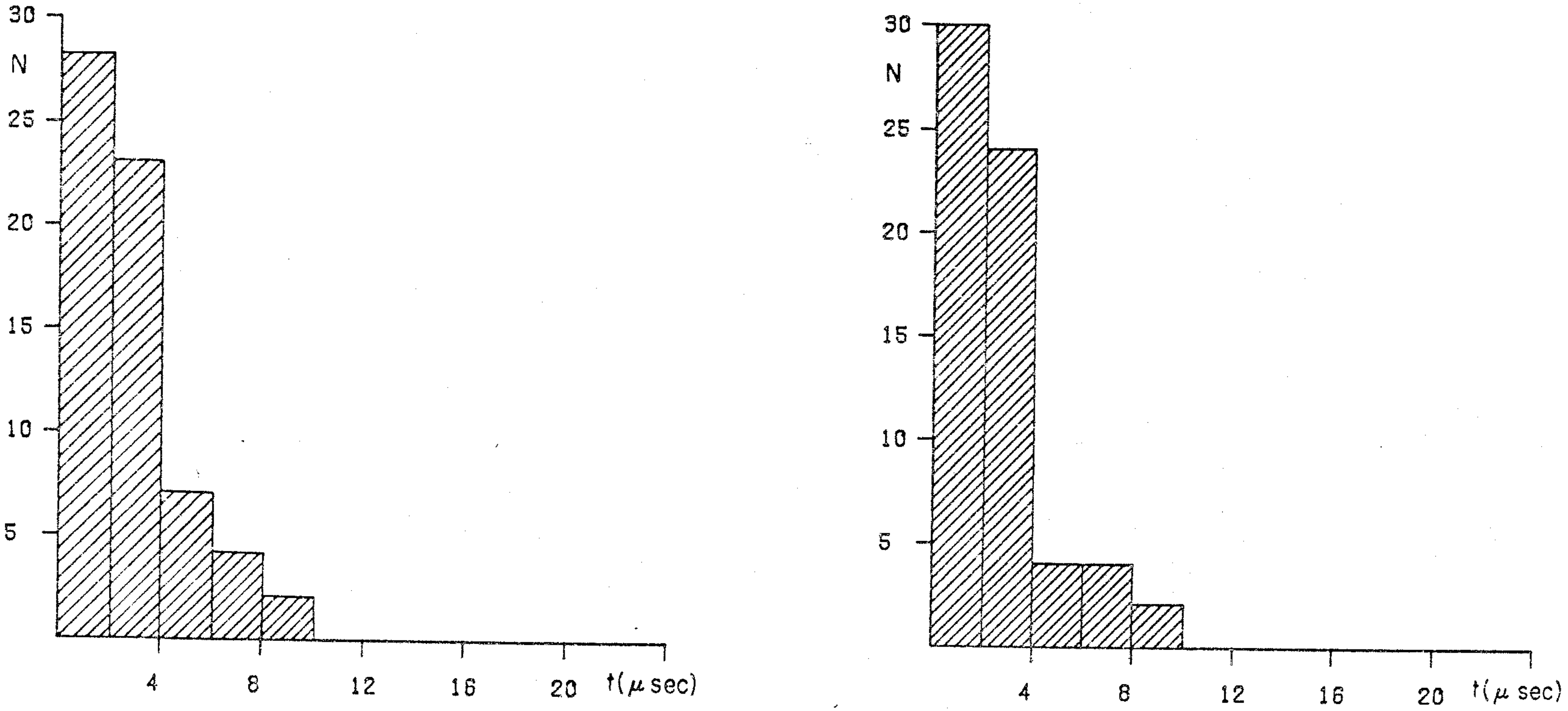

(measured near down stream shutter)

(measured near endwall)

FIG.6.12 HISTOGRAM OF SHOCK RISE TIMES ($M_S = 1.007$)

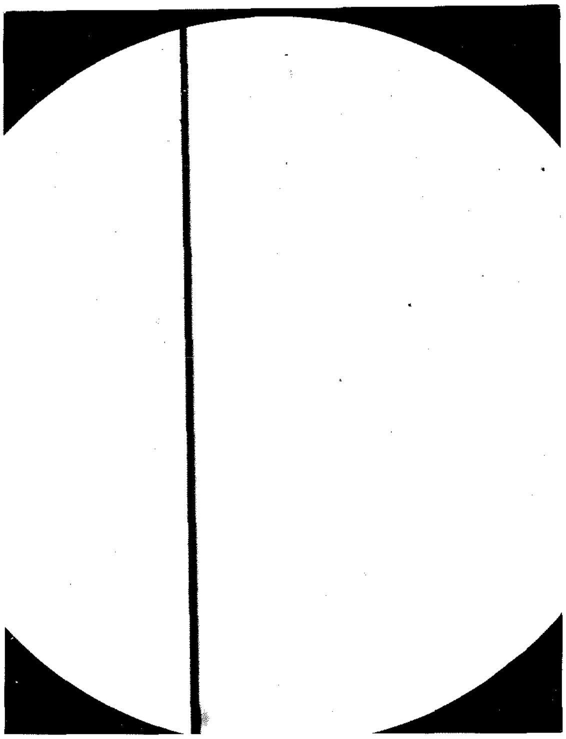

FIG. 6.14 SCHLIEREN PHOTOGRAPH OF M_S=1.03 UNPERTURBED SHOCK MOVING FROM RIGHT TO LEFT

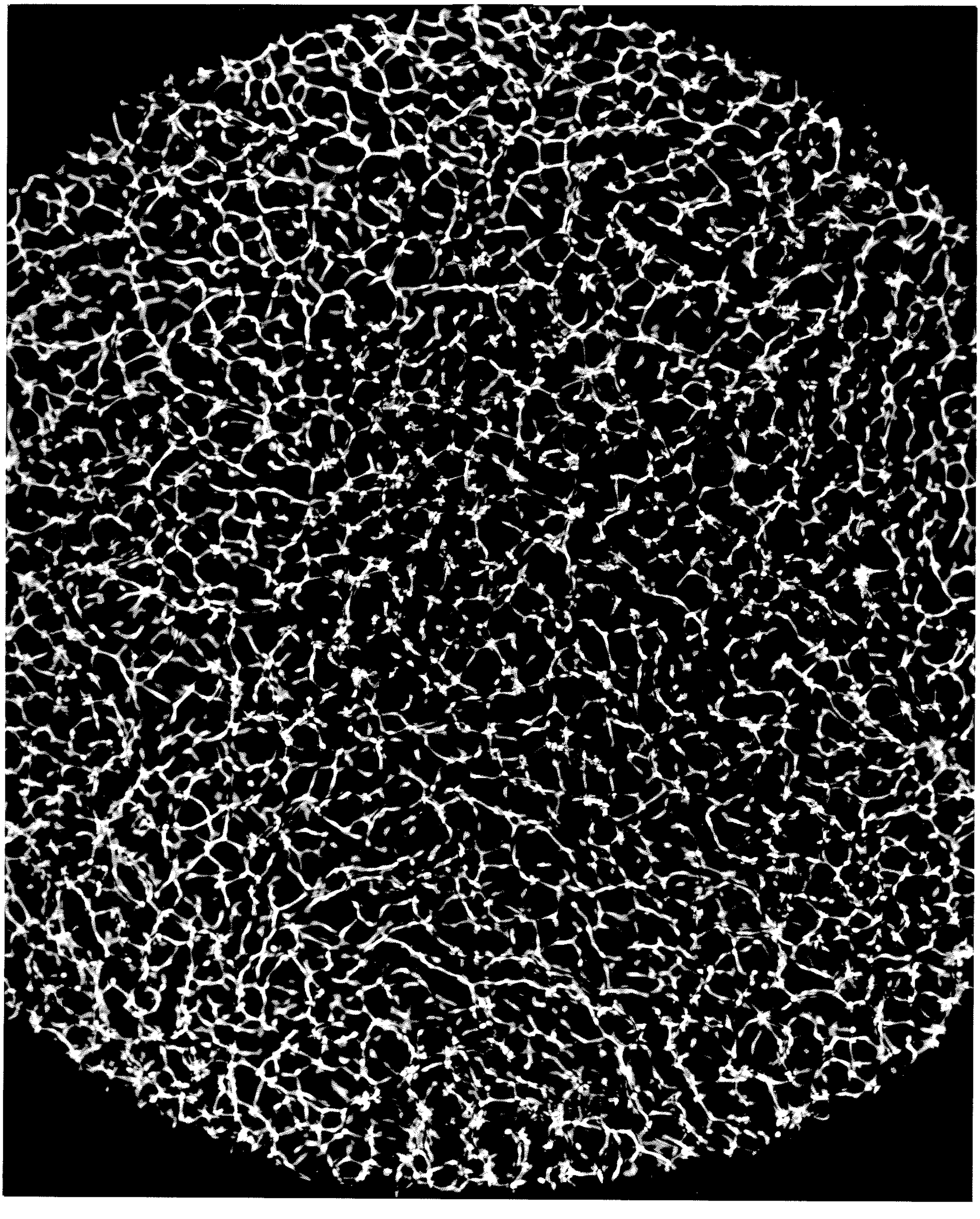

FIG. 6.15 SHADOWGRAPH PHOTOGRAPH OF M_S=1.007 SHOCK WHICH IS INDISTINGUISHABLE FROM THE TURBULENCE

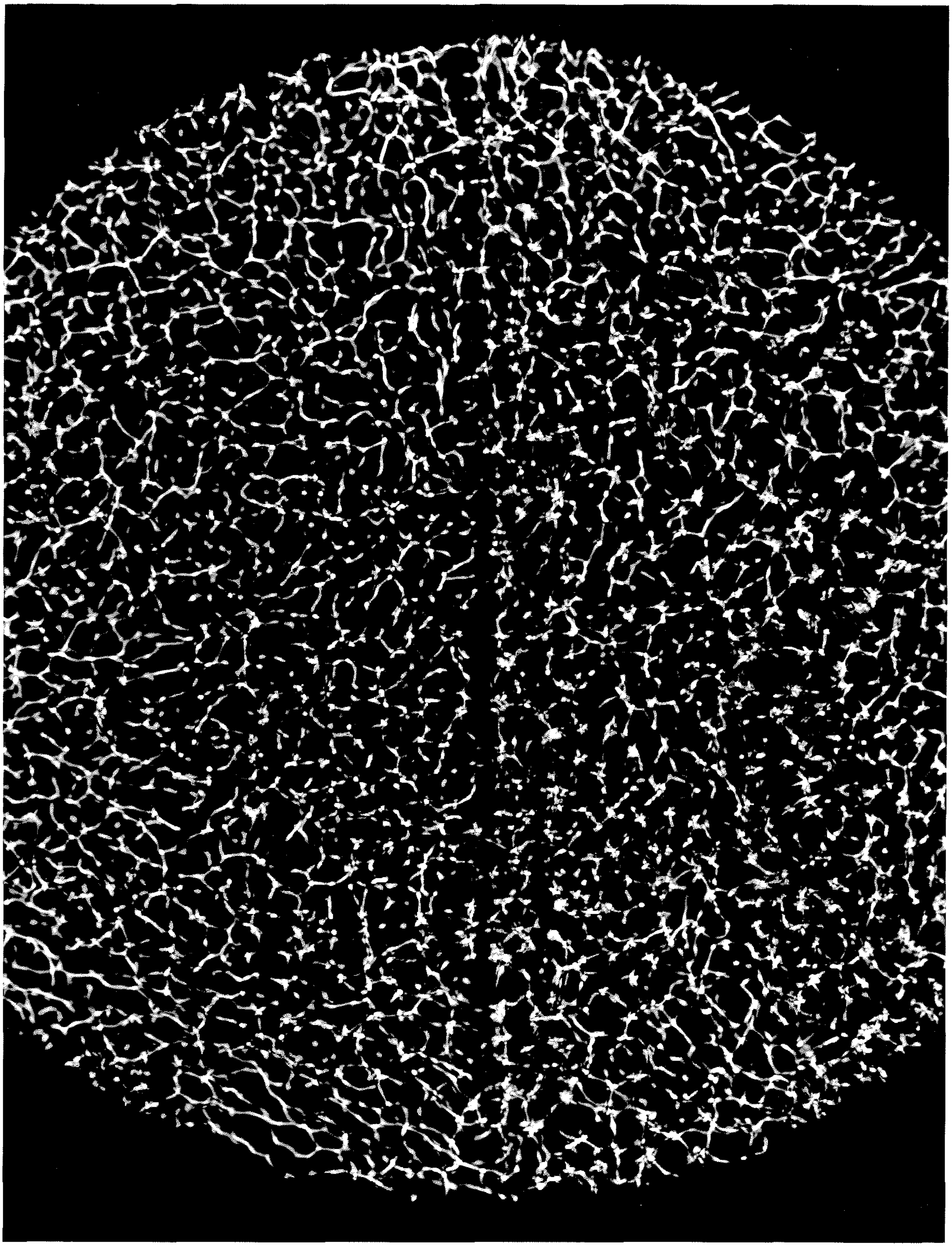

FIG. 6.16 SHADOWGRAPH PHOTOGRAPH OF $M_s = 1.03$ SHOCK MOVING FROM RIGHT TO LEFT

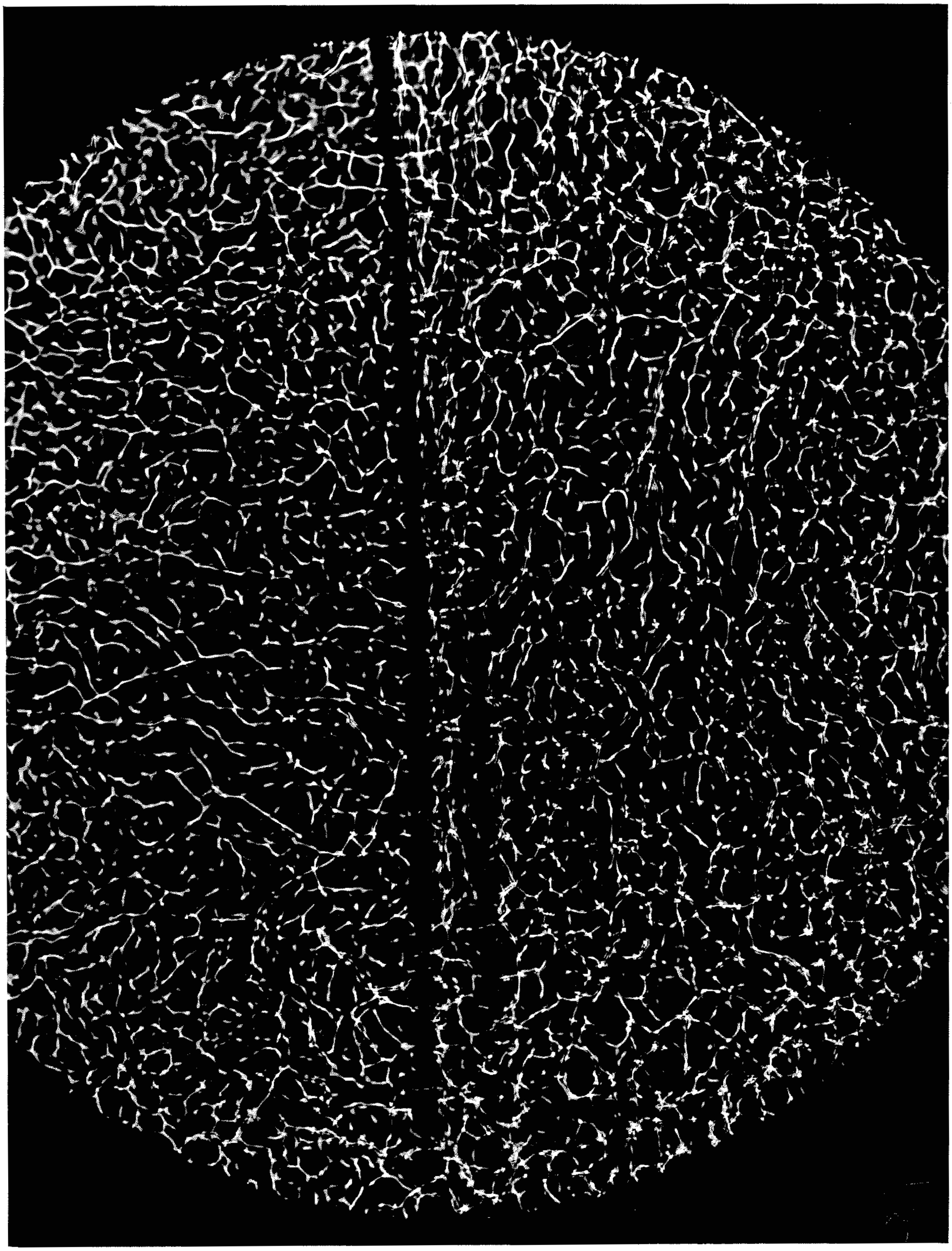

FIG. 6.17 SHADOWGRAPH PHOTOGRAPH OF $M_s = 1.1$ SHOCK MOVING FROM RIGHT TO LEFT

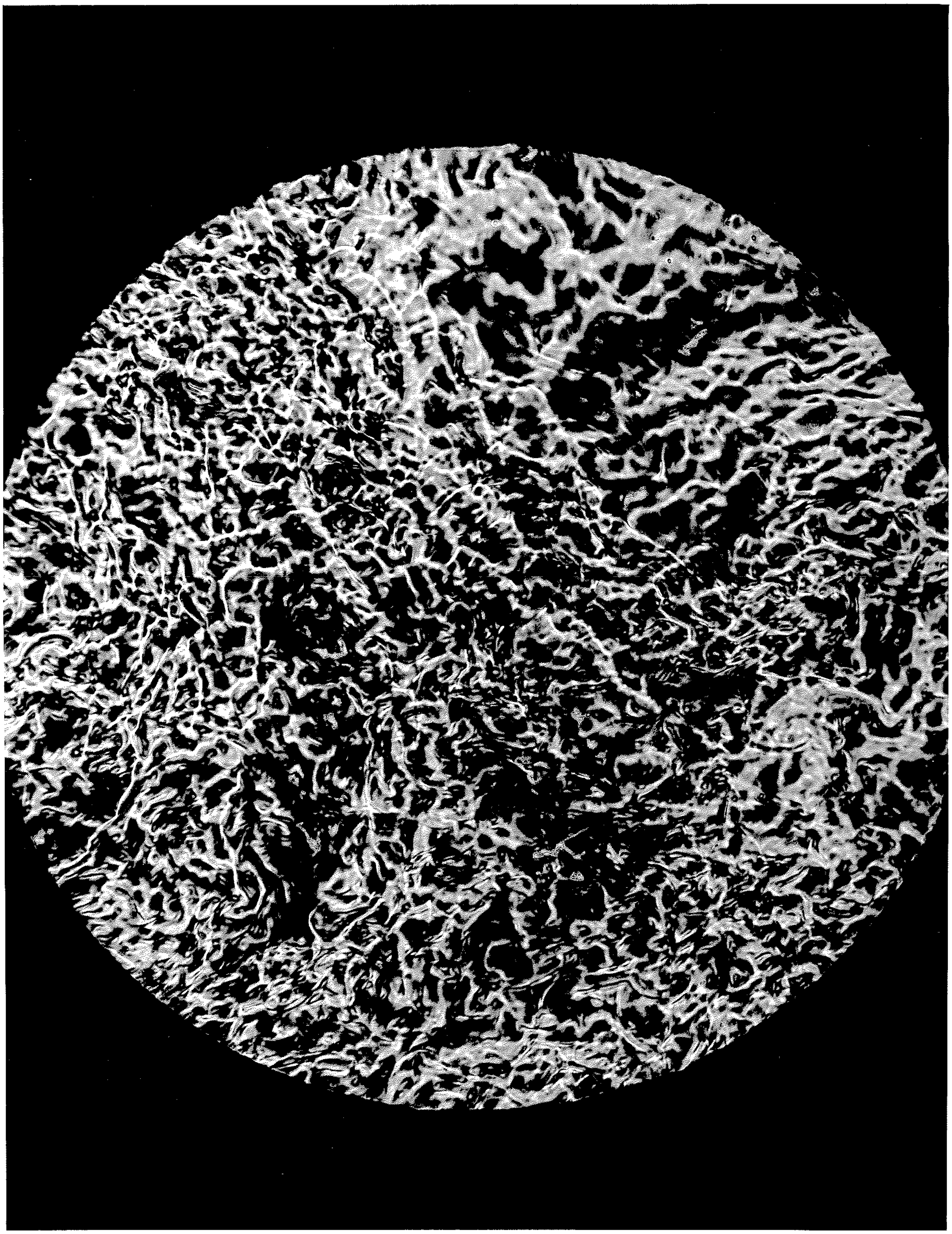

FIG. 6.18 SCHLIEREN PHOTOGRAPH OF M_S=1.007 SHOCK WHICH IS INDISTINGUISHABLE FROM THE TURBULENCE

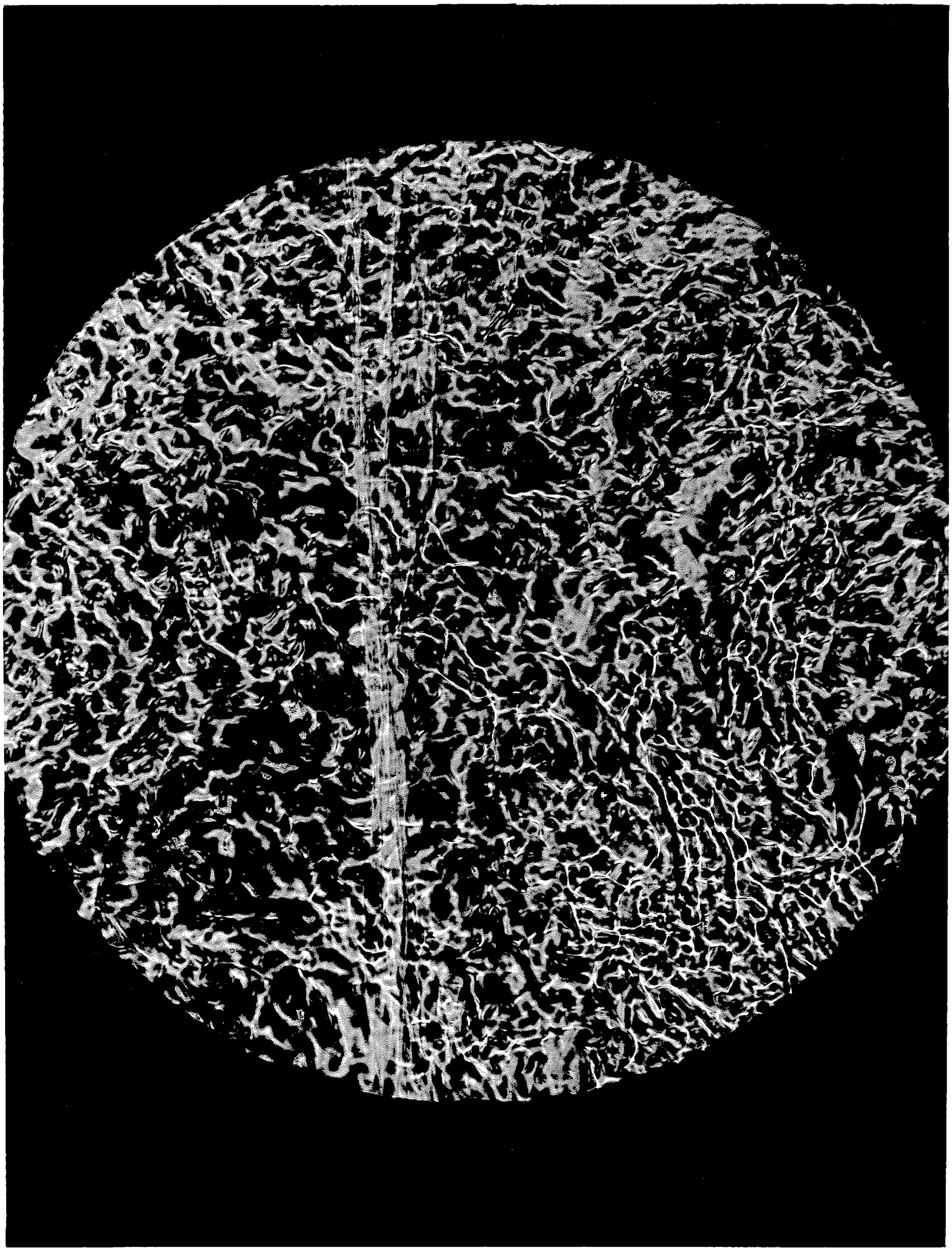

FIG. 6.19 SCHLIEREN PHOTOGRAPH OF $M_s = 1.03$ SHOCK MOVING FROM RIGHT TO LEFT

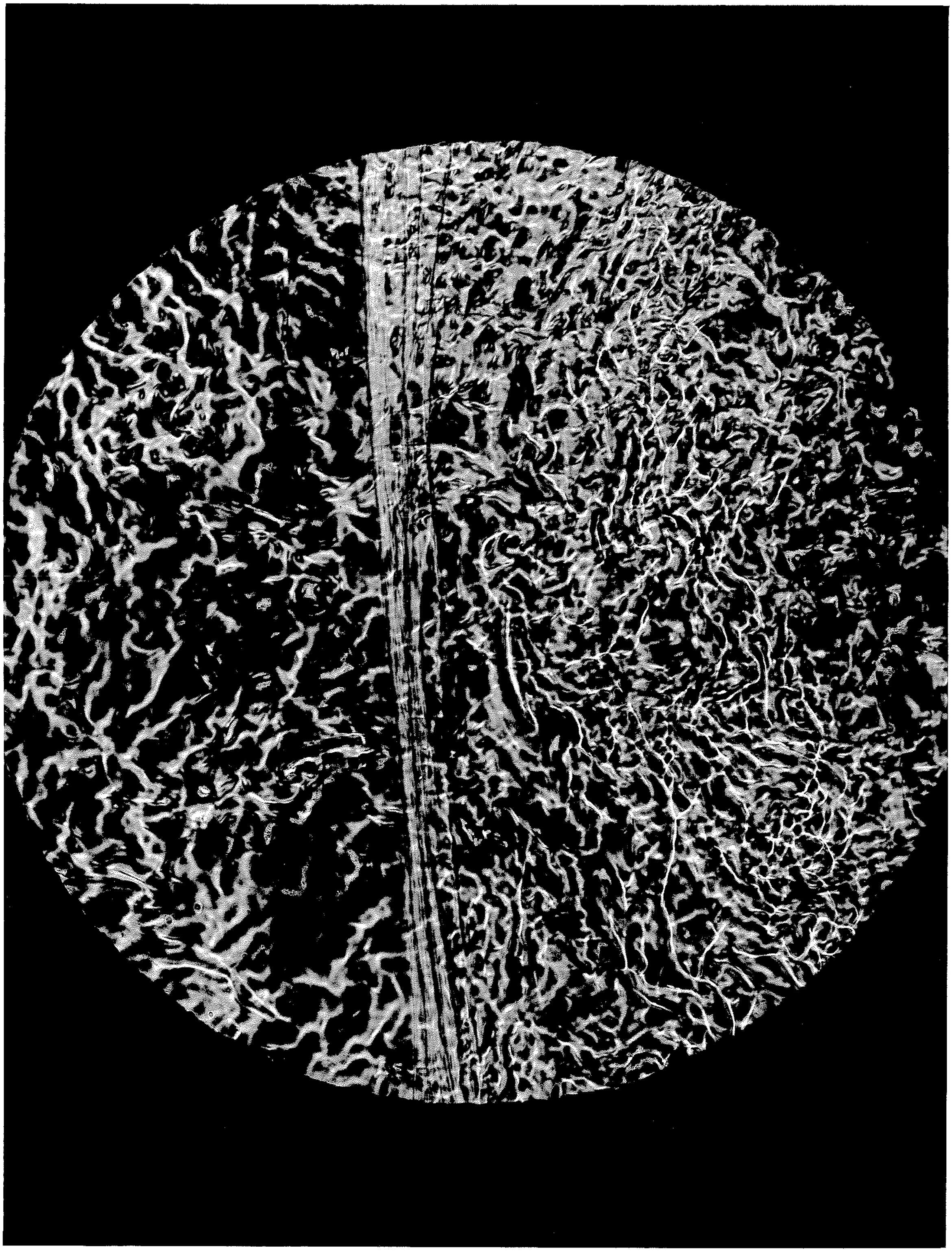

FIG. 6.20 SCHLIEREN PHOTOGRAPH OF M_S= 1.1 SHOCK MOVING FROM RIGHT TO LEFT

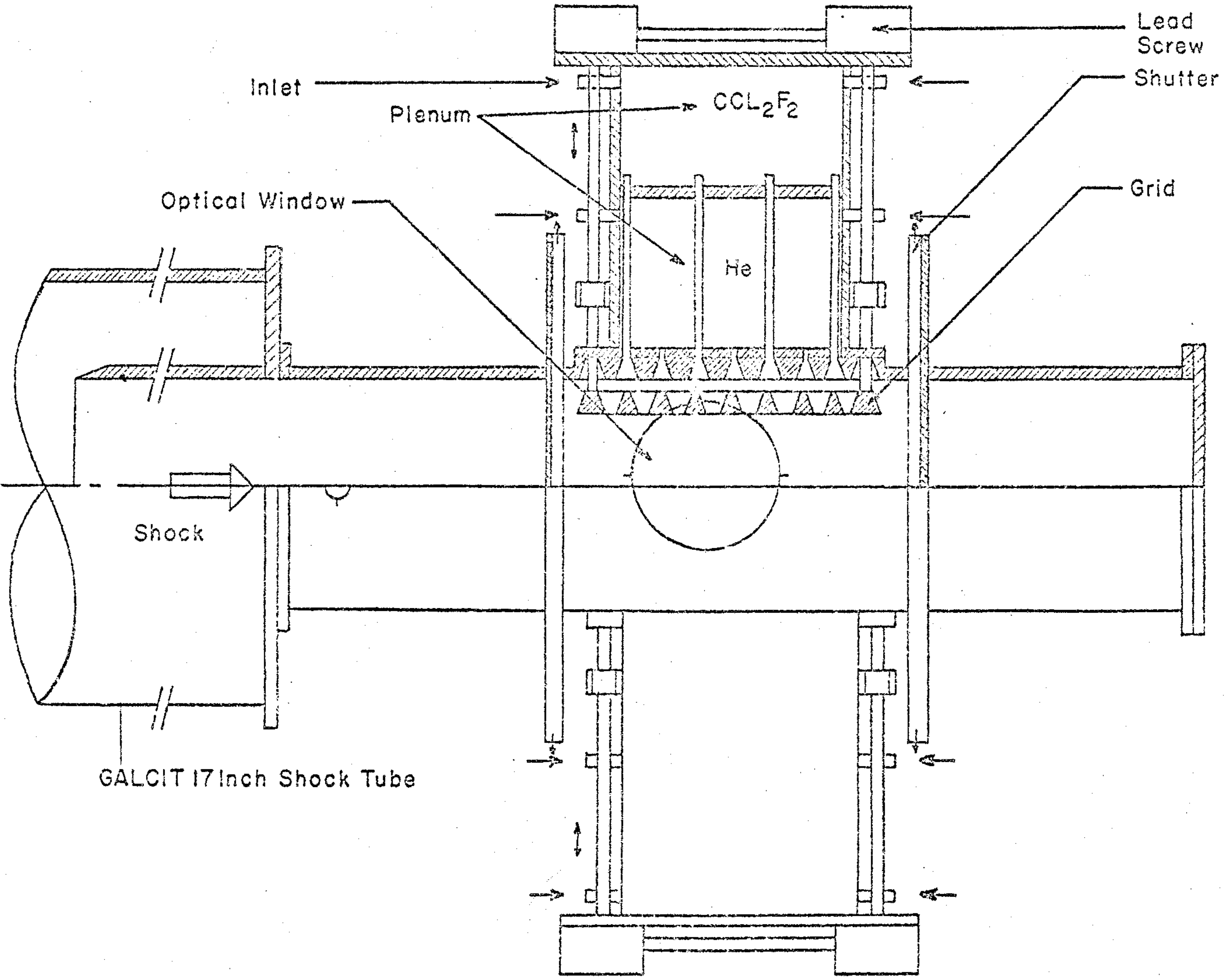

FIG. A.1 HORIZONTAL CROSS SECTION AND TOP VIEW OF TURBULENT MIXER

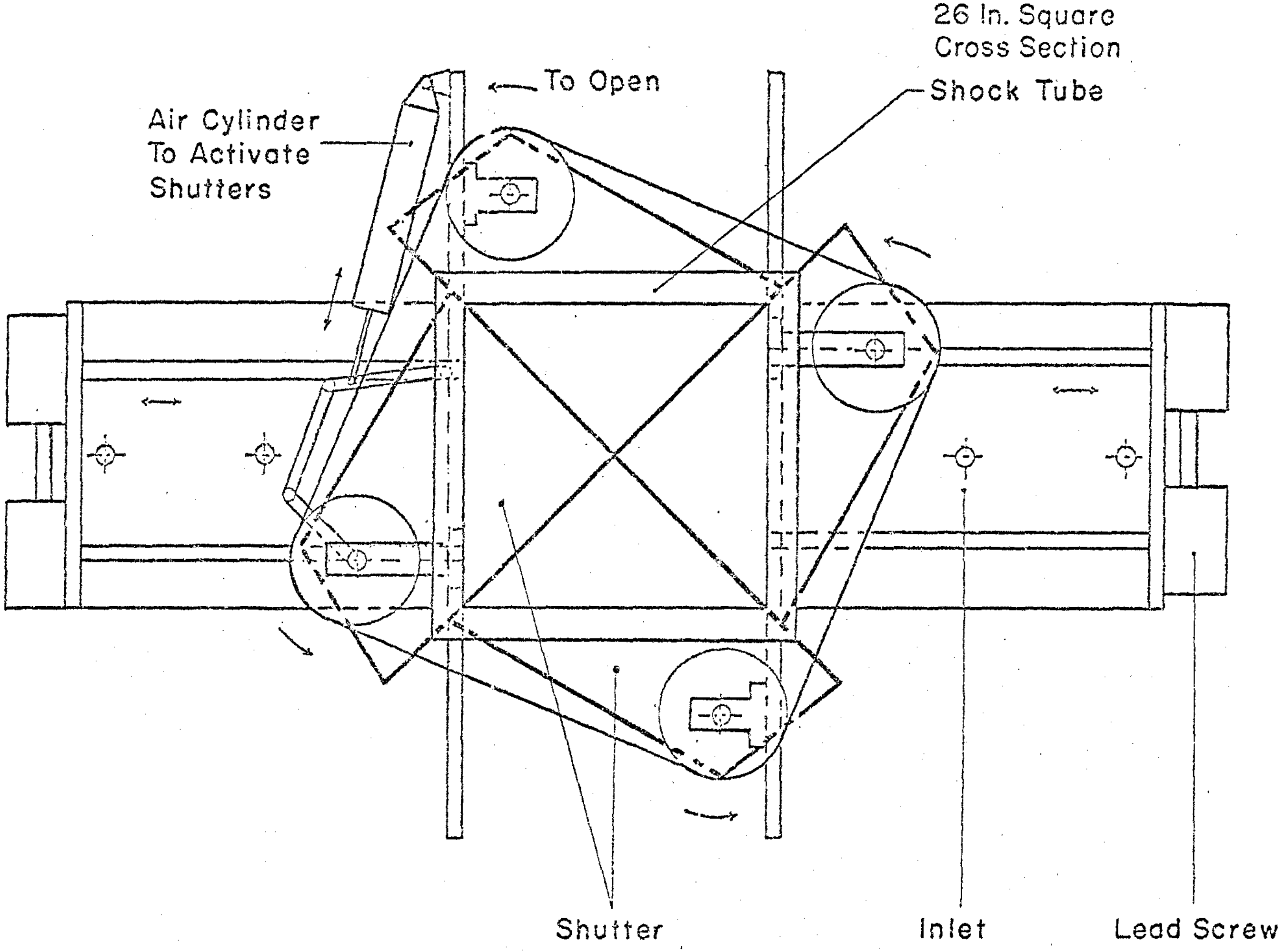

FIG.A.2 SCHEMATIC END VIEW (END PLATE REMOVED)

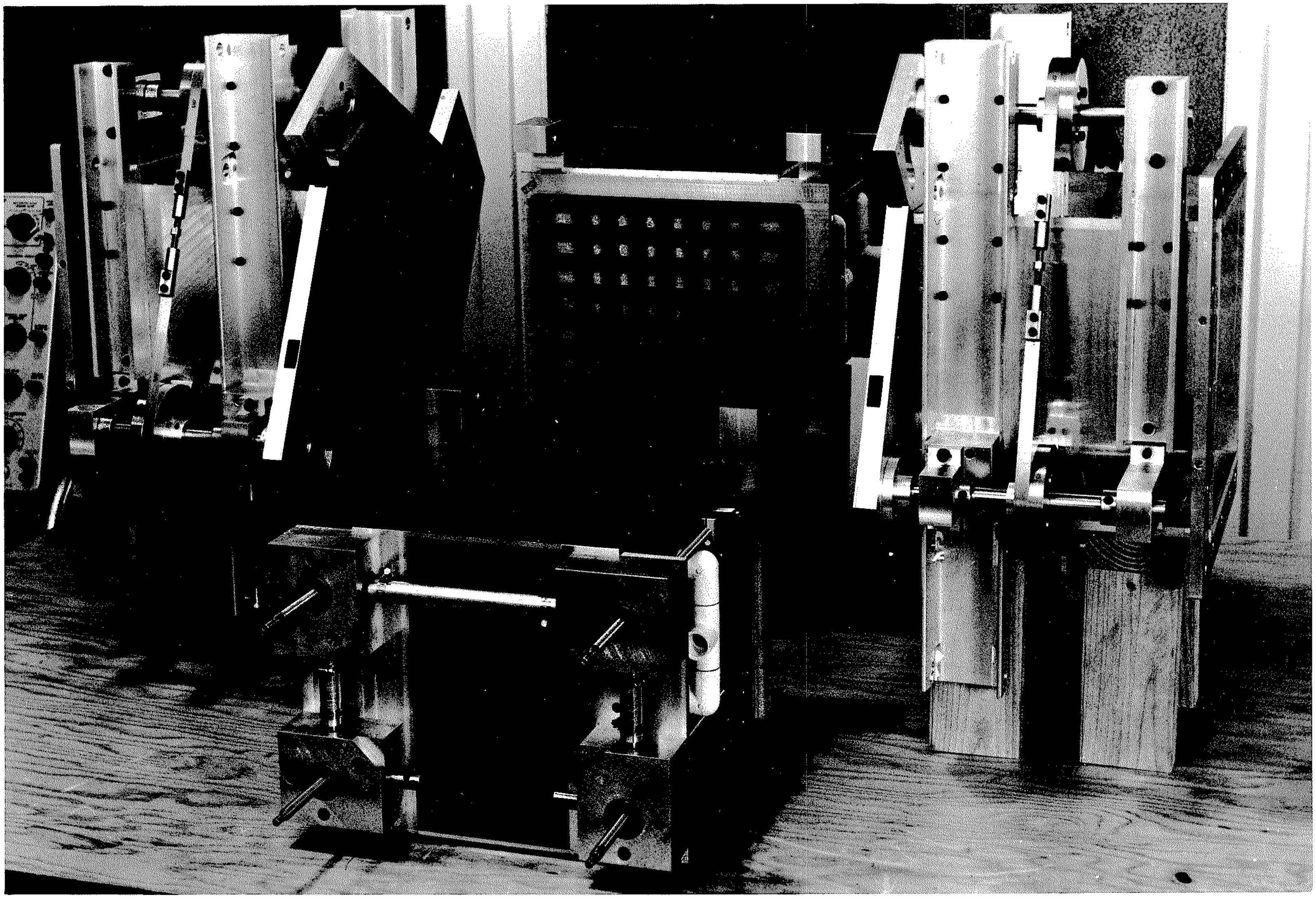

FIG. A.3 PHOTOGRAPH OF TURBULENT MIXER UNITS

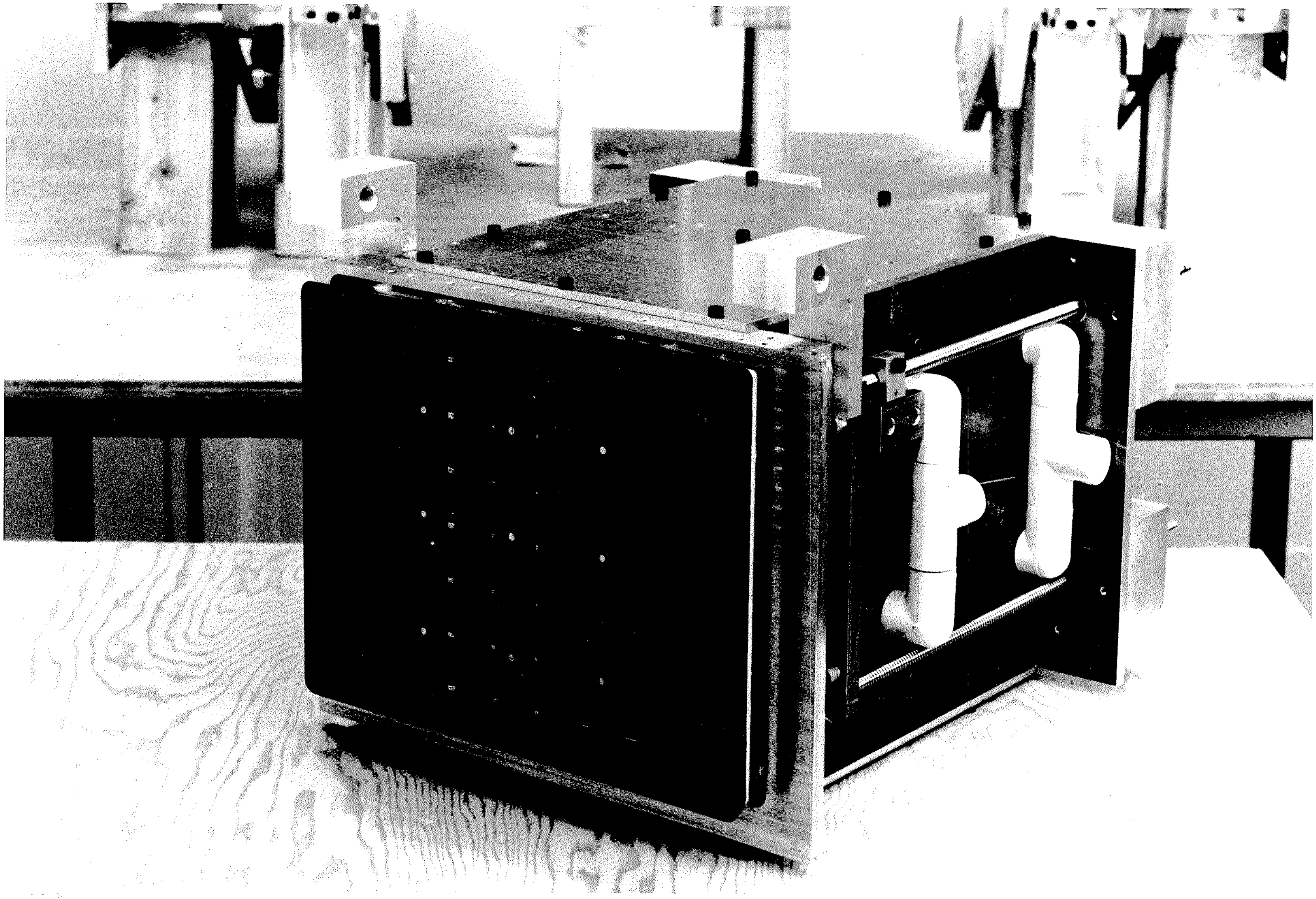

FIG.A.5 PHOTOGRAPH OF PLENUM CHAMBER AND GRID

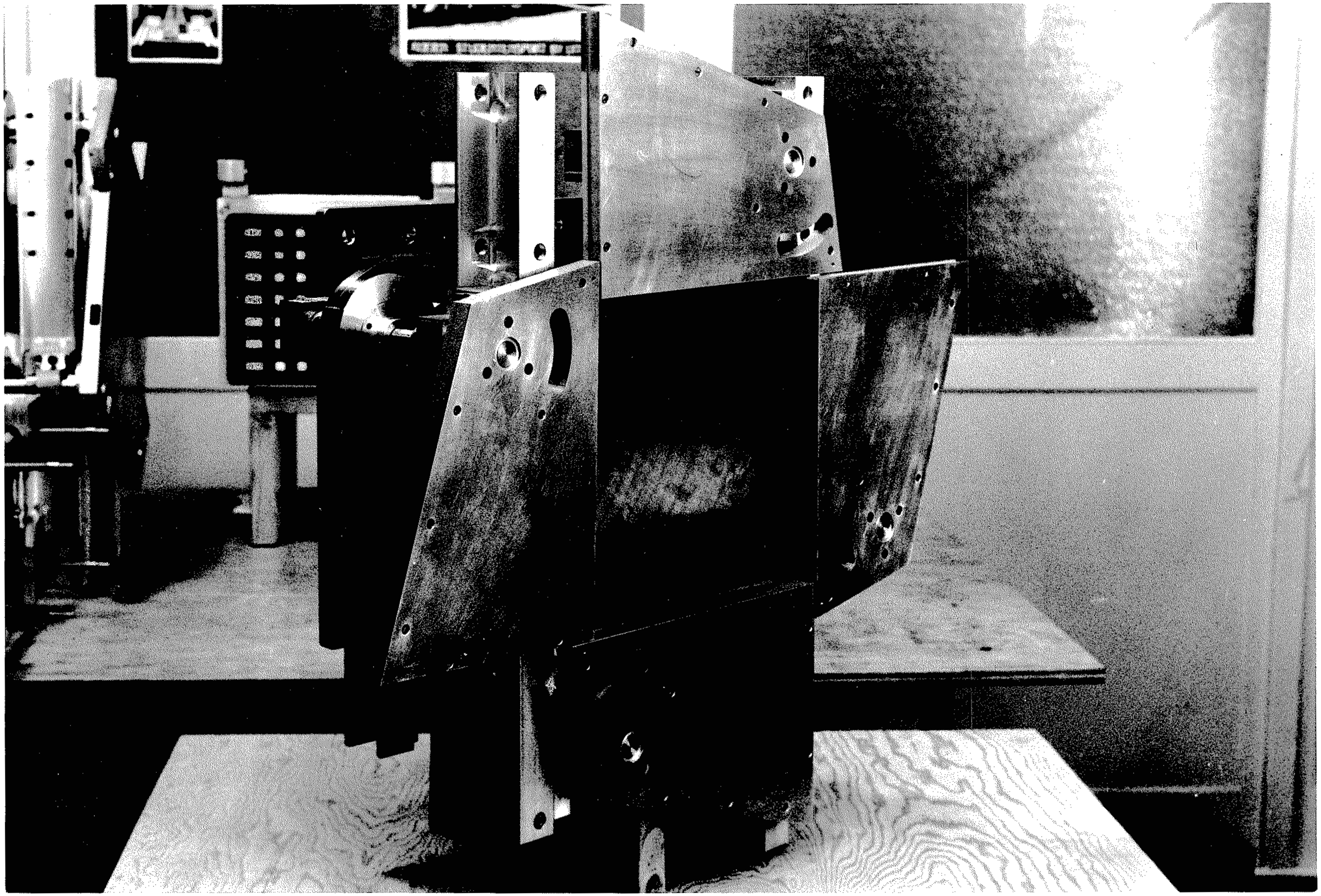

FIG.A.4 PHOTOGRAPH OF SHUTTER ASSEMBLY (OPEN)

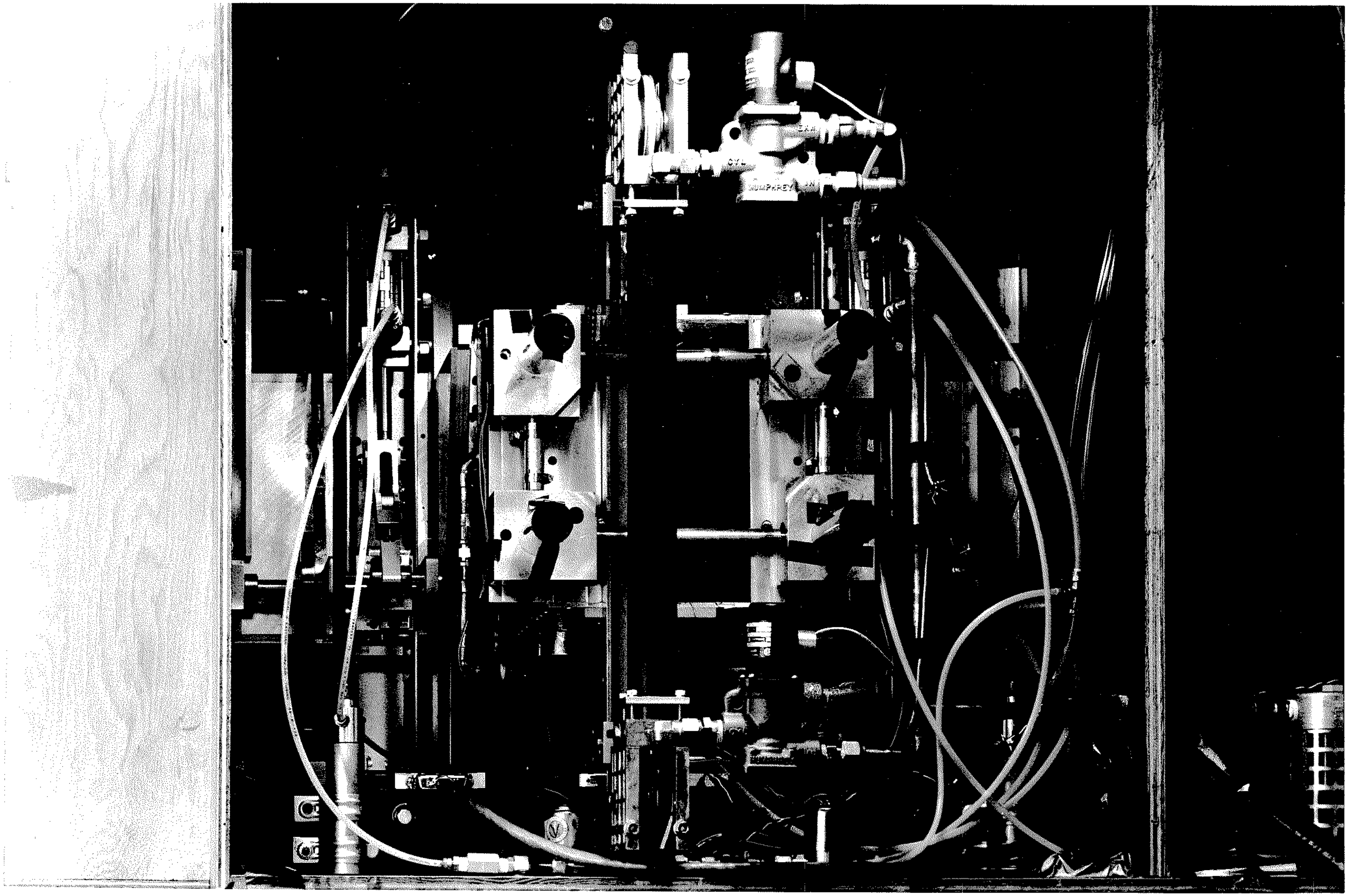

FIG. A.6 PHOTOGRAPH OF TURBULENT MIXER

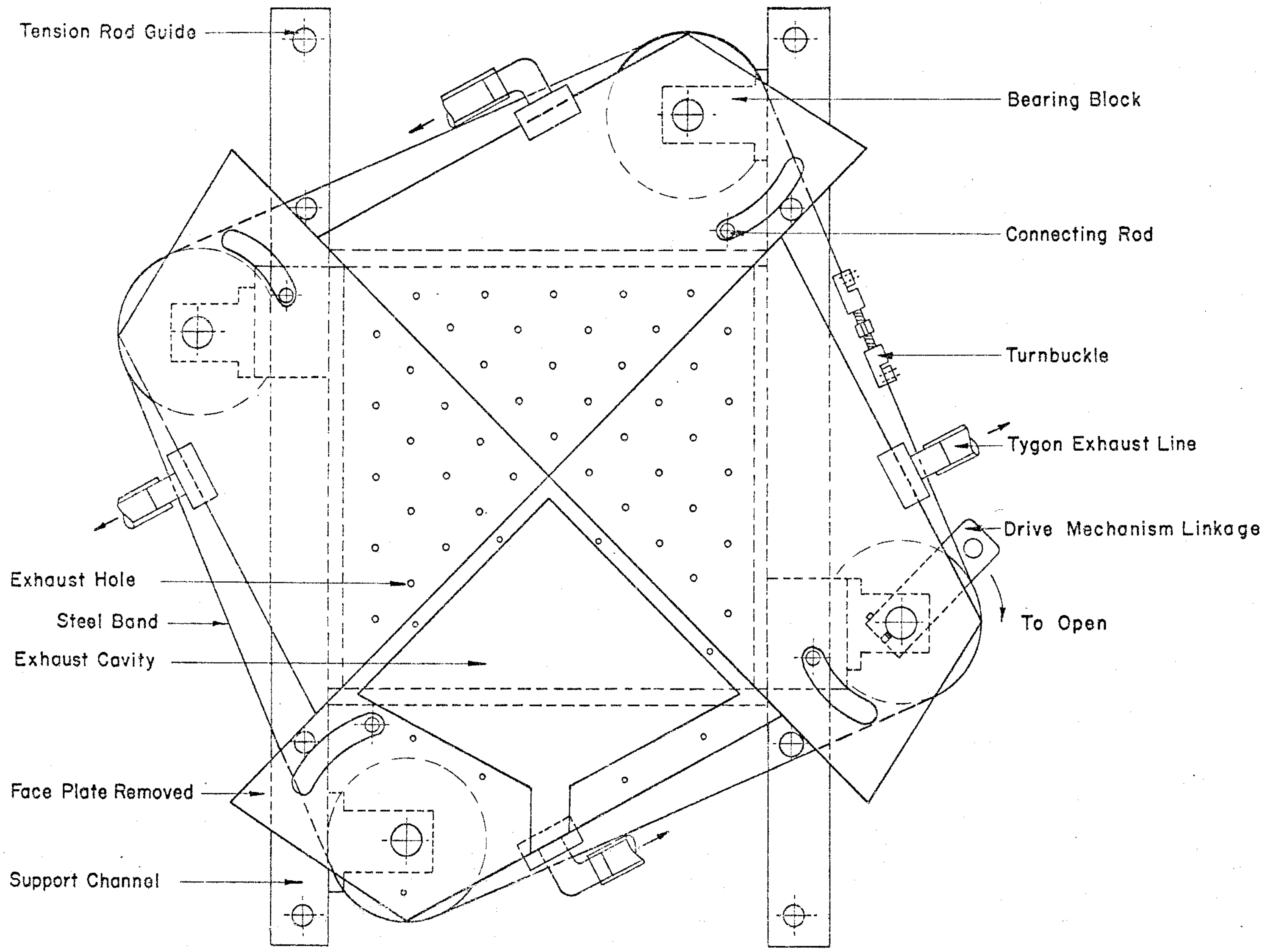

FIG. A.7 SCHEMATIC OF SHUTTER ASSEMBLY (FACE PLATE OF BOTTOM SHUTTER BLADE REMOVED)

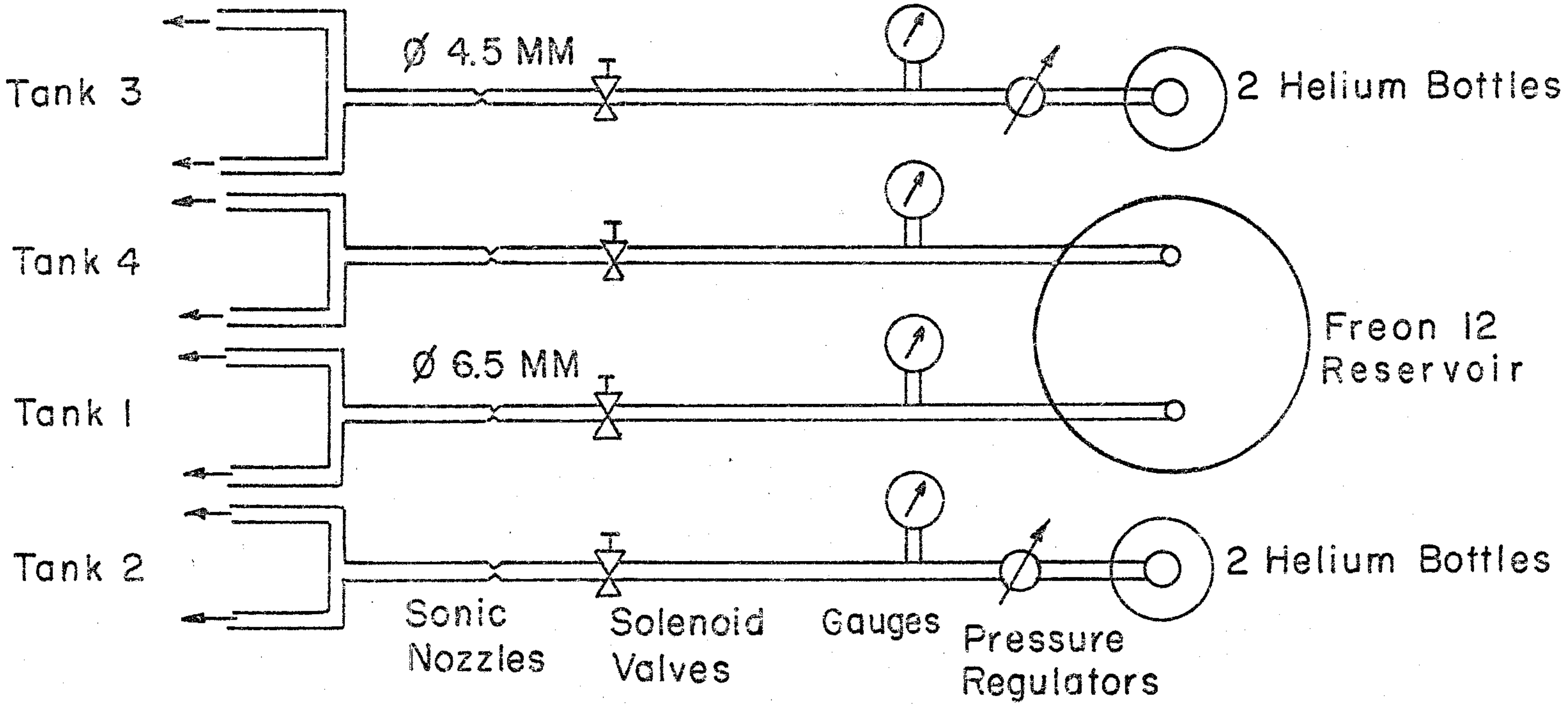

FIG.A.8 SCHEMATIC FLOW CONTROL SYSTEM FOR TURBULENT MIXER

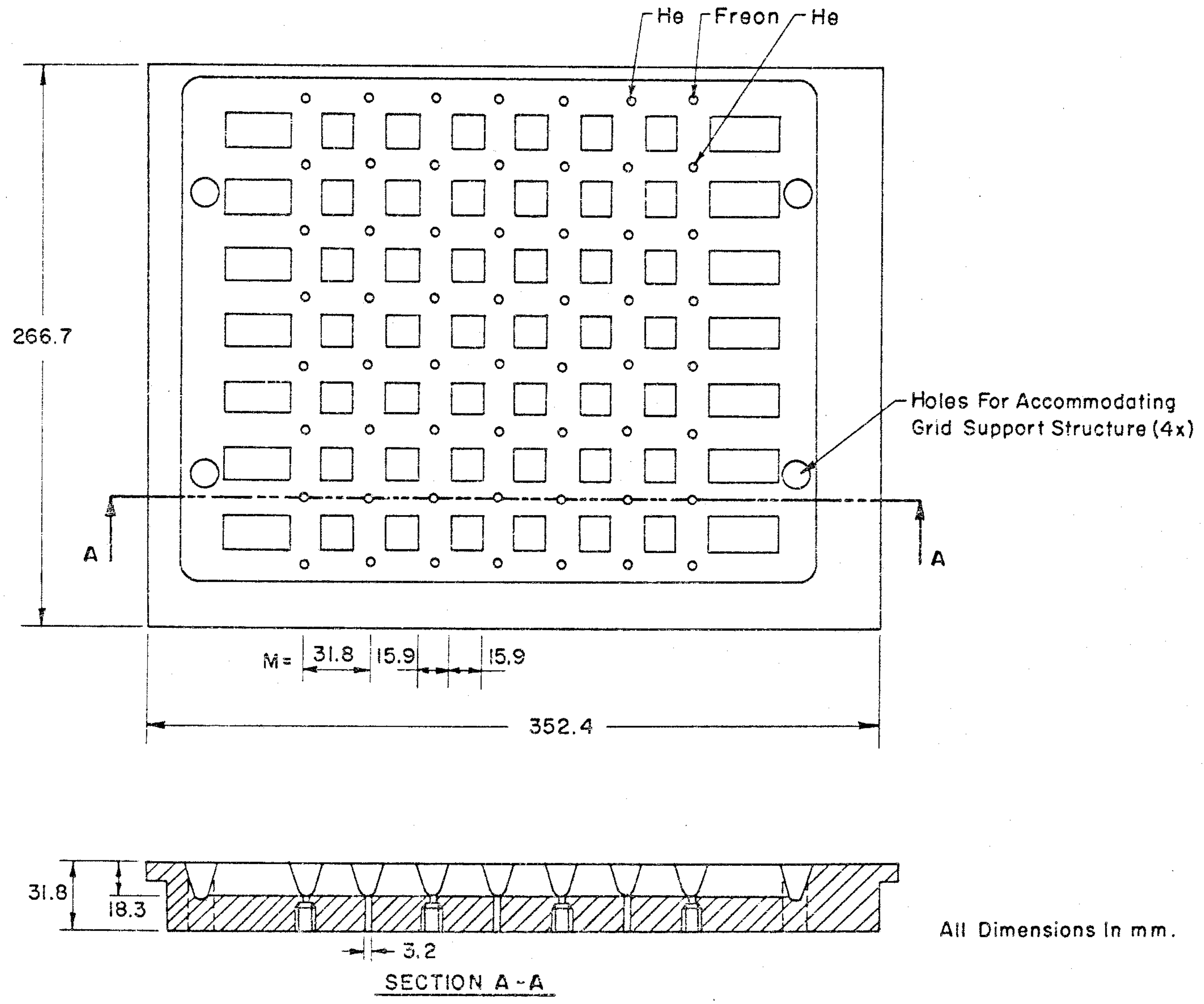

All Dimensions In mm.

FIG. A.9 GROOVE PATTERN IN THE VERTICAL SIDEWALLS OF THE MIXING ZONE

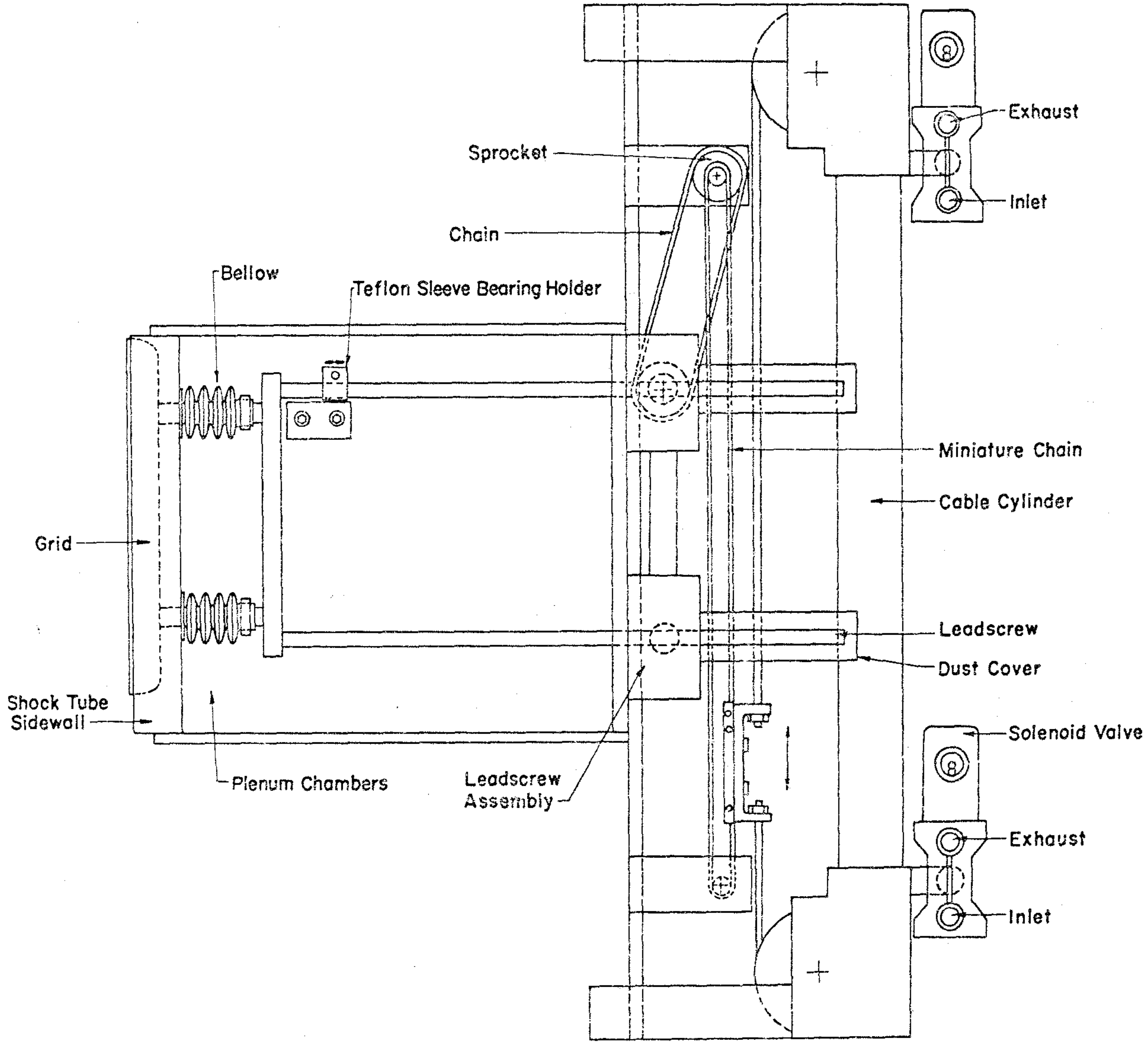

FIG.A.10 SCHEMATIC OF GRID DRIVE MECHANISM

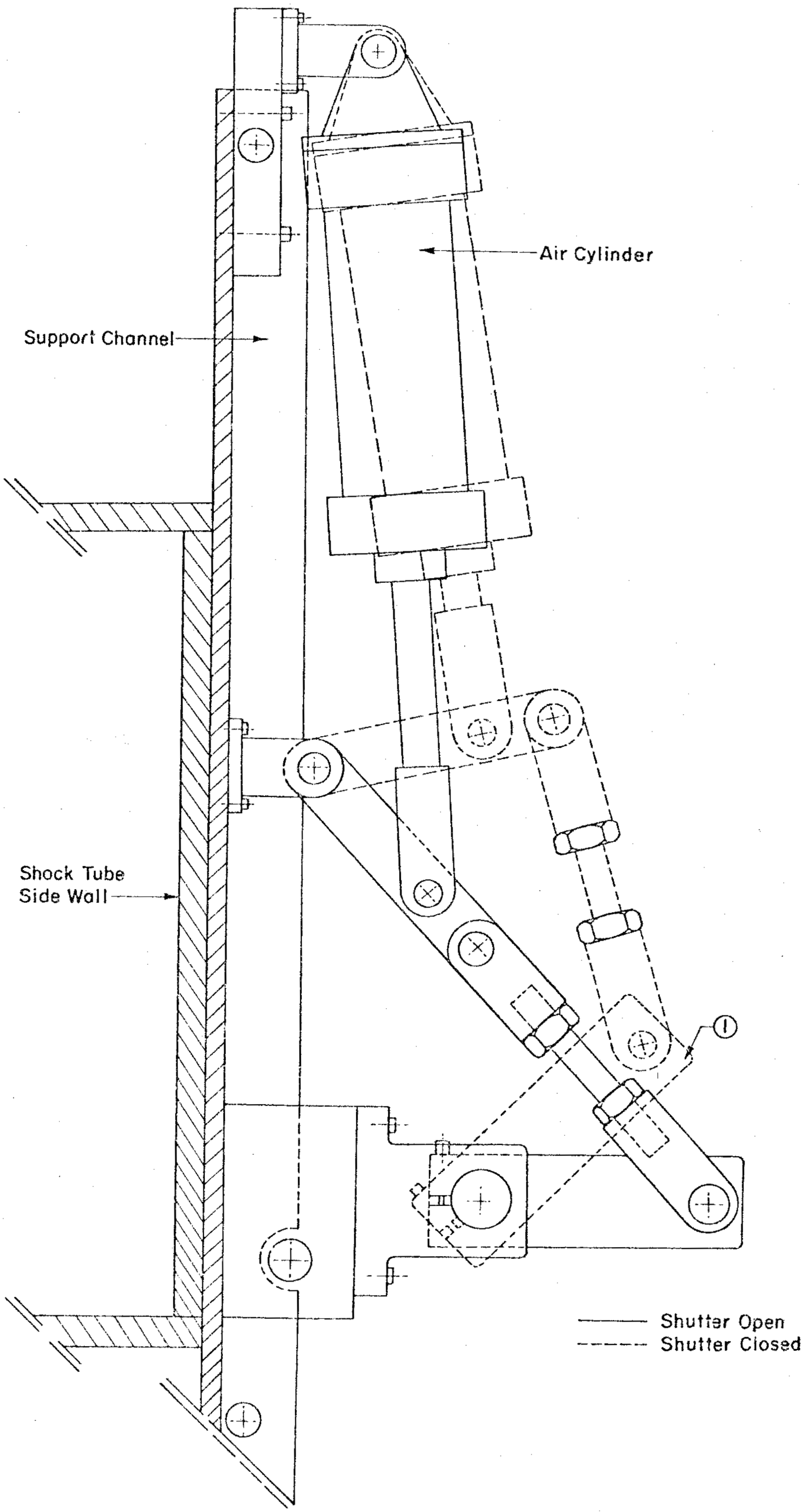

FIG. A.11 SCHEMATIC OF SHUTTER DRIVE MECHANISM

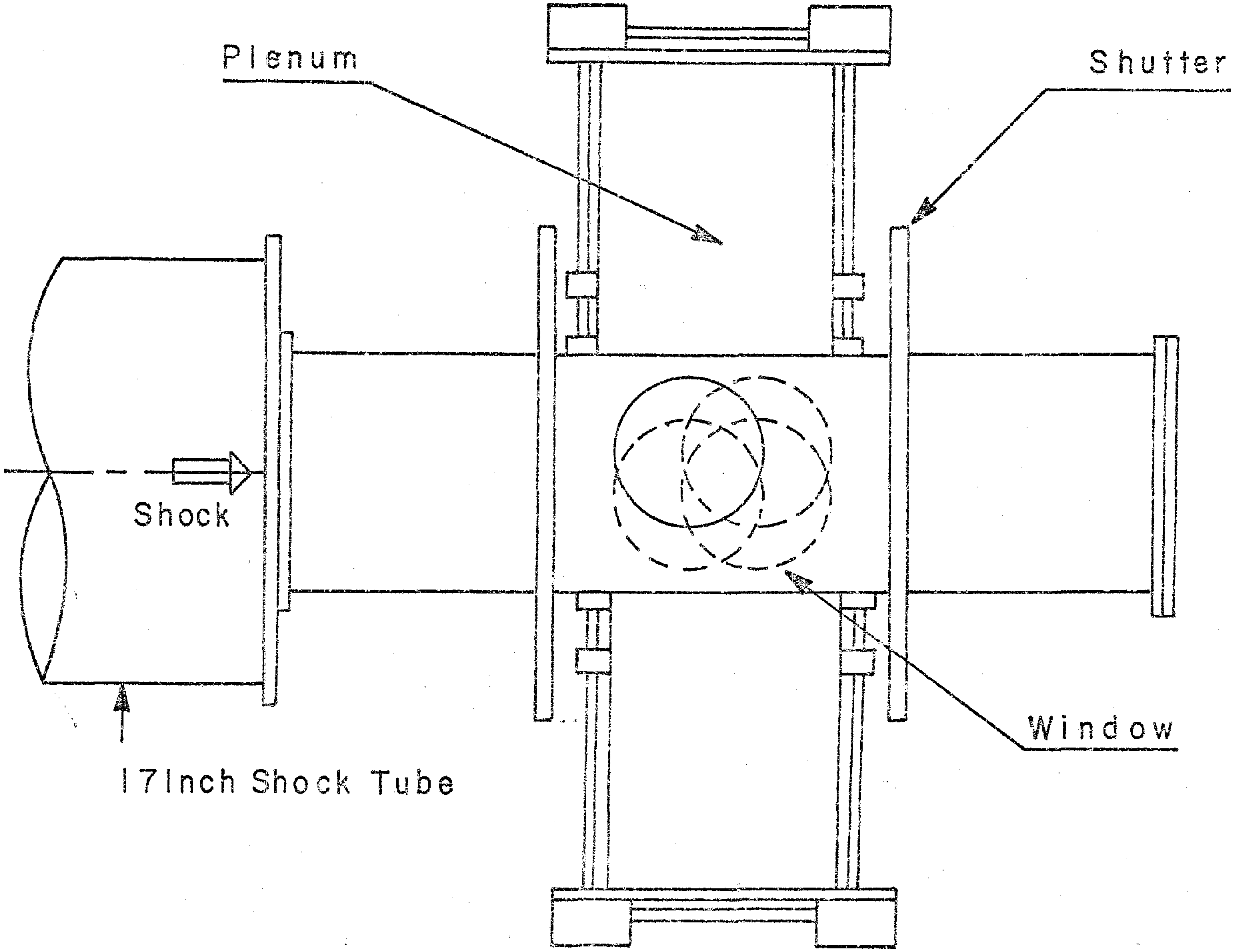

FIG. A.12 WINDOW LOCATIONS

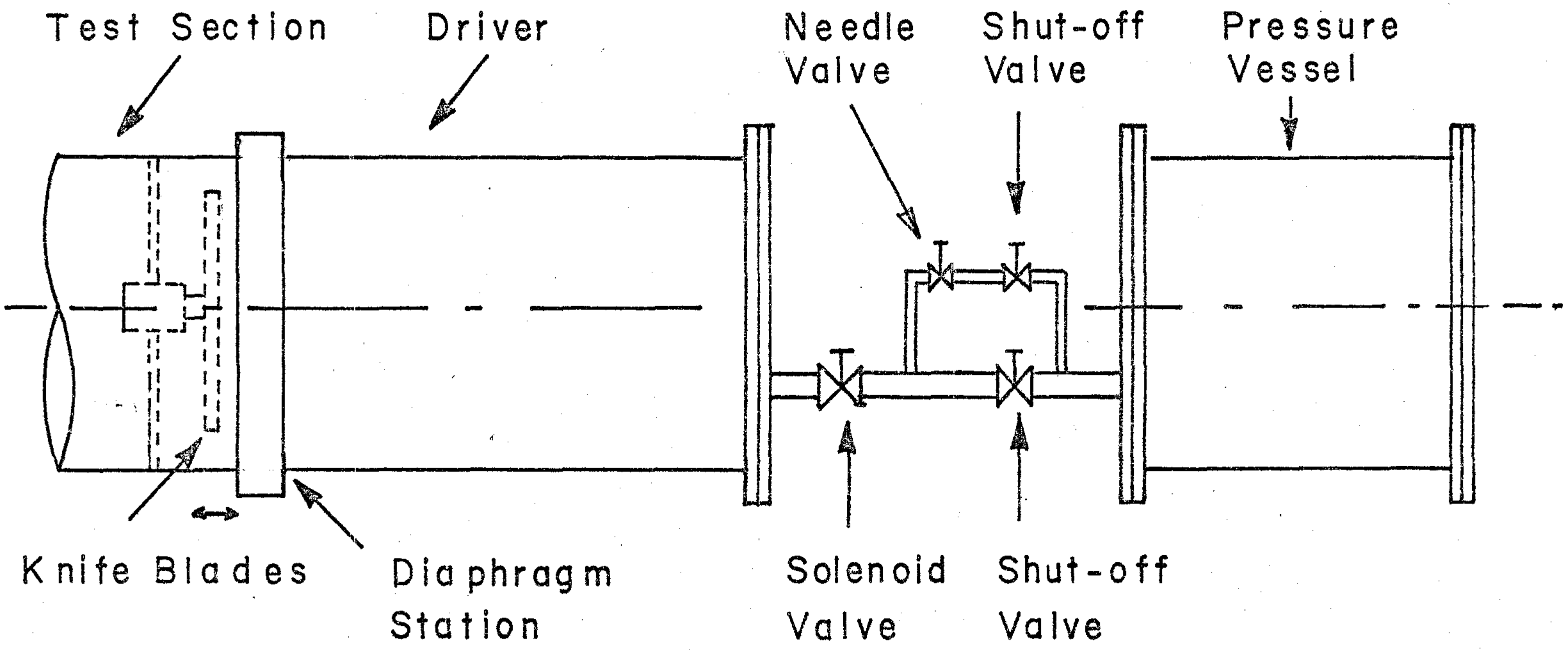

FIG.A.13 SHOCK TUBE FIRING MECHANISM

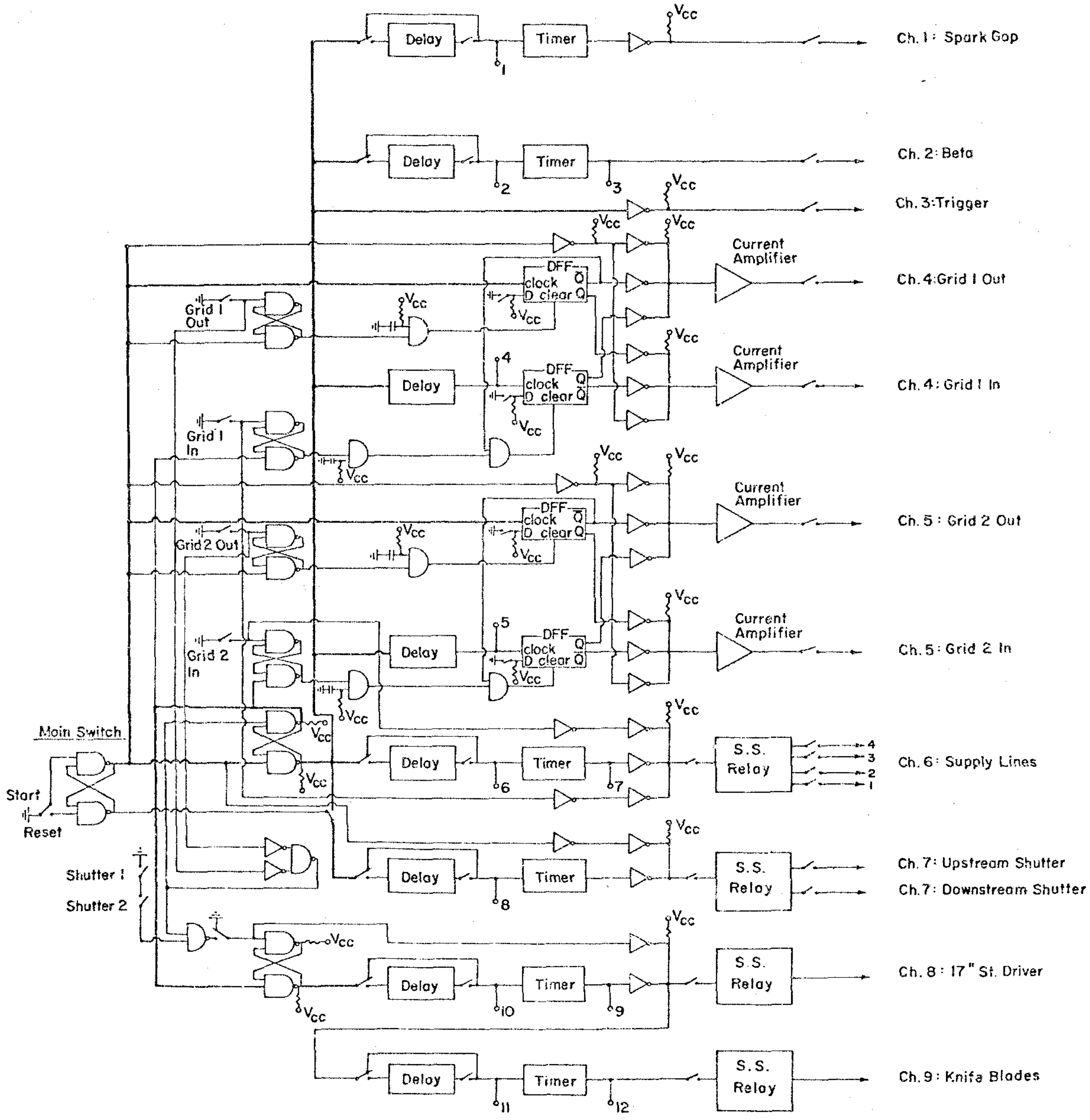

FIG. A.14 SCHEMATIC OF THE ELECTRONIC CONTROL SYSTEM FOR THE TURBULENT MIXER

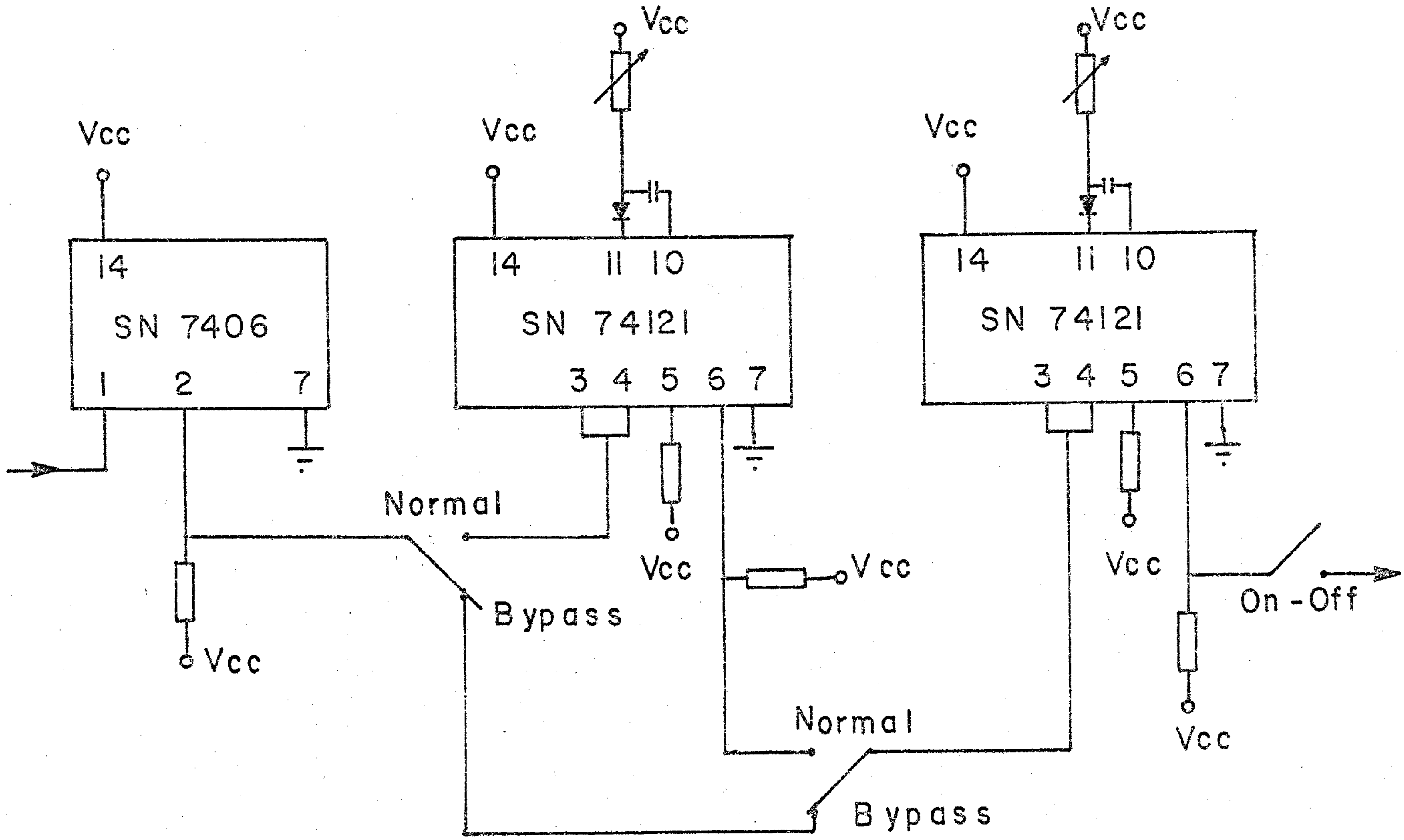

FIG.A.15 SCHEMATIC OF A SINGLE CHANNEL

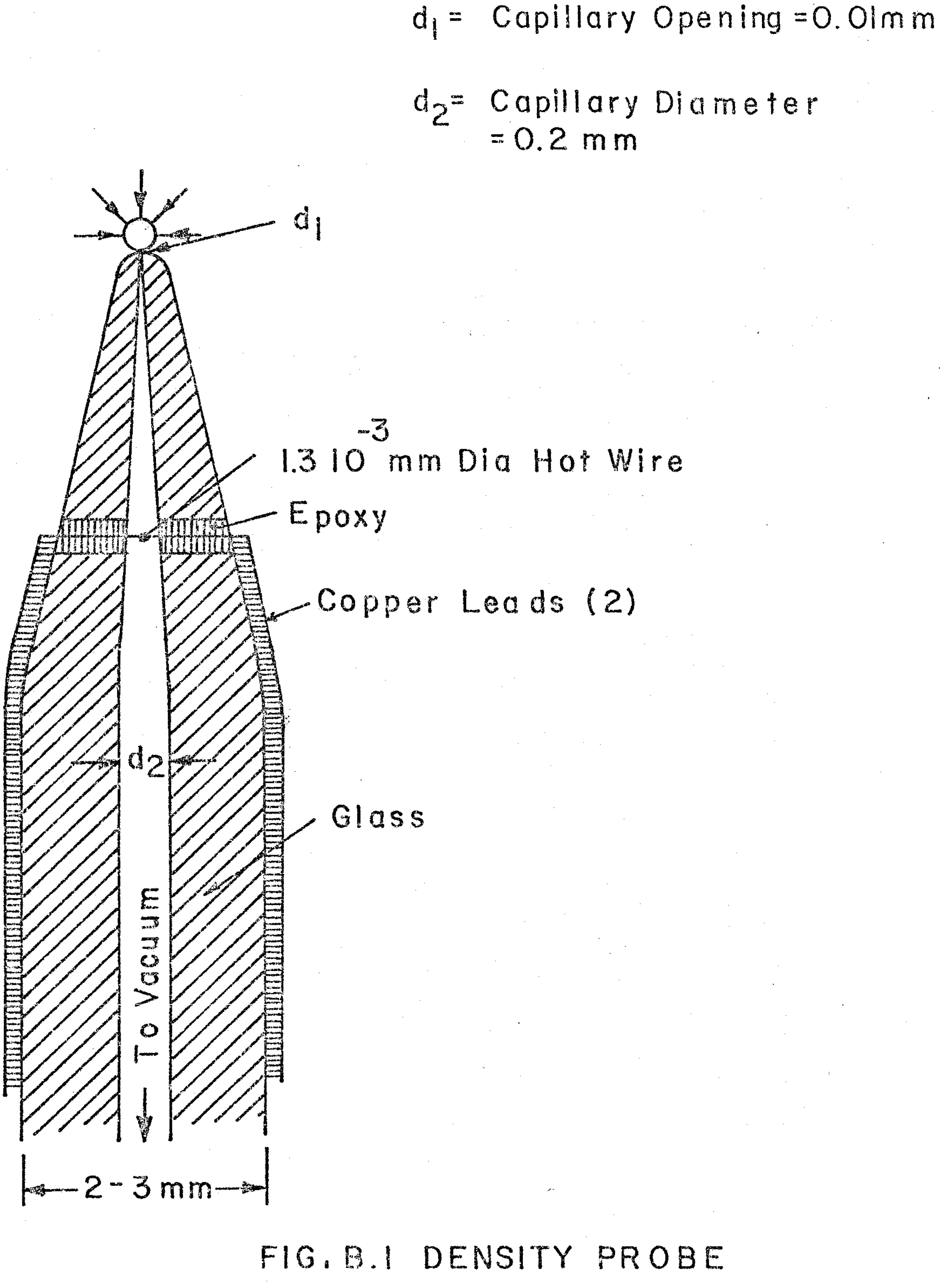

FIG. B.1 DENSITY PROBE

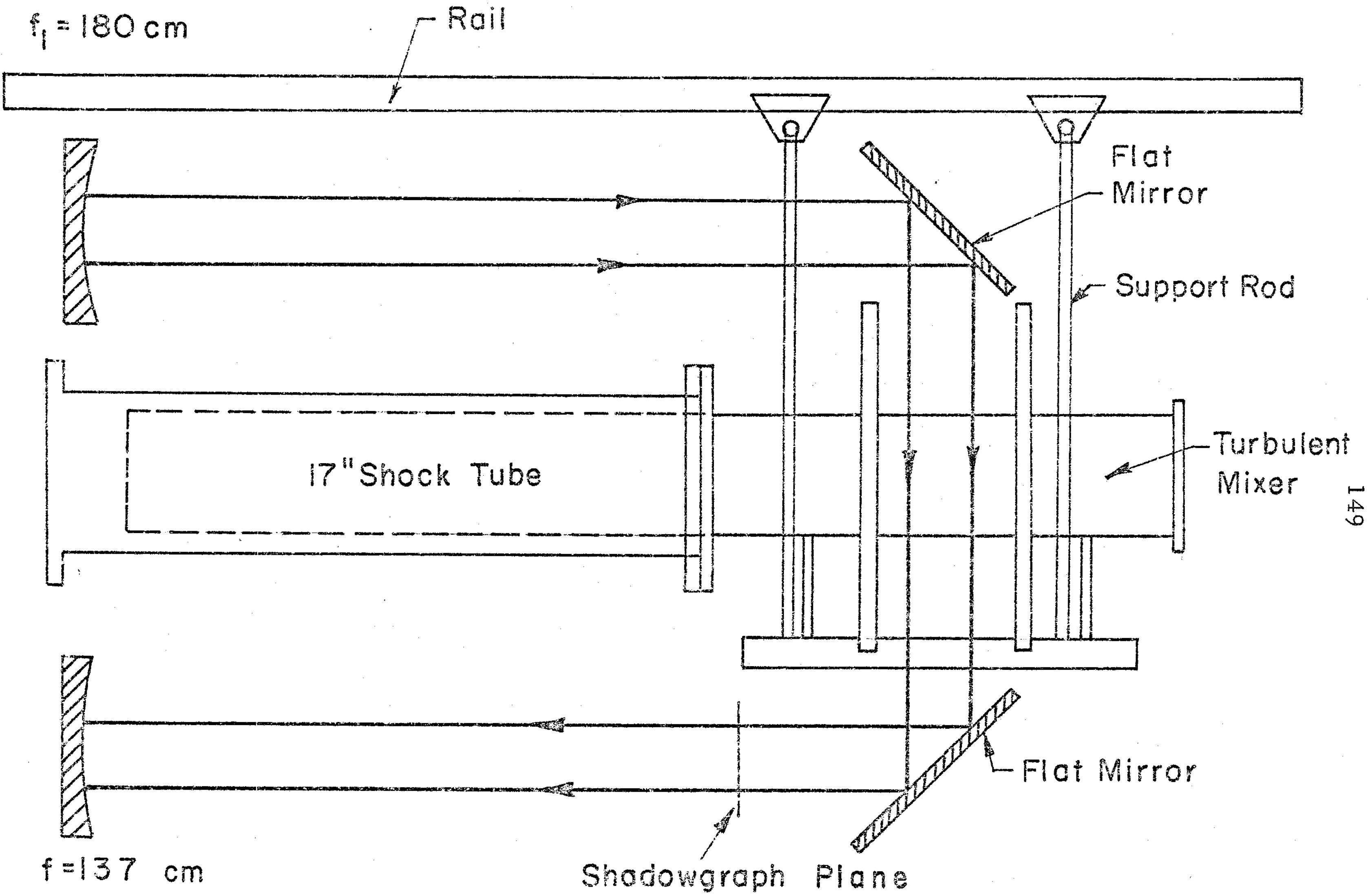

FIG. B.2 SIDE VIEW SCHLIEREN SYSTEM

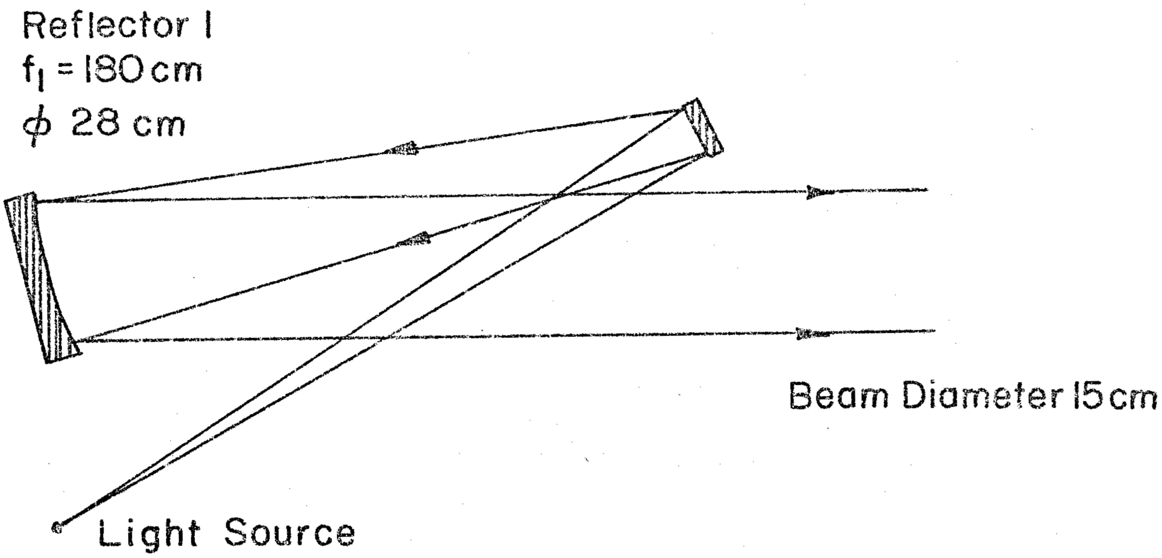

Top View Light Source Arrangement

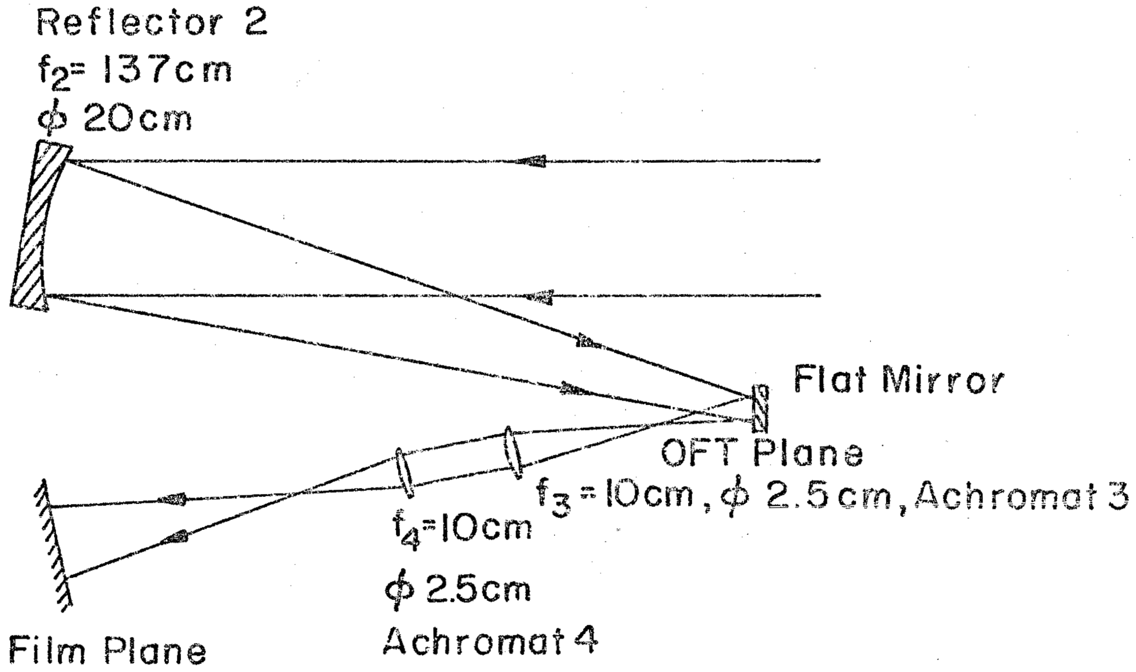

Top View Camera Arrangement

FIG.B.3 DETAILS SCHLIEREN SYSTEM

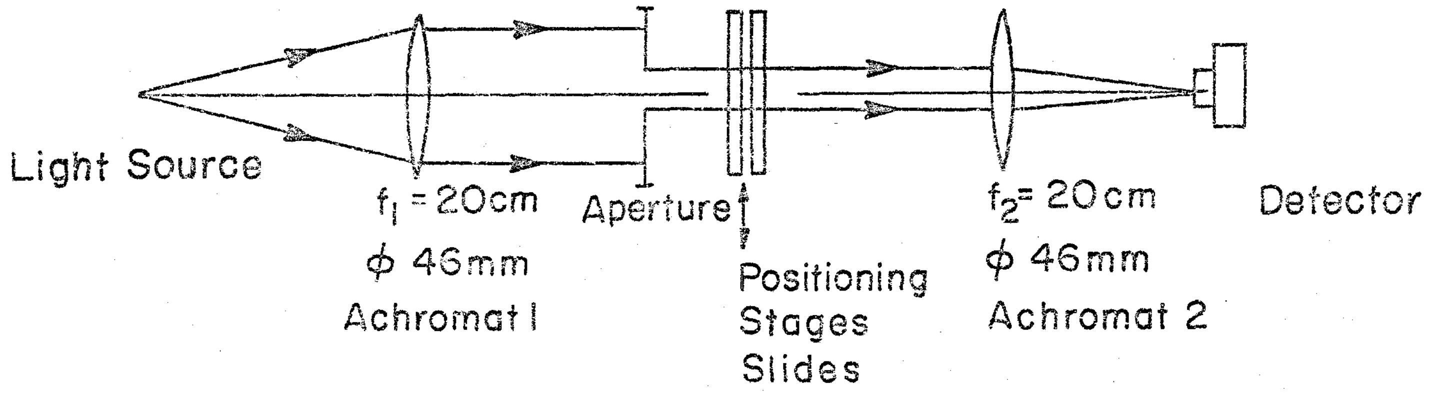

FIG.B.4 OPTICAL CORRELATOR

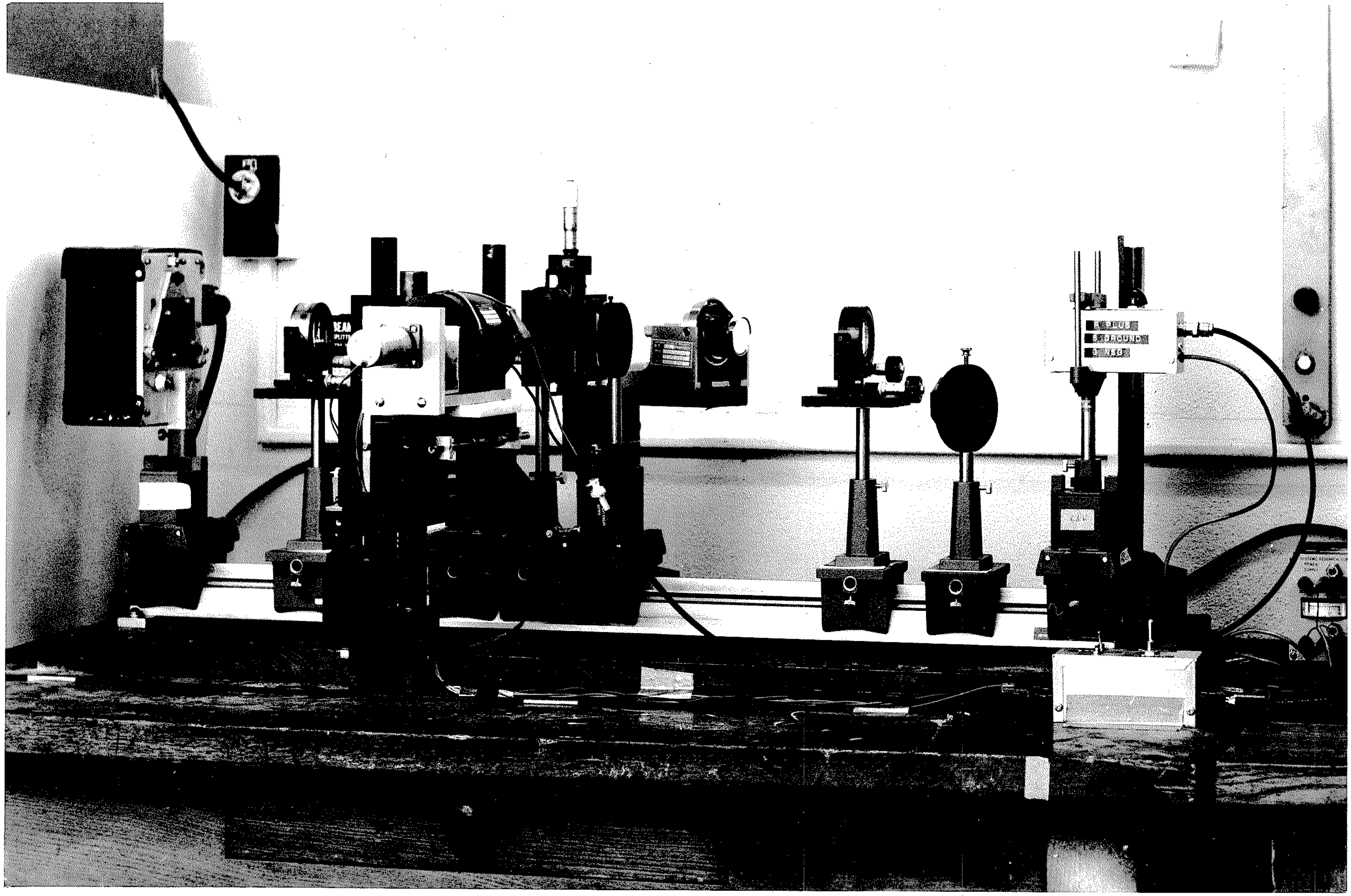

FIG. B.5 PHOTOGRAPH OF OPTICAL CORRELATOR

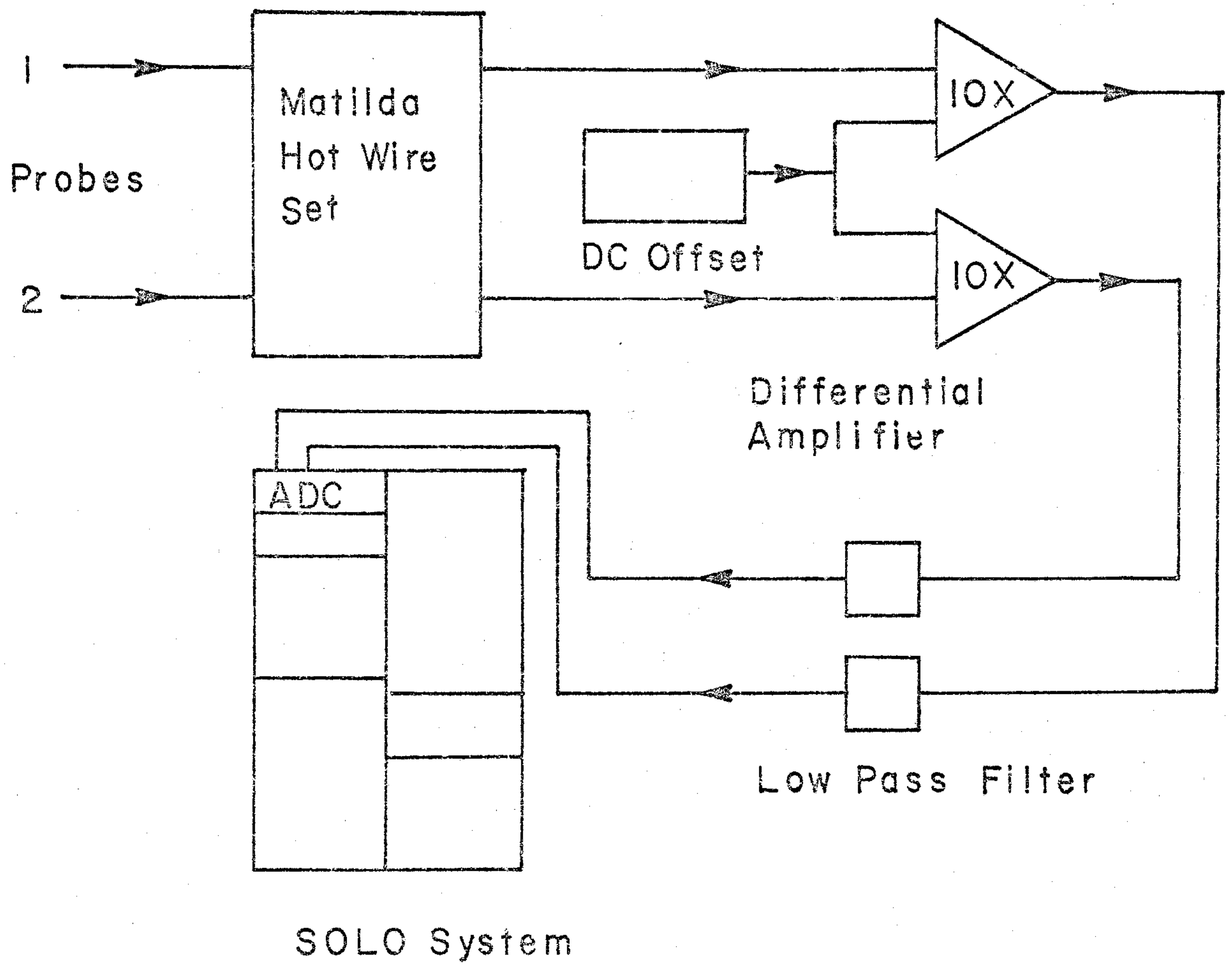

FIG. B.6 DATA ACQUISITION SCHEME

REFERENCES

1. Chernov, L. A. 1960 Wave Propagation in a Random Medium. New York: McGraw-Hill.

2. Crow, S. C. 1969 Journal of Fluid Mechanics, 37, p. 529.

3. Keller, J. B. 1964 Proceedings of symposia in Applied Math. 16, p. 145.

4. Whitham, G. B. 1952 Comm. Pure Appl. Math. 5, p. 301.

5. Maglieri, D. J. and T. L. Parrott 1963 NASA TN D-2021.

6. George, A. R. and J. P. Plotkin 1971 The Physics of Fluids, 14, p. 548.

7. Pierce, A. D. 1968 Journal of the Acoustical Society of America, 44, p. 1052.

8. Ffowcs Williams, J. E. and M. S. Howe 1973 Journal of Fluid Mechanics, 58, p. 461.

9. Hodgson, J. P. 1973 Journal of Fluid Mechanics, 58, p. 187.

10. Uberoi, M. S. and L. S. G. Kovasznay 1954 Journal of Applied Physics, 26, p. 19.

11. Brown, G. L. and M. R. Rebollo 1972 AIAA Journal, 10, p. 649.

12. Batchelor, G. K. 1970 The Theory of Homogeneous Turbulence. London: Cambridge University Press.

13. Liepmann, H. W. et al. 1962 Rev. Sci. Instr. 33, p. 625.

14. Konrad, J. H. 1977 Ph. D. Thesis, California Institute of Technology, Pasadena.

15. Goodman, J. W. 1968 Introduction to Fourier Optics. New York: McGraw-Hill.

REFERENCES (CONT'D)

16. Taylor, L. S. 1969 AIAA Journal, 8, p. 1284.

17. Thompson, L. L. and L. S. Taylor 1969 AIAA Journal, 7, p. 2030.

18. Sturtevant, B. and V. Kulkarny 1976 Journal of Fluid Mechanics, 73, p. 651.

19. Abd - El-Fattah, A. M. et al. 1975 Journal of Fluid Mechanics, 76, p. 157.

20. Whitham, G. B. 1974 Linear and Non Linear Waves. New York: John Wiley and Sons.

21. Chu, B. T. and L. S. G. Kovasznay 1957 Journal of Fluid Mechanics, 3, p. 494.